Faculty of Science and Technology
Department of Chemistry

Enzyme mechanism, thermostability and structural studies of OXA-48 like carbapenemases involved in antibiotic resistance

Ane Molden Thomassen
KJE-3900, Master Thesis in Chemistry - May 2018

Acknowledgements

Abbreviations

Δε	Extinction coefficient
A. beumannii	*Acinetobacter beumannii*
AFI	After induction
Amp	Ampicillin
AMR	Antimicrobial resistance
ATEV	After addition of TEV protease
BFI	Before induction
BSA	Bovine Serum Albumin
BTEV	Before addition of TEV protease
CAM	Chloramphenicol
CHDL	Carbapenem-hydrolysing class D β-lactamase
CS	Cell supernatant
Da	Dalton
DBL	Class D β-lactamase
DMSO	Dimethyl sulfoxide
DNA	Deoxyribonucleic acid
DSC	Differential scanning calorimetry
ddH_2O	Double-distilled water
dNTP	Deoxyribonucleotide
E. coli	*Escherichia coli*
EDTA	Ethylene-diamine-tetra-acetic acid
ESBL	Extended spectrum β-lactamase
FT	Flow-through
HEPES	4-(2-hydroxyethyl)-1-piperazineethanesulfonic acid
IMAC	Immobilized metal affinity chromatography
IPTG	Isopropyl-β-D-1-thiogalactopyranoside
k_{cat}	Turnover number in Michaelis-Menten kinetics
K_d	Dissociation constant
K_M	Michaelis kinetics constant
K. pneumoniae	*Klebsiella pneumoniae*
KPC	*Klebsiella pneumoniae* carbapenemases
LB	Lysogenic Broth

MS	Mass spectrometry
MST	Microscale thermophoresis
NMR	Nuclear magnetic resonance
OD	Optical density
o/n	Overnight
OXA	Oxacillinase
P. aeruginosa	*Pseudomonas aeruginosa*
Pa	Pascal
PBP	Penicillin binding protein
PCR	Polymerase chain reaction
PEG MME	Polyethylene glycol methyl ether
rpm	Rounds per minute
SB	Sample buffer
SBL	Serine-β-lactamase
SDS-PAGE	Sodium dodecyl sulphate-polyacrylamide gel electrophoresis
SEC	Size-exclusion chromatography
SOC	Super optimal broth with catabolite repression
T_m	Transition midpoint temperature
TAE	Tris-acetate-EDTA
TB	Terrific broth
TET	Tetracycline
TEV	Tobacco Etch Virus
VIM	Verona integron-encoded metallo-β-lactamase
WC	Whole cell

Abstract

Antibiotic resistance is a growing problem, and is now being recognized as a world-wide crisis in modern medicine. Coordinated awareness and action are needed to combat the fact that antimicrobial resistance is creating a health crisis rapidly outpacing available treatment options. β-lactam antibiotics are the most commonly used antibiotic, and the most widespread β-lactam resistance is the expression of enzymes with the ability to hydrolyse β-lactam antibiotics. Herein class D β-lactamases are commonly referred to as OXA-enzymes. OXA-enzymes are considered an increasing problem as they are spreading rapidly, and can be found among clinically relevant Gram-negative species.

OXA-48 was first identified from a carbapenem- and multidrug- resistant *Klebsiella pneumoniae* isolate in Turkey in 2001, and is now one of the most geographically widespread members of the class D β-lactamases. Multiple aspects concerning OXA-48 and OXA-48 like enzymes were examined during this thesis, using methods such as site-directed mutagenesis, X-ray crystallography, enzyme kinetics, microscale thermophoresis (MST) and differential scanning calorimetry (DSC), to contribute to a better understanding of the enzyme mechanism and structure-function relationship.

OXA-48 like β-lactamases differ only by a few amino acid substitutions and/or deletions, and the resulting effects were not always evident. To gain a greater insight into the different OXA-48 like β-lactamases, protein crystals were obtained for OXA-181, OXA-163 and the novel β-lactamase OXA-436, to determine the crystal structure. DSC analysis was used to determine the thermal stability for OXA-48, OXA-181, OXA-245, OXA-163 and OXA-436 in two different buffer systems. The differences in thermal stability were discussed based on the obtained crystal structures.

Many class D β-lactamases, including OXA-48 forms dimers in solution, however the structural nor the functional basis for this dimerization were obvious. Specific residues at the dimer interface could be potential targets for allosteric inhibitors. Three OXA-48 mutants affecting the dimer interface (R189A, R206A and R189A/R206A) were investigated by thermal stability analysis, dimer affinity determination, and enzyme activity assays. Based on these results it was concluded that the OXA-48 dimer is strong and held together by many salt-bridges at the dimer interface. Destabilization of the dimer does not seem to affect the enzyme activity significantly, but appears to be important for the thermal stability of the enzyme.

Previously conducted mutational studies concerning the active site triad S70-T71-L73 had shown S70 to be crucial for enzyme activity, but also that the active site serine contributes

to steric strain in the active site. S70 and L73 are assumed to be essential for the enzyme mechanism, however the role of the conserved active site residue T71 is not known. To further investigate the nature of the active site and the function of T71, the crystal structure of the OXA-48 mutants S70T and S70T/T71S were determined, and the enzyme activity measured. The obtained results suggested that both residues are crucial for the enzyme since the mutations greatly reduced the enzyme activity. This was explained by an increased steric strain, and unfavorable orientation of the active site residues.

Ceftazidime and ceftazidime/avibactam is used against a broad range of β-lactamases, and it is possible that pathogens carrying the *bla*$_{\text{OXA-48}}$ gene could be exposed to this treatment. Many pathogens carrying the *bla*$_{\text{OXA-48}}$ gene, are multi-drug resistant, and a selective pressure of ceftazidime/avibactam on OXA-48 carrying bacteria might cause mutations to occur within OXA-48 conferring resistance towards this drug combination. The OXA-48 mutants P68A and P68A/Y211S were discovered in previous evolution studies selecting for OXA-48 ceftazidime and ceftazidime-avibactam resistance. Enzyme kinetics were therefore used to investigate the effect of these mutations on the enzyme activity with different substrates. The results suggested increased flexibility in the active site due to lack of P68, allowing for hydrolysis of larger substrates such as ceftazidime, to which OXA-48 is inactive. However, this seems to come at the cost of reduced ability to hydrolyse other substrates, compared to OXA-48.

Table of Contents

x

1   Introduction

For more than 70 years, antibiotics have been used to cure infections, and has over the years been used, and produced, at an increasing rate. The use of antibiotics is a cornerstone in modern medicine, agriculture and farming. Its use in medicine has reduced childhood mortality and increased life expectancy, being crucial for treatments such as chemotherapy, surgery, and even to recover from common community-acquired infections such as pneumonia [1, 2]. Antibiotic-resistance is a growing problem, and new multidrug-resistant pathogens are spreading rapidly causing increased mortality rates and treatment costs. Antibiotic resistance is now being recognized as a world-wide crisis in modern medicine, and is expected to get much worse. It has been estimated that antimicrobial resistance (AMR), or drug resistance claims 700 000 lives a year, being a low estimate, with an expected increase to 10 million deaths per year by 2050 [3], as illustrated in Figure 1-1.

The Global Risks Report from 2013 warned about the growing risk of antimicrobial resistance, and lists antimicrobial resistance as one of the greatest treats to human health [4]. WHO published in 2014 their first global surveillance report on antimicrobial resistance, to make it clear that widespread antimicrobial resistance is no longer simply a possibility, but is happening all over the world. Coordinated awareness and action is needed to deal with the fact that antimicrobial resistance is creating a health crisis rapidly outpacing available treatment options [5].
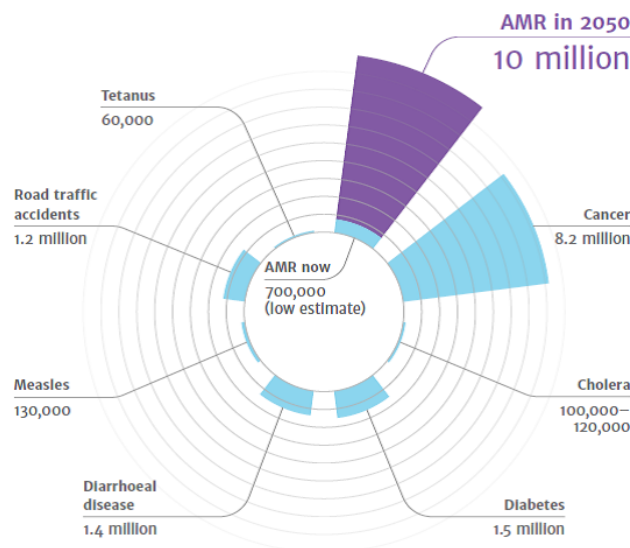
Figure 1-1: Estimated global number of deaths caused by common causes in 2016, showed in blue. The expected rise of antimicrobial resistance (AMR) caused deaths per year by 2050 is 10 million, compared to 700 000 in 2016. Figure from reference [3].

1.1 Antibiotic resistance; mechanisms of resistance and β-lactam antibiotics

Alexander Fleming received the Nobel Prize in Medicine in 1945 for his part in discovering the first mass produced antibiotic; penicillin. Already in his speech he warned that bacteria could develop resistance towards this "miracle drug" [5]. The development of resistance towards antibiotics is a part of the microbe evolution. Their high population numbers and capacity to exchange genetic information makes them remarkably ready to adapt. It is clear however, that the extensive use of antibiotics has forced this evolutionary process to move much faster than expected, causing the rapid spread of multi-resistant pathogenic bacteria worldwide, by selecting for bacteria with an elevated mutation rate [6].

Bacteria can develop antibiotic resistance through several mechanisms; by altering the antibiotic binding site (or target) through mutations, changing the cell permeability and efflux pump(s), and producing enzymes that can inactivate the antibiotic by hydrolysis or modifications (e.g. β-lactamases) [1, 6], these mechanisms are illustrated in Figure 1-2.

The method of changing the antibiotic binding site is a successful method that can be found for almost all classes of antibiotics, since the antibiotic often binds to its target with high specificity. Gram-negative bacteria are less permeable than Gram-positive bacteria to many antibiotics, due to their outer lipid membrane. Efflux pumps and porins are therefore major contributors to the resistance of some Gram-negative bacteria. Efflux pumps are often capable of recognizing multiple substrates, recognizing chemical properties rather than chemical structure, making many efflux pumps multi-drug resistant by increasing the expulsion. Porins are the most abundant protein on the outer membrane, and acts as a selective barrier. Both the porin size and number of porins may affect the ability of the drug to enter the cell [1, 7].

There are different types of antibiotics, used more or less frequently depending on the class. The different classes of antibiotics functions by different mechanisms; (i) β-lactams interfere with the cell wall synthesis, and are the most commonly used antibiotics, (ii) macrolides binds to the 50S subunit of bacterial ribosomes, preventing protein synthesis, (iii) aminoglycosides also prevents protein synthesis, by binding to the 30S subunit of bacterial ribosomes, and (iv) quinolones that inhibit topoisomerases, and prevent DNA replication [1].
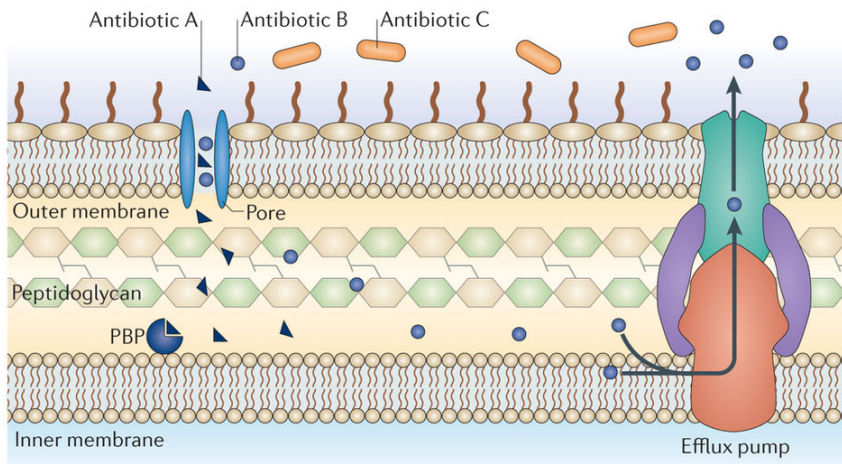
Figure 1-2: Illustration of different mechanisms of resistance in Gram-negative bacteria. The example shows β-lactam antibiotics targeting the penicillin-binding protein (PBP). Antibiotic A and B are able to enter the cell via a porin membrane protein. Antibiotic A reaches its target and can inhibit peptidoglycan synthesis. Antibiotic B cannot bind to its target, and is also removed from the cell by an efflux pump. Antibiotic C cannot cross the outer cell membrane, and hence cannot access its target. Figure from reference [1].

1.1.1   β-lactam antibiotics

Resistance to antibiotics typically appears within 2-3 years after clinical introduction and use [8], the rapid development of antibiotic resistance is especially clear for the β-lactam class [9]. The widespread resistance is due to β-lactams being the most commonly used antibiotic class [2].

β-lactams are bactericidal antibiotics, and act by inhibiting the bacterial cell wall synthesis. The peptidoglycan cell wall envelops the bacterial cell, with a thick outer layer for Gram-positive bacteria, and a thinner cell wall enclosed by a lipid bilayer in Gram-negative bacteria. The peptidoglycan cell wall is important for bacterial cells to define the cell shape and keep the cell from osmotic rapture. The peptidoglycan is made up of linear polysaccharide chains of alternating N-acetylglucosamine and N-acetylmuramic acid, cross linked by peptides, by the enzyme transpeptidase, also known as penicillin-binding proteins (PBP). PBPs bind to β-lactam antibiotics, because the β-lactams are structurally similar to the substrate (D-ala-D-ala) of PBPs. Inhibition of PBPs by β-lactams reduces cross-linking between the linear peptidoglycan chains, eventually causing cell wall degradation, and making the cell unable to withstand the osmotic pressure, causing cell rupture [7, 10].

β-lactams all have a four membered β-lactam ring in their structure core, and can be divided into four classes based on the structure; penicillins, cephalosporins, monobactams, and carbapenems. The chemical structure of the four β-lactam classes is shown in Figure 1-3.
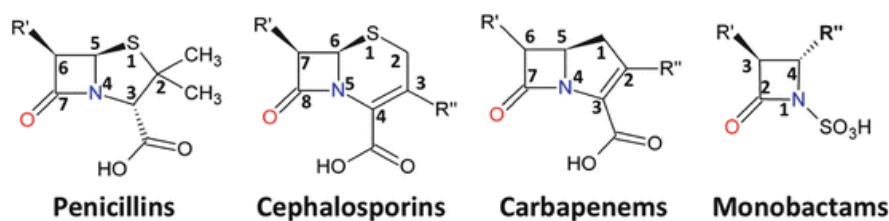
Figure 1-3: Chemical structure of the four different classes of β-lactam antibiotics in clinical use. The four membered β-lactam ring is the core of the structure. Figure from reference [7].

1.1.1.1   Penicillins

Penicillin is the oldest known β-lactam antibiotic, initially derived from *Penicillum* fungi. It was discovered by a coincidence in 1928 by Alexander Fleming, who was the first to describe its inhibition of bacterial growth. Ernst Chain and Howard Florey were the ones responsible for turning the discovery of penicillin into medical use, and received the Nobel Prize in Medicine in 1945 together with Fleming for their work.

The penicillin core consists of five-membered thiazolidine ring fused to the β-lactam ring, as illustrated in Figure 1-3. The penicillin family is divided into five basic classes; natural penicillins (e.g. penicillin G/ benzylpenicillin – early generation penicillins), penicillinase-resistant penicillins (e.g oxacillin), aminopenicillins (e.g ampicillin), extended-spectrum penicillins (e.g piperacillin), and aminopenicillins/ β-lactamase inhibitor combinations. The aminopenicillins were the first penicillin group to function against Gram-negative bacteria. Even though penicillins are important in modern medicine its extensive use has led to decreased efficiency and resistance [7, 11].

1.1.1.2   Cephalosporins

Cephalosporin C was the first in the cephalosporin subfamily to be discovered from the fungi *Chepalosporium acremonium* in 1948. It consists of a six-membered dihydrothiazine ring attached to the β-lactam core, and has two sites for attachment of different sidechains, giving a wider structural diversity compared to penicillins which only has one site for sidechain attachment, as shown in Figure 1-3 [7].

The closely related compound cephamycin is chemically similar to the structure of cephalosporins, and are sometimes classified as one, but was originally derived from the fungi *Streptomyces* and determined to be a separate class of β-lactams from the cephalosporins [12]. Cephalosporins are classified into 5 generations based on their antimicrobial properties; the first generation being the oldest classified cephalosporins, and the later generation having a

more extended-spectrum. Cephalothin is the oldest cephalosporin antibiotic in the first generation and was active towards most Gram-positive bacteria. The second generation had a slightly lower activity towards Gram-positive bacteria, but had an extended-spectra towards certain Gram-negative bacteria. An example of a second-generation cephalosporin is cefuroxime. Ceftazidime and cefepime are examples of third and fourth generation cephalosporins [13].

1.1.1.3   Monobactams

The only clinically approved and available monobactam is aztreonam, which is synthetically made. It differs from the other β-lactams by not having any ring structure fused with the β-lactam ring, as illustrated in Figure 1-3. Aztreonam is not widely used clinically since cephalosporins have a more extended-spectrum, but it is especially active against aerobic Gram-negative bacteria [7, 14].

1.1.1.4   Carbapenems

Carbapenems were developed from the discovery of thienamycin from *Streptomyces cattleya*, which turned out to be chemically unstable. This was overcome by the N-formimidoyl derivative, imipenem. The general structure of carbapenems is illustrated in Figure 1-3. Later, several different compounds have been derived from the original thienamycin. Some of the most clinically important are meropenem, ertapenem and doripenem, their specific structure of which, are shown in Figure 1-4 [15, 16].

All clinically used carbapenems have a 6-hydroxyethyl R1-sidechain, which is proposed to disrupt the hydrolysis step of the β-lactam ring. This sidechain is more compact than some of the penicillins and cephalosporins [17]. Other factors that are considered to make carbapenems especially difficult to hydrolyze are; firstly, the fused pyrroline ring (as opposed to thiazolidine in penicillins, and thiazine in cephalosporins), the presence of the double bond in the pyrroline ring gives a flatter ring structure and allows for tautomerization upon acylation (sp^2 or sp^3 hybridization of C-2). Secondly the C-6 atom stereochemistry is S instead of R as found for penicillins and cephalosporins [17]. See Figure 1-3 and Figure 1-4 for labelling of atoms and carbapenem core structure.

Carbapenems have a remarkably broad antimicrobial activity compared to other β-lactams, and are relatively resistant towards hydrolysis by β-lactamases. Carbapenems are still considered a "last defense" towards multi-resistant gram-negative pathogens. However, carbapenem resistance has spread rapidly, making carbapenems less and less useful. It is troubling that an increasing number of carbapenem resistant pathogens are discovered [7, 16].
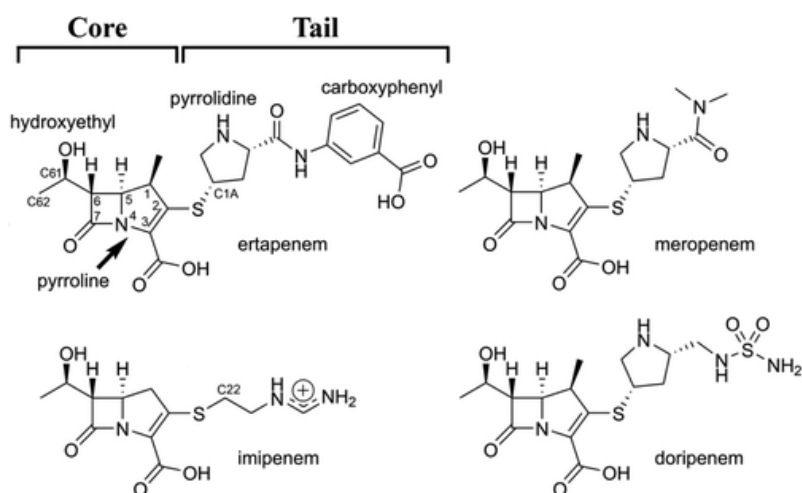
Figure 1-4: Structure of the carbapenem antibiotics; ertapenem, meropenem, imienem and doripenem. Certain functional groups are indicated, as well as the core and tail region. Figure from reference [18].

1.2   β-lactamases and the class D β-lactamases – Oxacillinases

The expression of β-lactamases is the most prevalent mechanism of resistance against the β-lactam class of antibiotics. By now over 4000 individual β-lactamases have been identified and reported, and the number is steadily growing (Beta-Lactamase DataBase, accessed 01.04.18) [19].

There are two possible classification systems for β-lactamases; the Ambler system, and the Bush-Jacoby-Medeiros system. The latter is a functional-based system grouping the enzymes in three main-classes (1; cephalosporinases, 2; broad-spectrum, inhibitor-resistant, extended-spectrum β-lactamases, and serine-carbapenemases, 3; metallo-β-lactamases) and subclasses, based on their substrate and inhibitor profiles. This is a more subjective system than the Ambler classification, but relates the varied enzymes to their clinical role [20, 21]. The most widely used classification system is the molecular classification, or the Ambler system, dividing β-lactamases into four groups (A-D) based on the amino acid sequence and structure [22]. Class A, C and D are serine-β-lactamases, with an active site serine, while class B are metallo-β-lactamases with a Zn^{2+} ion in the active site. The class A β-lactamases are the most common β-lactamases, and were the first β-lactamases to be identified, in penicillin resistant isolates [8]. Class D β-lactamases are often termed "oxacilliases" or OXA-enzymes, due to the original observation that members of this class had a strong hydrolytic activity towards the β-lactam oxacillin.

Class D β-lactamases are named using the OXA nomenclature and a number based on when they were discovered in time. Based on sequence identity class D β-lactamases are also divided into a number of subfamilies with >80% sequence identity. With more than 650 members in the class D subfamily, it is not the largest, but the fastest growing subfamily. It is also the most diverse class, of the four Ambler classes, both in terms of genetics and biochemical properties [23]. Class D β-lactamases can hydrolyze both narrow and extended spectrum antibiotics. OXA-enzymes are considered increasingly problematic as they can be found among human pathogens - clinically relevant Gram-negative species, such as *Acinetobacter baumannii, Pseudomonas aeruginosa* and Enterobacteriaceae (e.g *Klebsiella pneumoniae* and *Escherichia coli*) [23, 24]. In 2017 WHO published the first ever list of "antibiotic resistant priority pathogens" for which new antibiotics are urgently needed, meant as a tool to ensure that research is focused on public health needs. Listed as the most critical pathogens are the carbapenem resistant *Acinetobacter baumannii, Pseudomonas aeruginosa*

and Enterobacteriaceae [25]. This highlights the need for a greater understanding of how β-lactamases – especially those showing carbapenem resistance, functions and can be inhibited.

Class D β-lactamases genes can be located both on chromosomes and plasmids, and are also coexisting with other OXA-enzymes on the same plasmid. The horizontal gene transfer using plasmids and transposons, promotes a rapid evolutionary process within, and even between bacterial species [8].

Kinetically the class is quite diverse. Narrow-spectrum variant enzymes hydrolyze early generation penicillins and cephalosporins most effectively. Extended-spectrum variants are more problematic as the enzyme possess point mutations in the active site region that allow them to bind later generation cephalosporins with more bulkier side chains. But the most troublesome fact is that some OXA-enzymes are able to hydrolyze last resort antibiotics; carbapenem. The hydrolysis of carbapenems is slow, but with a high substrate affinity [24, 26].

1.2.1   Overall structure and reaction mechanism of class D β-lactamases

Despite class D β-lactamases being diverse, all OXA-enzymes display several conserved amino acid residues and motifs. The topological protein fold is highly conserved. The active site motifs Ser-Thr-Phe-Lys (amino acid number 70-73 using DBL numbering), Ser-Val-Val (118-120) and Lys-Thr-Gly (208-210) are found for all OXA-enzymes [23, 24].

In contrast to class A and C serine β-lactamases which are dominantly monomers, class D β-lactamases are both monomeric and dimeric. Each monomer has an independent active site. The OXA-enzyme fold is composed of two domains; one central β-sheet domain surrounded by α-helices, and one α-helical domain. The active site is found in the interface between the two domains, and is formed by a short 3_{10} helix. One side of the active site is made up by the omega loop (Ω), a loop with Ω shape and varying length. [26].

The general enzyme mechanism of serine-β-lactamases is widely accepted, where the active site serine hydrolyzes β-lactam antibiotics in a three-step model, as shown in equation 1-1.

$$(1\text{-}1) \qquad E + S \underset{k_1}{\overset{k_{-1}}{\leftrightarrows}} ES \xrightarrow{k_2} E - S \xrightarrow{k_3} E + P$$

8
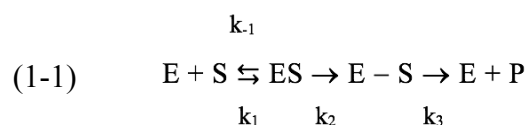
In the first step the enzyme interacts with the substrate forming into a Henri-Michaelis complex, which can either dissociate or form the acyl-enzyme complex. The acyl-enzyme complex is formed by a nucleophile attach by the active site serine, activated by a general base, forming an ester linkage to the β-lactam antibiotic. In the last step, the ester-linkage is hydrolyzed by an active site water molecule, activated by a general base. The product is released and the active site serine restored to its original state. The rate-constants k_1, k_2 and k_3 describe the binding, acylation and deacylation rates of the reaction. The reaction is made possible by the use of a general base (in hydrogen bonding distance to the active site serine), making the weakly nucleophilic hydroxyl group into a strong nucleophile [27-29].

Identifying the general base that activates the active site serine has been very challenging for all serine β-lactamases. After discovering the unusual N-carboxylation (covalent bond between amino acid side chain nitrogen and a carboxy group) chain and post-translational modification for Lys73 in OXA-enzymes, and enzyme inactivation upon decarboxylation, it was concluded that this residue acts as the general base for both the acylation and deacylation step [27, 30].

The formation of the carboxylated lysine in OXA-enzymes is favored by hydrophobic buried protein regions that lowers the pKa value, and local residues are able to stabilize the negatively charged deprotonated carbamate [31]. A study by Isom et al. on buried lysine residues, showed that the pKa value may be reduced by as much as 5 pH units, in favorable hydrophobic environments [32]. The very hydrophobic active site of class D β-lactamases, compared to class A and C β-lactamases allows Lys73 to exist in a deprotonated state at neutral pH for OXA-enzymes, able to react spontaneously with carbon dioxide forming the carboxylated lysine, characteristic for all class D β-lactamases [27].

The proposed general reaction mechanism for class D β-lactamases is illustrated in Figure 1-5, based on the reaction mechanisms presented in Leonard et al. [26] and Sun et al. [33]. First, the carboxylated Lys73 (KCX) acts as a general base, taking a proton from Ser70, making it a better nucleophile. Ser70 attacks the β-lactam ring carbonyl, yielding a covalent acyl-enzyme intermediate. The tetrahedral intermediate is stabilized by the main-chain amides of residue Ser70 and Tyr/Trp/Pro/Ala 211, and sidechain of Lys208. The easiest way of restoring the negatively charged lysine carbamate (enabling it to work as a general base and activating the active site water molecule) has been suggested to be a proton transfer to the β-lactam nitrogen leaving group using Ser118 as an intermediate. Ser118 is mostly found at hydrogen bonding distance to Ser70, while KCX is not. Often Ser118 is not close enough to the

carboxylate group, but found at hydrogen bonding distance to the carbamate nitrogen, and it is suggested that the proton may be transferred in this manner. The now restored general base KCX takes a hydrogen from an active site water molecule, the hydroxyl nucleophile will then attack the cleaved β-lactam carbonyl, releasing Ser70, which is restored with the hydrogen from KCX [26, 33, 34]. Another residue conserved among class D β-lactamases is Arg250, found in the active site. Arg250 is suspected of contributing to the catalysis by trapping the substrate, forming an ionic bond with the carboxylate group of the substrate, or stabilizing the transition state [34].
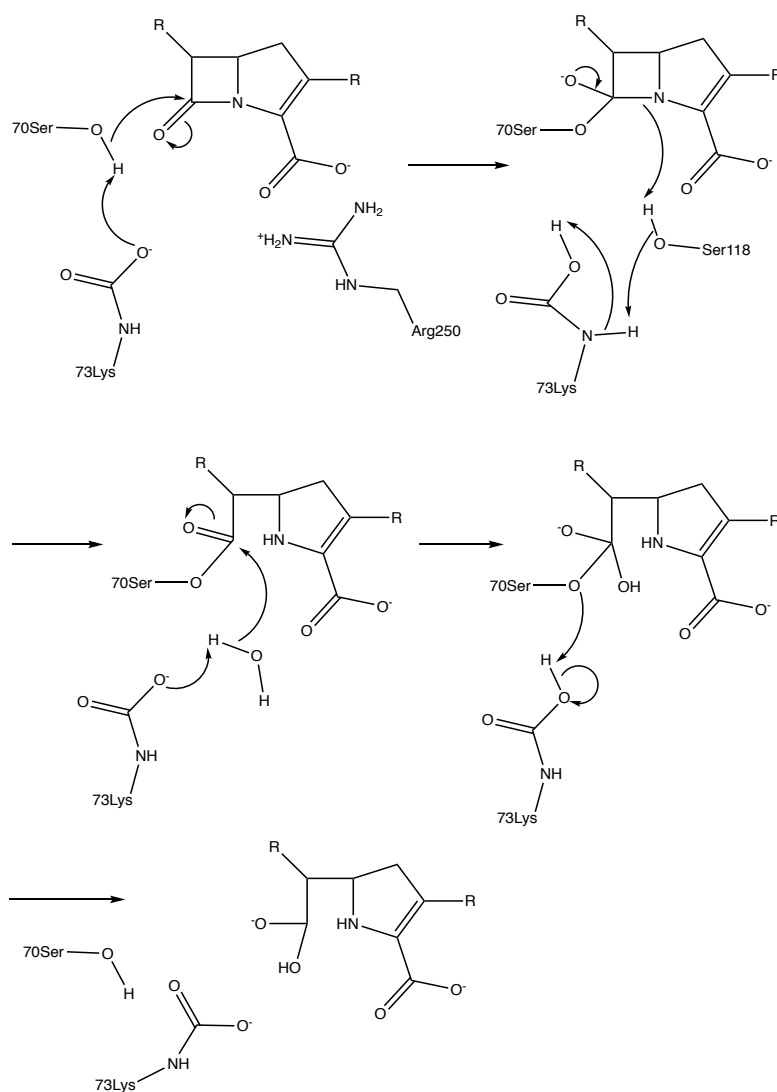
Figure 1-5: Proposed reaction mechanism for class D β-lactamases adopted from Leonard et al. [26], and Sun et al. [33], the movement of electrons are shown by curved arrows. The substrate is stabilized by an ionic interaction to Arg250 (showed only in the first step), Ser70 is activated by the carboxylated Lys73, and performes a nucleophilic attack on the β-lactam ring. The ring-structure opens and carboxylated Lys73 is restored to its deprotonated state through a proton transfer using Ser118 as an intermediate. Carboxylated Lys73 then acts as a general base again activating a catalytic water molecule, which attacks the carbonyl-group of the acyl-complex, leading to the release of the substrate.

The importance of the carboxylated lysine has been proven in multiple studies, showing that mutation of Lys73 lead to an inactive enzyme [26, 35]. The hydrophobic core surrounding Lys73 has also shown to be highly important for enzyme activity. Mutational studies on the residues Val120 and Trp157, has also shown to promote decarboxylation and enzyme inactivity [27, 36].

Other mutational studies focusing on the carboxylated lysine show that the mechanism (perhaps not surprisingly) is likely not so simple as described. For class D β-lactamases deacylation has proven to be the rate-limiting step. Despite the lack of a carboxylated lysine Vercheval et al. [37] and Schneider et al. [27] managed to show the formation of the acyl-enzyme intermediate, while the deacylation rate was almost completely stopped. Similar results have been shown for class A β-lactamases, being used as an argument for an asymmetric reaction mechanism – using two different residues as general bases [38]. However, as pointed out by Schneider et al. [27] the effect of mutation of residues essential to the enzyme mechanism should be considered with caution, the acylation (and lack of deacylation) may be effects of changes and adaptations in the active site upon mutating Lys73 [27]. The acylation and lack of deacylation (previously noted as enzyme inactivity) was also observed by Lund et al. [39] using surface plasmon resonance (SPR) to study interaction between substrate and OXA-48. Using a buffer without bicarbonate it was observed that acylation still was present, but deacylation only at a slow rate [39]. A possible explanation for why some enzyme activity is found with decarboxylated lysine in the active site could be found from the suggested reaction mechanism for class C β-lactamases. Here it is suggested that deprotonated lysine (not carboxylated) acts as the general base in the acylation step, or that the substrate carboxylgroup itself may act as a general base activating the active site serine [40].

Another study also show the complexity of enzyme mechanisms, by Sgrignani et al. [41] – using quantum mechanics/ molecular mechanics (QM/MM) calculations, suggests a different reaction mechanism for class D β-lactamase OXA-23 [41]. The study found that the simplest hypothesis of the direct proton transfer from Ser118 to the nitrogen of the β-lactam ring, was energetically highly unlikely. The most likely scenario was quite different; the acylation-step mechanism remained the same, but in the deacylation step the proton transfer to the nitrogen of the β-lactam ring would happen through another residue, Lys208, by stabilizing a water molecule, enabling the nitrogen to take a proton from the catalytic water. The hydroxyl would then act as a nucleophile (as previously explained). The carboxylated lysine will then

11

only contribute in transferring a proton to Ser70, restoring it [41]. This does seemingly not help explain why the deacylation step is particularly affected by Lys73 decarboxylation or mutation.

These slightly conflicting results hints at the reaction mechanism of class D β-lactamases being more advanced and intricate than currently understood, there are many residues involved, and highlights the need for further studies of both structural and functional aspects concerning the enzyme mechanistic details.

1.2.2 Carbapenem-hydrolyzing class D β-lactamases

Carbapenem-hydrolyzing β-lactamases can be found among class A, C and D serine-β-lactamases, common to them is the ability to hydrolyze a broad range of β-lactams, including extended spectrum cephalosporins and carbapenems. Class B metallo-β-lactamases are also carbapenemases. Carbapenemase producing pathogens are often multidrug-resistant, and difficult to treat, with high mortality rates. Class D β-lactamases were first identified on the chromosomes in a single bacteria species, with narrow substrate specificity, and not considered a great clinical treat. The discovery of class D β-lactamases able to hydrolyze carbapenems and cephalosporins changed this view. Many carbapenemases are now found on mobile genetic elements, and are reported in clinically important pathogens such as *A. baumannii, P. aeruginosa* and Enterobacteriaceae (especially *K. pneumoniae*) [1, 42].

Enterobacteriaceae is a bacterial family that inhabits the intestinal flora, and is among the most common human pathogens, causing both community and hospital-acquired infections. The first carbapenem resistant Enterobacteriaceae was reported in 1993, and has since spread worldwide. This is the cause of great concern due to the easy spread of this pathogen among humans, and the fact that carbapenem drugs are considered as "last defense" antibiotics in the clinic [43, 44].

Carbapenem-hydrolyzing class D β-lactamases (CHDLs) are defined as class D β-lactamases that produce clinical levels of resistance to carbapenem antibiotics. Enzymes belonging to the subfamilies OXA-23, OXA-24/40, OXA-48, OXA-51, OXA-58, OXA-143 and OXA-235 comprise over 200 enzymes which are classified as CHDLs [17]. All these enzymes were isolated form *A. baumannii* (with the exception of the OXA-48 like enzymes) [17]. Although only a selection of OXA-enzymes are considered to be CHDLs, a study by Antunes et al. [45] show that perhaps all class D β-lactamases are CHDLs. In the study, OXA-10 and OXA-2 which are considered narrow-spectrum enzymes (based on MIC values from these enzymes produced in *E. coli* or *P. aeruginosa*) was expressed in *A. baumannii*. The

strain is unique due to its low permeability and low antibiotic concentration in its periplasma, contributing to increased levels of resistance. OXA-10 and OXA-2 enzymes expressed in *A. baumannii,* turned out to in fact be CHDLs. This is clinically concerning, as there is a possibility that class D β-lactamases not previously considered to be CHDLs could display carbapenem resistance if expressed by these bacteria [45]. CHDLs have been reported increasingly in recent years [28]. One of the major concerns for attempting to control the CHDL spread are difficulties identifying the enzymes [23].

Determining the detailed reaction mechanism for carbapenem hydrolysis by CHDLs is an ongoing process, and several different mechanisms have been suggested, with arguments both for and against individual mechanisms among the different OXA subfamilies. Class D β-lactamases are as mentioned, a highly divergent class, both structurally and functionally. The apparent lack of conserved residues involved in carbapenem hydrolysis across different OXA subfamilies, has led to the conclusion that CHDLs utilize different evolutionary strategies, where specific residues give a local active site conformation capable of positioning the catalytic water molecule favorable for carbapenem hydrolysis. Crystal structures of OXA-24/40 and OXA-48 has been used to show this [28, 46].

The first carbapenem hydrolysis mechanism was suggested for OXA-24/40 from *A. baumannii* by Santillana et al. [47] who through crystallization and mutational studies identified that substrate specificity is affected by a hydrophobic barrier formed by Tyr112 and Met223, creating a tunnel-like entrance into the active site [47]. Later Schneider et al. [48] suggested that the hydrophobic bridge structure prevented tautomerization and the formation of sp^3 hybridized C-2 atom in the pyrroline ring (Figure 1-4), keeping the carbapenem substrate in the correct orientation and conformation in the active site, allowing for deacylation [17, 48]. A different mechanism was suggested by Docquier et al. [46] for OXA-48 from Enterobacteriaeae. OXA-48 have no hydrophobic bridge shaping its active site as OXA-24/40 do, and is as a result more "open". It was suggested that the specific conformation of the residues near the β5-β6 loop caused the hydroxyethyl-group of the carbapenem substrate to adopt a different rotamer and reposition, allowing for a distant active-site water molecule to get close enough to start the deacylation reaction [17, 26, 46].

Toth et al. [17] found that the conserved hydrophobic surface residue Val119 play an important role for the deacylation step of carbapenem in OXA-143 (a close relative of OXA-24/40), arguing that this might be an important part of a more universal reaction mechanism for CHDLs. Val119 was found to have two different conformations in the active site. In the first

both methyl groups are directed away from Ser70 ("open conformation"), while in the second conformation one of the methyl groups points towards Ser70 ("closed conformation"). The "open conformation" creates a small pocket around the active site residues, allowing for a water molecule to be present, and promoting deacylation. In the "closed conformation", the water will be positioned too far away from the active site residues. Binding of the substrate is quite specific, and upon binding, the hydroxyethyl sidechain of the carbapenem substrate will clash sterically with the "closed" conformation of Val119, locking it into the "open conformation". The formation of the acyl-enzyme complex in OXA-14, OXA-24/40 and OXA-23 leaves no space in the active site for the catalytic water molecule. However, the formed water-channel by the "open conformation" of Val119 solves this problem, and allows for deacylation [17].

The latest suggested reaction mechanism for carbapenem hydrolysis by class D β-lactamases, presented by Lohans et al. [49] show a new hydrolysis product, using NMR and MS. Rather than cleavage of the β-lactam ring, a β-lactone product is proposed to be formed instead, where the hydroxyl group of the hydroxyethyl carbapenem side-chain acts as a nucleophile in place of the water molecule required for hydrolysis [49]. The two possible reaction mechanisms and the structure of the two possible hydrolysis products are shown in Figure 1-6. In the study β-lacton formation by OXA-48 with different substrates were examined, suggesting that the β-lacton formation is dependent on a 1β-methyl substituent. It was suggested that the lactone formation only represented a competitive pathway if hydrolysis is disfavored. No β-lactone formation was observed for class A and B β-lactamases [49].

The results from different studies show that we have come closer to understanding the specific mechanism of class D β-lactamases, but still much is not known, the different findings hint at a larger more complex reaction mechanism than shown earlier. Further mutational studies affecting the enzyme active site, and enzyme activity, will be important to gain a greater understanding on the subject.
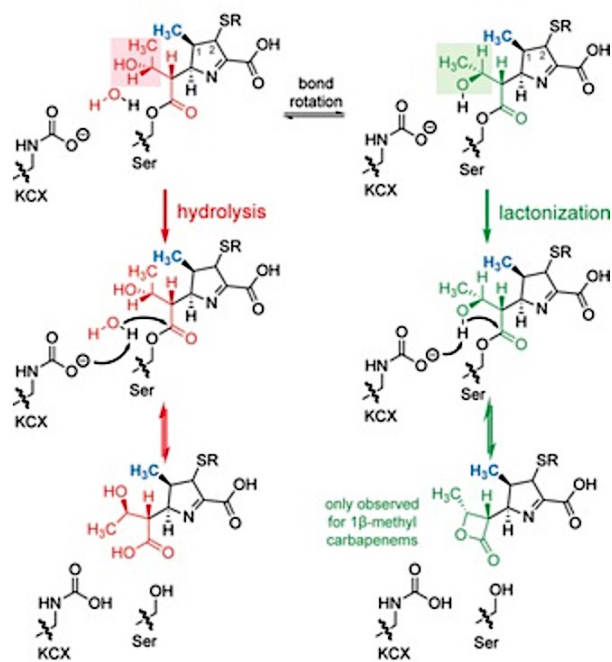
Figure 1-6: Proposed mechanism for suggested competitive carbapenem hydrolysis reaction through lactone formation. Hydroxy group acts as nucleophile instead of the catalytic water molecule. Ser is the active site serine, KCX is the carboxylated active site lysine functioning as a general base. 1β-methyl group important for lactone formation is marked in blue. Figure from reference [49].

1.3 OXA-48 and OXA-48 like class D β-lactamases

OXA-48 was first identified from a carbapenem- and multidrug- resistant *K. pneumoniae* isolate in Turkey in 2001. The identified *bla*$_{OXA-48}$ gene was plasmid located, and showed low amino acid sequence similarity with other class D β-lactamases, therefore being recognized as its own OXA-subfamily (46% identity with OXA-10, as the highest sequence similarity). Enzyme kinetics showed that OXA-48 hydrolyze penicillins at a high level and carpabenems at a low level, but had only a weak activity towards extended-spectrum cephaloporins [50, 51].

Since the discovery, OXA-48 producers have been identified worldwide in Enterobacteriaceae, even (rarely) in *A. baumannii*, and OXA-48 is one of the most geographically widespread members of the class D β-lactamases [43]. One of the reasons for the fast spread of OXA-48 producers, may be the difficulties in identifying these. Both the lack of a good phenotypic identification method, and the fact the *bla*$_{OXA-48}$ gene has a generally weak activity towards carbapenems, made the identification challenging [43, 51].

Some CHDLs have been shown to originate from *Shewanella*, a waterborne species. The main hypothesis is that insertion sequences (genetic tools) mobilized the chromosomal genes into plasmids which then transferred the gene into the more clinically relevant species. If the transfer was direct or was executed through an intermediate species is not clear, but *Serratia mercescens* has been suggest as an intermediate after *bla*$_{OXA-48}$ was identified in this enterobacterial pathogen from an aquatic environment [23, 51].

1.3.1 OXA-48 variants

Several OXA-48 variants have been identified since the discovery of OXA-48, differing only by a few amino acids. Figure 1-7 shows a sequence alignment of the different OXA-48 variants used during this thesis, namely OXA-48, OXA-163, OXA-245, OXA-436 and OXA-181. OXA-48 like variants have shown to be rather heterogeneous in terms of their hydrolytic profile, although being homologous in terms of protein sequence [52].

OXA-181 differs from OXA-48 by a four amino-acid substitution (T104A, N110D, E168Q and S171A), and generally show the same hydrolytic activity. Interestingly it is often found co-expressed with other carbapenemases, like metallo-β-lactamases. Despite the close sequence similarity, OXA-48 and OXA-181 has always been identified in distinct genetic contexts, suggesting that OXA-181 did not evolve from OXA-48 through mutations, but that the two occurred from mobilization of two different genes from two *Shewanella* strains [51].

OXA-163 is especially interesting in that it only differs from OXA-48 by a four amino-acid deletion (residue 214-217) and one amino-acid substitution (S212D) but has a different substrate specificity and hydrolytic profile. OXA-163 hydrolyses extended-spectrum cephalosporins, but carbapenems very weakly, making it more an extended-spectrum β-lactamase (ESBL) rather than a CHDL, as OXA-48 and other OXA-48 like variants [51, 53].

OXA-245 displays a quite similar hydrolytic activity to OXA-181 and OXA-48, and differs only from OXA-48 by one amino acid substitution (E125Y), the reason for this mutation is not completely evident [54].

OXA-436 is a newly identified OXA-48 like CHDL, isolated from patients in different hospitals in Denmark. Previously described OXA-48 variants differs only by > 97% in sequence identity, while OXA-436 has 90-93% sequence similarity to the other OXA-48 variants [55].
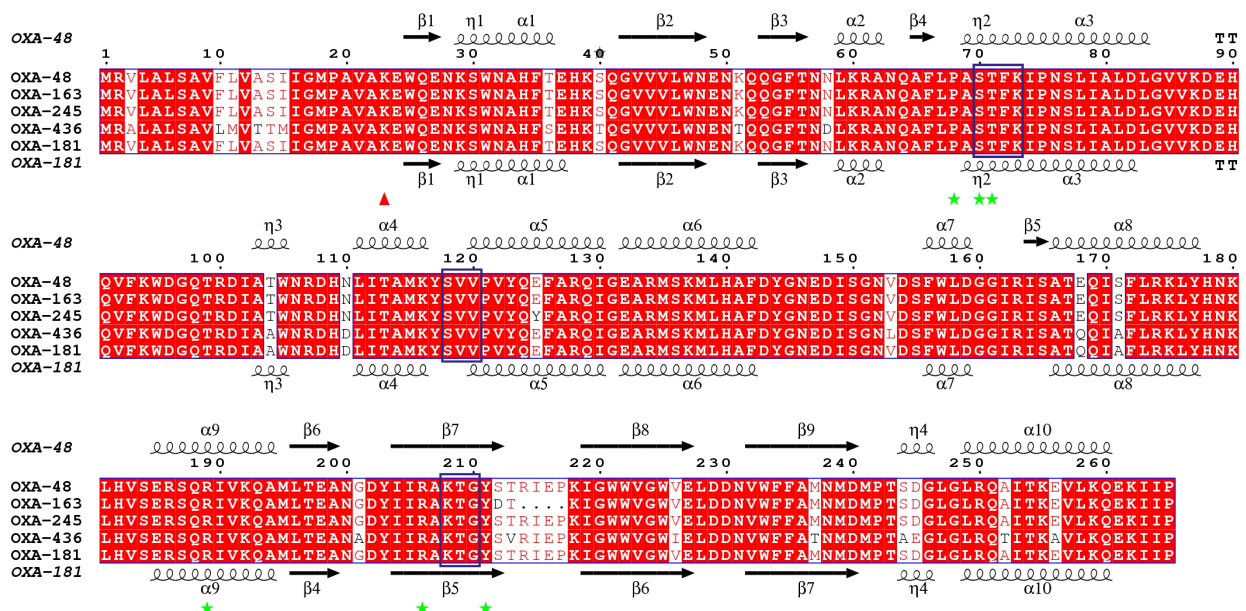
Figure 1-7: Sequence alignment of OXA-48, OXA-181, OXA-245, OXA-163 and OXA-436, with secondary structure elements from the crystal structures of OXA-48 (top, PDB: 5QB4) and OXA-181 (bottom, PDB: 5OE0). The residues are labelled according to the DBL numbering system. The conserved active site motifs are marked with blue frames, and the red triangle marks the end of the signal peptide. The green stars denote the substituted residues in the OXA-48 mutants investigated in this thesis. Figure was prepared using *ESPript* 3.0 [56] in collaboration with researcher Hanna-Kirsti S. Leiros.

1.3.2 OXA-48 structure and mutagenesis studies

1.3.2.1 Mutants affecting the dimer interface of OXA-48

It has been shown that some of the class D β-lactamases, including OXA-48, form homodimers, a protein-protein interaction where two identical polypeptide chains dimerize [35]. The binding affinity in a protein-protein interaction may vary a lot, with dissociation constants (K_d) spanning from μM to pM. The smaller the K_d value the stronger the binding affinity, and attraction between the polypeptide chains [57]. Studies on OXA dimerization for OXA-10, OXA-14 and OXA-29 determined K_d values from nM to μM range using gel filtration methods [58, 59]. For OXA-10 and OXA-14 divalent cations have been shown to facilitate dimerization, giving a more active dimer than monomer [58]. For OXA-48 a chloride ion was reported in the dimer interface bound between two amino acid Arg206, one from each protein chain upon dimer formation [39]. Chloride ions are known to form "packing bridges" connecting two adjacent protein chains, but are previously not known to be located in the dimer interface [60].

Compounds targeting the dimer interface may be useful inhibitors as some dimeric OXA enzymes have shown to be more active than the monomeric [58]. Targeting the dimer interface has been challenging due to the generally large surface of the dimer interface, and the lack of binding pockets. However, it has been shown that not all residues in the dimer interface are critical, but that most of the binding energy arise from small "hot-spots", often found near the center of the interface. This suggests that small molecule inhibitors may be used by targeting these "hot-spots" binding sites. Investigating the dimer interface is therefore important to be able to explore the possibility for such dimer inhibitors, and for elucidating the oligomeric state of the enzyme [61].

In a study by Dr. Bjarte A. Lund (unpublished data) an OXA-48 mutant affecting the dimer interface was designed; residue Arg206 binding a chloride ion was mutated to alanine. The effect of disrupting the chloride binding in the dimer interface was studied using size exclusion chromatography, differential scanning calorimetry (DSC), enzyme kinetics, and microscale thermophoresis (MST) (unpublished data). Size exclusion chromatography showed that both OXA-48 and OXA-48 R206A eluted as dimers, only at pH 4.0 did the enzymes elute as monomers, indicating the importance of the salt-bridges in the dimer interface. MST results were not obtained for OXA-48, but showed a remarkable low K_d value of 700 pM for OXA-48 R206A, indicating that the dimer interface of OXA-48 is more stable than of other class D β-

lactamases. DSC showed that OXA-48 had >4°C higher melting temperature than OXA-48 R206A, suggesting that the dimer formation is important for enzyme stability. No significant difference in enzyme activity was observed (unpublished data). A lower activity should in principle be observed, if the monomeric form was significantly less active than the dimeric form. It would therefore be interesting to design an even less thermostable OXA-48 mutant affecting the dimer interface, to better study the monomeric form and elucidate requirements for dimer formation (Figure 1-8 C).

Based on an *in situ* alanine scan, residues contributing to stabilizing the OXA-48 dimer were identified and ranked by suspected influence, as shown in Table 1-1. Based on these results it was decided to design two OXA-48 mutants in this study; one single mutant Arg189 to alanine (R189A), and one double mutant Arg189 to alanine and Arg206 to alanine (R189A/R206A). Figure 1-8 A shows the ribbon dimer structure of OXA-48, with residue interactions for R206 and R189 in the dimer interface (Figure 1-8 B), and the loss of interactions for the OXA-48 R189A mutant (Figure 1-8 C).

Table 1-1: Calculated energy differences from changing the residue to alanine using BioLuminate [62], and the chain A and D of OXA-48 (PDB: 5DTK). Top ten most influential residues are shown, mutating one or more of these will most likely influence and reduce the dimer stability. Calculations performed by Dr. Bjarte A. Lund.

Residue	Δ affinity (kJ/mol)
Arg189	189
Asp229	116
Lys116	104
Glu89	93
Arg206	82
Arg186	80
Leu196	79
Glu185	44
Arg107	39
Tyr117	38
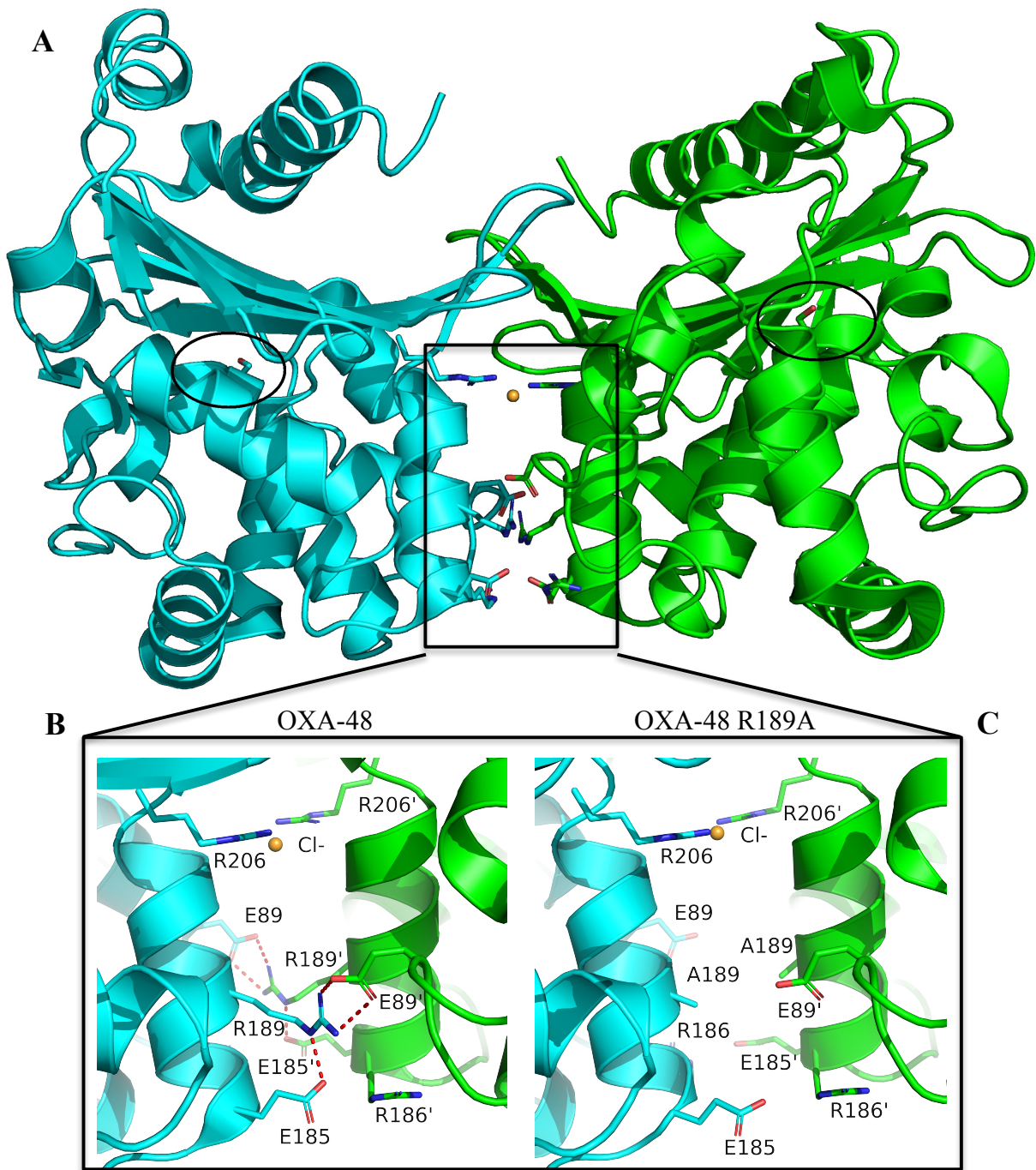
Figure 1-8: A) Proposed assembly of OXA-48 from a crystal structure (PDB: 5QB4), residues interacting with the dimer interface residues R189A and R206A are showed as stick figures. The active site residue S70 is also showed as a stick figure, and circled to highlight the active site. The chloride ion bound by residues R206 is shown as an orange sphere. **B)** Labelled residues with interactions to residue R189 showed as dashed lines. **C)** The lack of interactions for OXA-48 mutant R189A in the dimer interface, likely to contribute to reduced dimer affinity, from crystal structure of OXA-48 R189A. Ribbon structures made in PyMOL by researcher Hanna-Kirsti S. Leiros.

The active site of OXA-48 is a narrow crevice of 5x10x20 Å (width, depth, length). The catalytically relevant residues Ser70, Lys73 and Arg250 are spatially conserved [46]. The function of Ser70 as an active site nucleophile, and suggested reaction mechanism creating an acyl-enzyme complex was first suggested in the 1980s [63]. This led to multiple studies looking into the conserved active site motif involving Ser70. Mutational studies on the class A β-lactamase TEM, was conducted both with cysteine and threonine substitutions [64, 65]. The "thiol-β-lactamase", S70C, showed reduced, but detectable catalytic activity [65]. Another study using several different serine and threonine substitutions, showed no detectable activity for S70T, or S70T/T71S mutants. However, a Thr71 to serine mutant did not affect the catalytic activity drastically compared to TEM. The thermal stability was also shown to be affected; for the T71S mutant the thermal stability was reduced, while for the S70C mutant showed enhanced thermal stability. It was speculated that the additional methyl group of threonine may cause a too great sterically hindrance within the constraints of the active site, giving no activity for Ser70 mutants. The additional methyl group of Thr71 may act as a keystone to interlock with other segments of the β-lactamase polypeptide chain, being important for stabilizing the three-dimensional structure [64]. To our knowledge no mutational studies on Ser70/Thr71 substitutions have been conducted for class D β-lactamases. Three mutants were therefore designed; one single mutant Ser70 to threonine (S70T), and one double mutant Ser70 to threonine and Thr71 to serine (S70T/T71S), aiming for more insight into the importance of Ser70 and Thr71 in OXA-enzymes. The last mutant Ser70 to alanine (S70A) was design simply to have an inactive enzyme, for kinetic activity comparison. Figure 1-9 show the active site residues of OXA-48 with bound imipenem, including substituted active site residues in the mutants affecting the active site.

The combination of ceftazidime-avibactam (β-lactam/ β-lactamase inhibitor) was designed to treat infections caused by *Klebsiella pneumoniae* carbapenemases (KPC) carrying pathogens [66]. Ceftazidime and ceftazidime/avibactam is used against a broad range of β-lactamases, and it is possible that pathogens carrying the bla_{OXA-48} gene could be exposed to this treatment. Many pathogens carrying the bla_{OXA-48} gene, are multi-drug resistant, and a selective pressure of ceftazidime/avibactam on OXA-48 carrying bacteria might cause mutations to occur within OXA-48 conferring resistance towards this drug combination [51]. Organisms producing an enzyme with very low activity against a substrate, may evolve enzymes that are more efficient, when exposed to that substrate [28]. Emergence of resistance

to cephalosporin with inhibitor combinations has been reported for OXA-2 in *P. aeruginosa*. This is the first report of *in vivo* emergence of an extended-spectrum class D β-lactamase, during treatment of a human infection with broad spectrum cephalosporins [67].

Therefore, *in vitro* selection of an OXA-48 expressing *E. coli* strain against clinical relevant concentrations of ceftazidime, and ceftazidime/avibactam was conducted by PhD. student Christopher Fröhlich. Analysis of single point mutations within *bla*$_{OXA-48}$ revealed single and double mutations; P68A and P68A/Y211S after selection on ceftazidime and ceftazidime/avibactam, respectively (unpublished data). The identified mutations were close to the active site serine (S70) of OXA-48, and therefore likely to affect the catalytic activity. Figure 1-9 shows the placement of residue P68A and Y211S in the active site. In this thesis, the mutants P68A and P68A/Y211S were expressed and purified, to study the effect of the mutations on the enzyme activity with selected antibiotics.
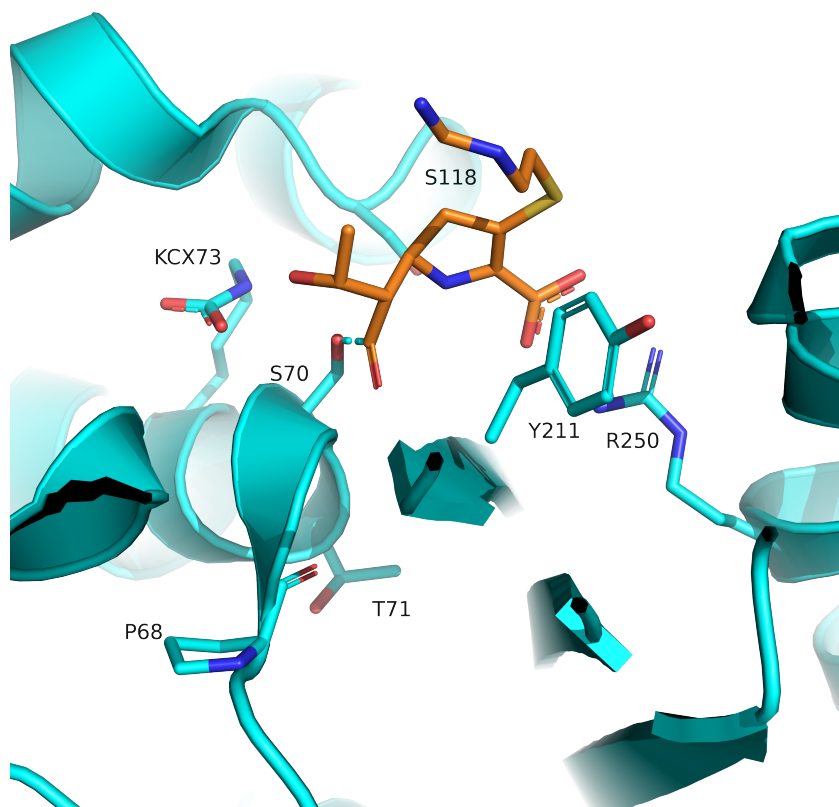
Figure 1-9: Proposed assembly of the active site residues in OXA-48 with bound imipenem, from a crystal structure (PDB: 5QB4). OXA-48 is displayed by ribbon structure in cyan, imipenem is shown in orange. The active site residues suspected of being important for the reaction mechanism, as well as the residues substituted in the active site OXA-48 mutants, are shown as stick figures. The figure was made in PyMOL, in collaboration with researcher Hanna-Kristi Leiros.

1.4 Classical β-lactamase inhibitors

During this thesis, the focus has been to study the stability, structure and enzyme mechanism, to gain more knowledge on this subject, also aiming for development of future OXA-inhibitors, and other solutions to the growing resistance problem. Only a brief mention of current inhibitors will therefore be given here.

To extend the use of existing β-lactam antibiotics β-lactamase inhibitors like culvanic acid, sulbactam and tazobactam were developed to coincide with the antibiotics already discovered. Culvanic acid was the first β-lactamase inhibitor introduced clinically in the 1970s. All three inhibitors are compounds that share structural similarity with penicillin, and are especially efficient towards class A β-lactamases. Avibactam is the first non-β-lactam β-lactamase inhibitor to be introduced clinically, in 2015. It has a broader spectrum activity than culvanic acid and sulbactam, inhibiting most class A and C β-lactamases, and even some class D carbapenemases. Unlike the previous inhibitors, avibactam is a tight binding reversible inhibitor for most enzymes (irreversible inhibitors bind irreversible to the enzyme causing a permanent inactivation) [68, 69]. However, resistance towards ceftazidime-avibactam combinations are already being reported for KPC (class A β-lactamase), showing the need for development of new β-lactamase inhibitors [70, 71].

1.5 Studying protein stability and activity

There are several different methods for studying protein stability and activity, focusing on different aspects. Only the methods used during this thesis will therefore be described here.

1.5.1 Differential scanning calorimetry (DSC)

Differential scanning calorimetry (DSC) is a powerful method for characterizing the stability of a system, and for directly determining the thermodynamic parameters; enthalpy ($\Delta H°$) and heat capacity change (ΔCp), as well as the melting temperature (T_m). DSC have many applications, and are commonly used to study protein denaturation, thermal protein stability, and folding mechanisms [72].

The heat capacity is a measure of the heat required to increase the temperature by 1°C for a given substance. The change in heat capacity of a compound reflects its ability to absorb heat. DSC functions by measuring small temperature differences between a sample cell, filled with the protein of interest in a desirable buffer, and a reference cell filled with the identical buffer. As temperature is increased, heat will be absorbed differently by the sample cell, from the reference cell. Additional heat will be added to keep the cells at the same temperature, the additional heat is then proportional to the to the excess heat capacity. DSC measures the excess heat capacity of a protein as a function of temperature. The transition midpoint temperature (T_m) is defined as the state where 50% of the protein is unfolded or denatured, while the rest is still in its folded or native state, this melting temperature is characteristic for each protein. The transition state is visible as a sharp endothermic peak, centred at the melting temperature in the thermogram (Figure 1-10) [72, 73]. When a protein reaches T_m a change in heat capacity will occur, due to uptake of heat to break interactions in the protein, going from the native to the denatured state. But a difference in heat capacity can also be observed before and after the transition state, since more heat is required to raise the temperature of a solution with unfolded protein, compared to the folded protein. This is mainly due to exposure of hydrophobic protein parts to the solvent. This shift in baseline is ΔCp, as illustrated in Figure 1-10. By including sample volume and protein concentration the specific heat capacity can be determined [73, 74].

Integration of the transition state curve yields the calorimetric enthalpy ΔH_{cal}, and represent the value of endothermic contributions such as disruption of hydrogen bonds, and exothermic ones, such as exposure of hydrophobic areas. The shape of the curve is an indication of the nature of the denaturation process. A sharp symmetric curve indicates a two-state model, which is currently the most popular mechanism used to describe protein denaturation processes.

Using this model, it is assumed that the protein unfolds directly from the native state to the denatured state, other states are assumed to be insignificantly populated. The two-state model can be verified by fitting a two-state vant's Hoff equation curve to the scan. From this, the vant's Hoff enthalpy is determined, which may differ from the calorimetric enthalpy [75, 76]. If the two enthalpies are similar, or more accurately if $\Delta H_{vH}/ \Delta H_{cal} \approx 1$ it can be assumed that the two-state model is correct. Values higher than 1 can indicate self-association of the protein, (e.g. assumed monomer is dimer), or the protein concentration may have been overestimated. Values lower than 1 indicates that the protein can unfold through several intermediate states, or the protein concentration may be underestimated. ΔH_{cal} may not be completely accurate as it is dependent on protein concentration, and hence can be affected by protein impurities and denaturation [72, 73].

DSC is a good method for studying thermal denaturation and protein stability, and is considered more accurate than Thermofluor and circular dichroism which are dependent on a spectroscopic signal [73].
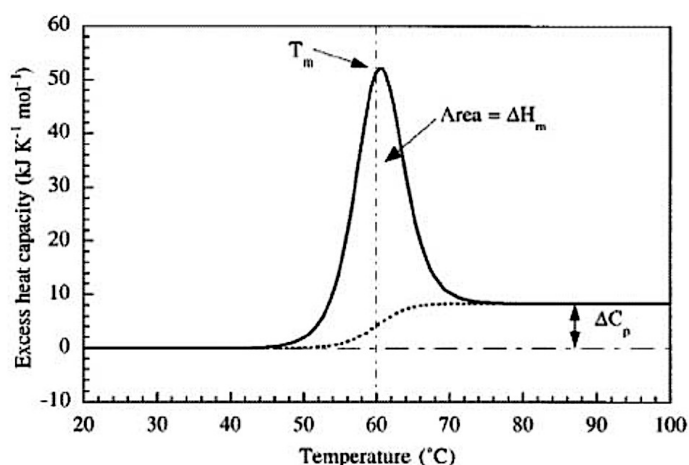
Figure 1-10: Illustration of a DSC thermogram – plotting heat capacity as a function of temperature. The melting temperature is shown in the centre of the transition state, and the integrated curve is the change in the calorimetric enthalpy (ΔH_{cal}). The difference in baseline before and after the protein transition is the heat capacity change (ΔCp). Figure from reference [72].

1.5.2 Microscale thermophoresis (MST)

Microscale thermophoresis (MST) refers to the motion of molecules in a microscopic temperature gradient [77]. The use of thermophoresis to quantify biomolecular interactions makes MST a unique method, since the binding-affinity measured by thermophoresis is dependent on multiple properties, not relying on the measurement of a single parameter as other methods do [78].

The temperature gradient in a solution with molecules induces a flow of molecules as well as a flow of heat. This coupling of heat- and mass-flow is known as thermophoresis or the Ludwig-Soret effect, its theoretical foundation is the subject of debate [77]. In general, the movement of molecules in a temperature gradient is described with a linear drift response; the molecular flow is linearly dependent on the temperature gradient, with a proportionally thermal diffusion constant [77-79].

The experimental setup of MST is illustrated in Figure 1-11 A, and is dependent on an infrared (IR) laser focused onto the sample through optics that is used for fluorescence detection. The IR-laser allows for very precise and reproducible heating of the sample, which is important since the general MST experiment involves interaction analysis of serial dilutions of 10-16 samples. The signal obtained by an MST instrument is shown in Figure 1-11 B, as a series of defined processes. The initial fluorescence is measured before heating the samples and should be constant. Turning on the IR-laser leads to a quick change in the fluorescence intensity, which is temperature dependent, referred to as the temperature jump. This is followed by the thermophoresis, where biomolecules will move with the thermal gradient dependent on their size, charge and hydration, weakening the fluorescent signal. When the IR-laser is switched off the inverse temperature jump can be observed, due to the fluorophore's temperature dependence, before the sample molecules diffuses back to its homogenous initial state (Figure 1-11 B). The difference in fluorescent on-signal (ΔF_{norm}) may be plotted against the protein concentration to give a dose-response curve from which the dissociation constant (K_d) can be derived [77, 78]. The use of fluorescence tags allows for higher sensitivity of the experiment, but unlabelled MST experiments can be conducted by measuring the fluorescence predominantly form tryptophan residues in the protein. For a typical MST experiment the concentration of a fluorescent labelled protein is kept constant (generally the concentration should be in the order of the expected K_d value or lower), with a dilution series of the unlabelled protein (starting concentration generally 10-20 times higher than the labelled protein) [77].
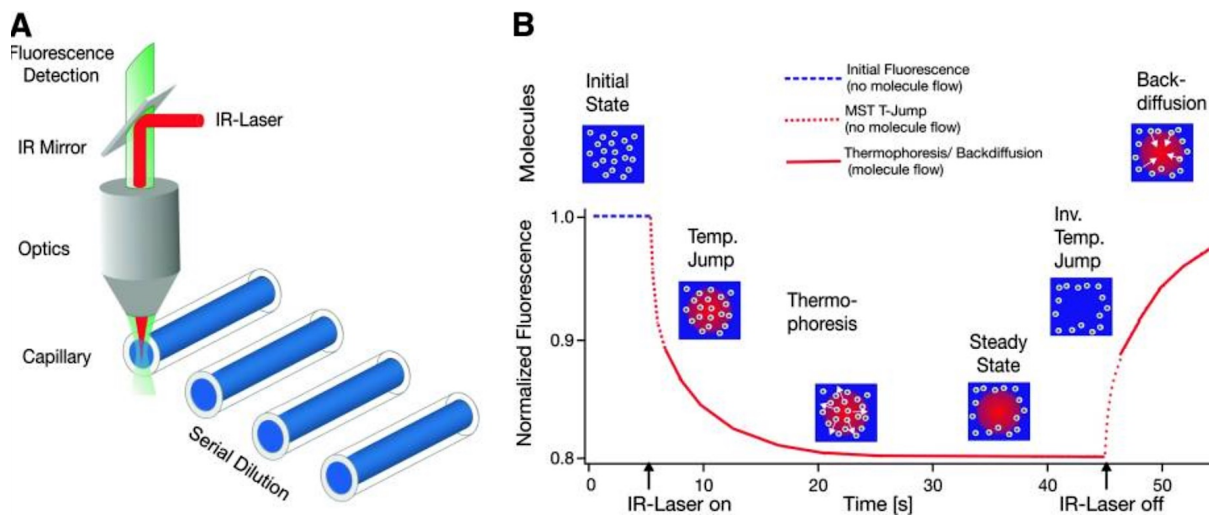
Figure 1-11: Overview of the experimental setup and a typical MST signal. **A)** An IR-laser is used to locally heat the sample volume in the capillaries, which is observed by fluorescence. **B)** A typical signal for a given capillary. When the initial fluorescence is measured the molecules in the sample are homogenous distributed. When the IR-laser is turned on a fast temperature jump is observed, followed by thermic molecule motion, and the fluorescent decrease is measured. When the IR-laser is turned off, the inverse temperature jump is observed, followed by a diffusion of molecules back to the initial homogenous state. Figure from reference [77].

1.5.3 Protein crystallization and X-ray crystallography

Obtaining a well-ordered protein crystal that can diffract X-rays strongly, is the first step for solving the three-dimensional structure of a macromolecule by X-ray crystallography [80]. Even though there are several challenges for determining the three-dimensional protein structure by this method, the protein crystallization step is somewhat of a bottleneck [81].

It is important to be able to obtain highly ordered protein crystals to retrieve high resolution diffraction patterns. The resulting three-dimensional protein crystal structure is not an image of the protein, but a map of the electron distribution in the protein. The X-ray scattering from a single molecule would be impossible to separate from the background noise, but by arranging the molecules in an ordered pattern the protein crystals functions as an amplifier (scattered waves adds up in phase), creating detectable diffraction spots [81]. The smallest repeating unit of a crystal is called the unit cell, each unit cell may contain one or more molecules. The arrangement of the unit cells makes up the symmetry of the protein crystal, and the crystal lattice [80].

Well-ordered protein crystals are difficult to grow because proteins are large molecules, with irregular surfaces, which creates large solvent-filled channels or holes in the crystal packing structure. The amount of solvent in the crystal structure may vary from 25-90% depending on the specific protein structure. This is one reason why protein structures determined by X-ray crystallography are very similar to the protein structure in solution. But the solvent filled-channels also creates larges spaces between adjacent molecules, causing some

molecules to not occupy exactly the same orientations, being the main reason for the limited resolution of the diffraction patterns [82].

There is no universal method for how to obtain macromolecular crystals. The methods applied for protein crystallization is therefore largely empirical in nature, remaining as what is basically a trial-and error approach. Protein crystallization is a matter of searching individual parameters affecting the crystallization, using patience, experience and intuition to identify successful factors. This may be done by systematically searching through the individual parameters, varying what is thought to be the most important factors, namely pH, temperature, protein concentration, precipitant type and use of additives. A more random search may prove to be more efficient. The use of crystallization robots and sparse-matrix crystallization kits, exploring a wide range of different conditions, has made the crystallization process more efficient. The sparse-matrix search may be good method for identifying promising conditions, but often becomes a matter of optimizing the protein crystallization [82].

Proteins will stay in solution up to a certain concentration, when this concentration is reached a new phase will appear. Proteins may form several different solid states, such as amorphous precipitates, oils and crystals. To create crystals the protein much first nucleate, or initiate development at high levels of supersaturation, 2-3 times higher than the level of supersaturation required for crystal growth [82, 83]. During nucleation, molecules associate forming a thermodynamically stable aggregate (nucleus) from which the crystal can grow [81]. The supersaturated state is a non-equilibrium condition in which some quantity of the protein is in excess, equilibrium is re-established by the formation of a solid phase [82].

The crystal growth and supersaturated state can be illustrated by a phase diagram, which can be an important tool for understanding when crystallization is likely to occur. The phase diagram is most often displayed as a two-dimensional graph as a function of the protein concentration and one other crystallization variable. When the protein solution is above its solubility limit it reaches the supersaturated state, which can be divided into three zones, depending on the level of supersaturation; metastable zone where crystal growth occurs, labile zone where nucleation occurs, and precipitation zone [81-83] (Figure 1-12).

As briefly mentioned, many parameters are found to affect protein crystallization. pH is considered one of the most important factors as it may alter the sidechain interactions of the proteins. Salts are also commonly used since they dehydrate the protein by competing for the water molecules. Organic solvents may change the dielectric constant of the protein solution, and some polymers produce volume-exclusion effects which may also cause the protein to become less soluble. Chemical agents that reduce the protein solubility is referred to as a

precipitant. Additives such as chemical protectants, poisons and solubilizing agents may also help, any substance other than the crystallizing compound, the buffer and the precipitant agent is considered an additive. Last, but not lest the temperature, protein concentration and protein sample homogeneity is important for the protein crystallization [81, 82].

There are different techniques for protein crystallization. The most commonly used is vapor diffusion, but batch crystallization, dialysis and free-interface diffusion may also be used. Vapor diffusion utilizes the evaporation of water from a drop containing the protein and the reservoir solution, to the same reservoir solution in a well, but at higher concentrations than found in the drop. Water will move from the place with lowest concentration to the one with the highest in an equilibrium. Commonly used set-ups are the sitting-drop method (drop deposited on a pedestal in the well), or the hanging-drop method (drop deposited on a cover slit above the well).
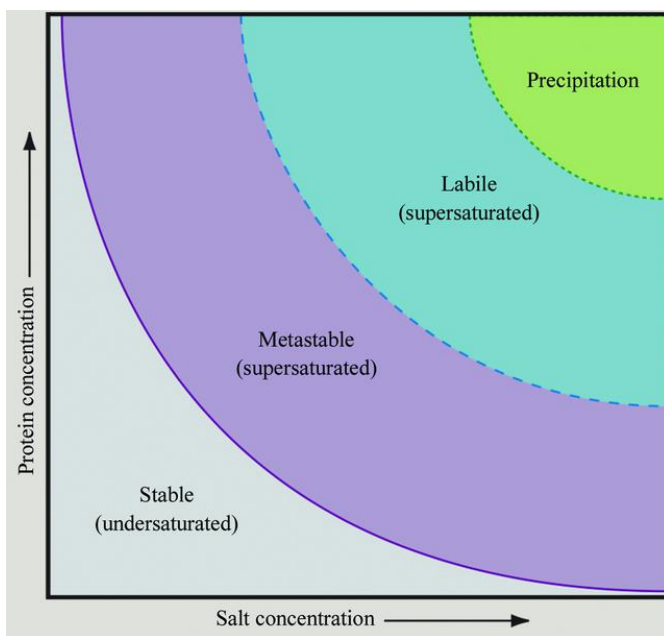
Figure 1-12: Phase diagram for the crystallization of macromolecules. The diagram is divided into regions of undersaturation (soluble protein) and supersaturation. The supersaturation zone can be divided into three separate zones; metastable zone where crystal growth occurs, labile zone where nucleation occurs, and precipitation zone. Figure from reference [82].

1.5.4 Enzyme kinetics

The determination of the enzyme reaction rate, commonly referred to as enzyme kinetics, and how it is affected by different experimental parameters, is an important method for studying proteins [84].

The Michaelis-Menten model is the foundation for enzyme kinetics, and is shown in equation 1-2. The model describes the rate of the reversible reaction where enzyme (E) binds to substrate (S), forming the enzyme-substrate(ES)-complex, and the irreversible reaction where substrate is converted to product. k_2 is the reaction rate at which the enzyme converts substrate to product and is referred to as k_{cat} or the turnover number. It is defined as the maximum number of substrate molecules converted to product per active site of the enzyme per unit of time [85].

$$(1\text{-}2) \qquad E + S \underset{k_1}{\overset{k_{-1}}{\rightleftharpoons}} ES \overset{k_2}{\rightarrow} E + P$$
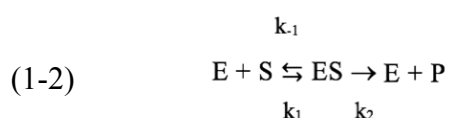
There are several assumptions implicit in this model; the enzyme binds only a single substrate, there is only one kinetically significant step between the formation of the ES-complex and the product formation, and the product formation is irreversible. This is not strictly correct for some enzymes, but is still a useful model [86].

A one-substrate enzyme-catalysed reaction can be described by the rate equation, or the Michaelis-Menten equation, shown in equation 1-3. It is based on a constant enzyme concentration in the reaction, and the steady-state assumption; the initial rate of the reaction reflects a steady state, in which the concentration of the intermediate ES-complex is constant. The formation of ES is equal to the consumption of ES [84, 86].

$$(1\text{-}3) \qquad v = \frac{V_{max}[S]}{K_m + [S]}$$

The K_m parameter is known as the Michaelis constant for the enzyme, and is the substrate concentration at which half-maximum reaction rate is observed. K_m can be used as a rough indicator of how tightly the enzyme binds the substrate (large K_m value indicates a weak interaction with the substrate). K_m is however not the true dissociation constant for the substrate, as it is also dependent on k_{cat}. The biomolecular rate constant k_{cat}/K_m is referred to as the overall conversion of substrate into product, and is considered to be the measure of catalytic efficiency of the enzyme [86]. V_{max} is obtained when the enzyme is saturated with substrate, when there are no available free enzymes to turn over more substrate, and is defined in equation 1-4 [85].

(1-4) $V_{max} = k_{cat}[E]$

The rate equation can be illustrated by the Michaelis-Menten kinetics curve, plotting the initial velocity as a function of the substrate concentration (Figure 1-13). As can be seen from Figure 1-13, the initial velocity v_0 increases almost linearly at low substrate concentrations. v_0 will be less and less affected by the increase in substrate until a plateau-like region is reached, where v_0 is close to the maximum velocity V_{max} [84].
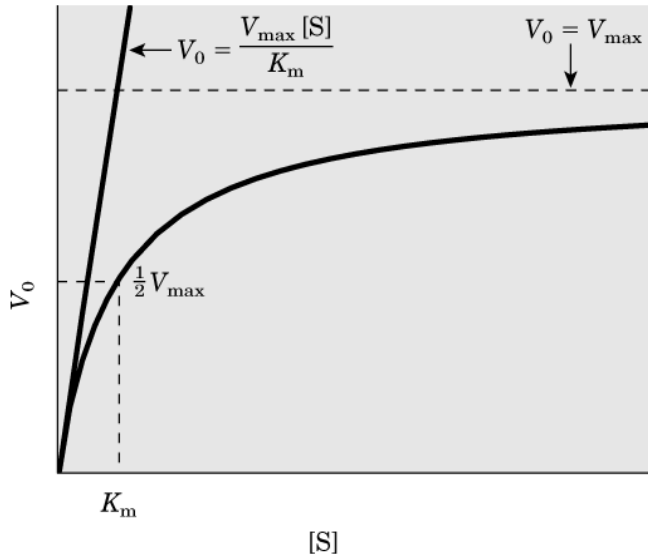
Figure 1-13: Plot of the initial velocity or reaction rate (V_0) as a function of the substrate concentration for an enzyme catalysed reaction, known as the Michaelis-Menten kinetics curve. V_{max} is the maximal velocity, K_m is the Michaelis constant, and is the substrate concentration at half of the maximal velocity. The initial velocity is related to the substrate concentration through the Michaelis-Menten equation (see eq. 1-3). Figure from reference [84].

2   Materials and methods
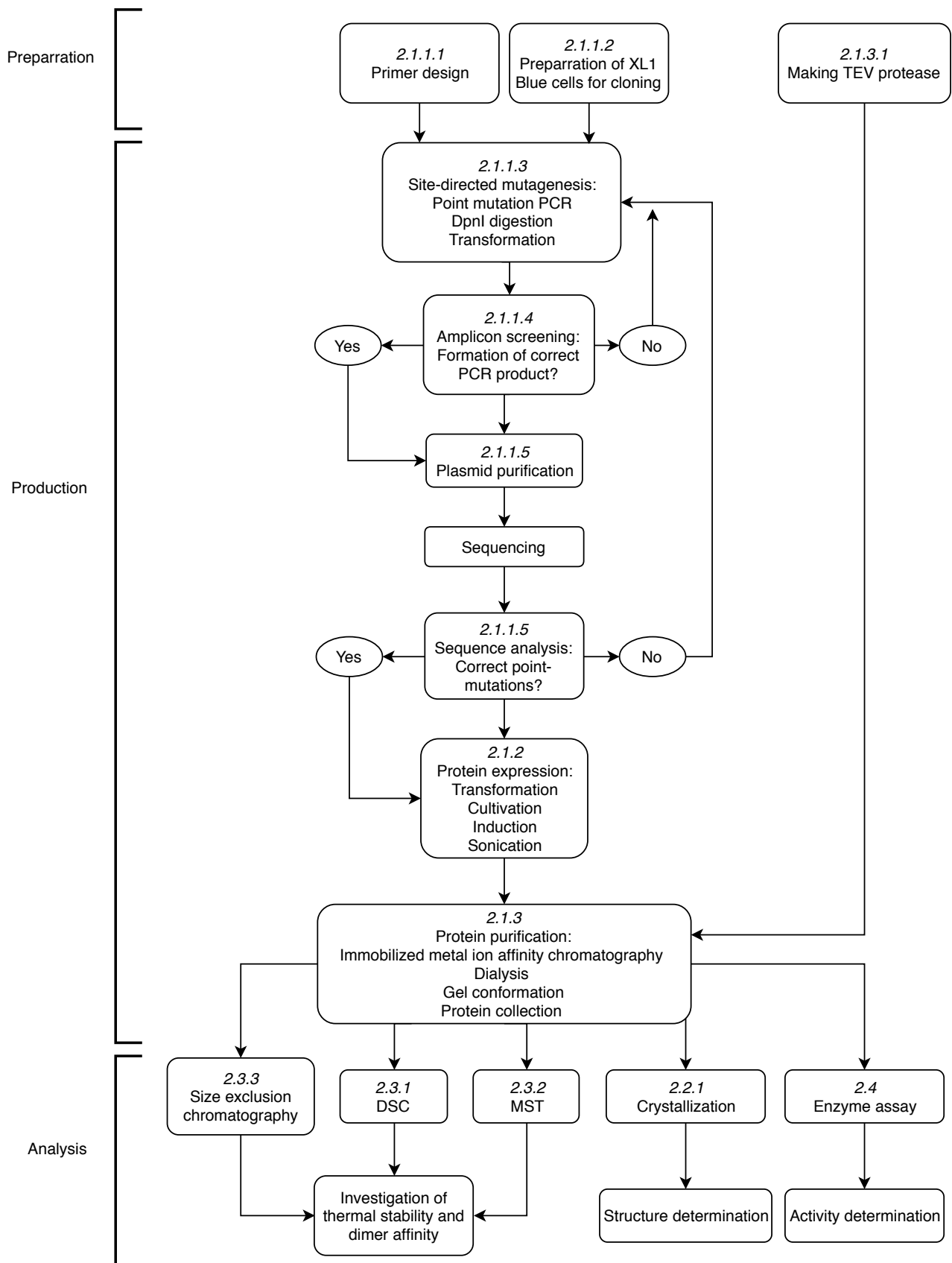
Figure 2-1: Schematic representation of work flow during this thesis, showing the laboratorial methods employed.

A major part of this thesis has been mutational studies of OXA-48 to investigate the active site, and the dimer interface. This was done to gain a greater understanding of how residue substitutions affect the enzyme activity and substrate specificity, as well as elucidating the oligomeric state of OXA-48, and study how specific mutations affect the thermal stability.

The OXA-48 mutants S70A, S70T, S70T/T71S, R189A, R189A/R206A, P68A, and P68A/Y211S were designed, expressed and purified. Mutants were then analyzed by different methods to investigate different aspects of the residue substitution(s), namely MST, DSC, size-exclusion chromatography, enzyme kinetics, and protein X-ray crystallography. Thermal stability and/or crystal structures were also used to investigate the effect of the residue substitutions and/or deletions between the OXA-48 like enzymes; OXA-181, OXA-245, OXA-163 and OXA-436. A schematic representation of the studies conducted in this thesis is shown in Figure 2-1.

2.1   Mutagenesis, protein expression and purification

2.1.1   Preparing OXA-48 mutants; R189A, R189A/R206A, P68A, P68A/Y211S, S70T, S70T/T71S, and S70A

Table 2-1: Solutions used for mutagenesis of OXA-48

Solution	Content
LB-agar (1 L)	10 g peptone 5 g yeast extract 10 g NaCl 15 g agar
LB-media (1 L)	10 g peptone 5 g yeast extract 10 g NaCl
Agarose gel	1% agarose in Tris-acetate-EDTA (TAE) buffer (heated, stored at 60°C)
TAE buffer	400 mM Tris pH 20 mM acetic acid 1 mM ethylenediaminetetraacetic acid (EDTA)
NZY$^+$ broth (1 L)	5 g NaCl 2 g MgSO$_4$ 5 g yeast extract 10 g N-Z amine (Casein hydrosylate)

2.1.1.1 Primer design for site-directed mutagenesis of OXA-48

It was decided to design 7 different OXA-48 mutants affecting both the active site and the dimer interface (see paragraph 1.3.2); R189A, R189A/R206A, P68A, P68A/Y211S, S70T, S70T/T71S, and S70A. To make these mutants, forward and reverse primer sets were designed based on the bla_{OXA-48} gene sequence (GeneBank: NC_019154), using the program QuickChange Primer Design (Agilent) [87]. For the double mutant P68A/Y211S two separate primer pairs were designed, due to the long distance between the target codons in the sequence. For R189A/R206A only the R189A primer were designed as the OXA-48 R206A was already available in the lab from previous experiments (unpublished data). The primer sequences are complementary to the bla_{OXA-48} gene, except for the target codon(s) to be substituted in the mutant. The primer pair sequences are shown in Table 2-2, with the R206A primers also included.

Table 2-2: Sequence of fwd. and rev. primer pairs for the OXA-48 mutants; R189A, R189A/R206A, P68A, P68A/Y211S, S70T, S70T/T71S, and S70A. Target codons are marked in red script, and exchanged nucleotides responsible for amino acid mutations are underlined. The melting temperature for the primer pairs are also included T_m, in °C.

		Primer sequence (5' - 3')
R189A T_m: 83.5	Fwd.	ATCGGAGCGCAGCCAGGCTATTGTCAAACAAGCC
	Rev.	GGCTTGTTTGACAATAGCCTGGCTGCGCTCCGAT
R206A T_m: 79.7	Fwd.	ACCGAAGCCAATGGTGACTATATTATTGCGGCTAAAACTGAT
	Rev.	ATCCAGTTTTAGCCGCAATAATATAGTCACCATTGGCTTCGGT
P68A T_m: 81.9	Fwd.	CGGGCGAACCAAGCATTTTTAGCCGCATCTACC
	Rev.	GGTAGATGCGGCTAAAAATGCTTGGTTCGCCCG
Y211S T_m: 78.0	Fwd.	TATTATTCGGGCTAAAACTGGATCCTCGACTAGAATCGAACCTAAG
	Rev.	CTTAGGTTCGATTCTAGTCGAGGATCCAGTTTTAGCCCGAATAATA
S70T T_m: 78.1	Fwd.	GAACCAAGCATTTTTACCCGCAACTACCTTTAAAATTCCCAATAG
	Rev.	CTATTGGGAATTTTAAAGGTAGTTGCGGGTAAAAATGCTTGGTTC
S70T/T71S T_m: 80.3	Fwd.	GAACCAAGCATTTTTACCCGCAACTAGCTTTAAAATTCCCAATAGCTTG
	Rev.	CAAGCTATTGGGAATTTTAAAGCTAGTTGCGGGTAAAAATGCTTGGTTC
S70A T_m: 79.1	Fwd.	GAACCAAGCATTTTTACCCGCAGCTACCTTTAAAATTCCCAATAG
	Rev.	CTATTGGGAATTTTAAAGGTAGCTGCGGGTAAAAATGCTTGGTTC

2.1.1.2 Preparation of XL1-Blue competent cells

Bacterial transformation is a process where bacteria take up foreign DNA, this may happen naturally. *E. coli* cells were made competent – making the cells more likely to take up foreign DNA. Making chemically competent cells involves treating the cells with Ca^{2+} ions, followed by a brief heat shock in the presence of foreign DNA, to allow uptake. This is referred to as the $CaCl_2$ method or heat-shock method [88, 89]. The presence of Ca^{2+} ions neutralize the negative repulsion between the foreign DNA and the phospholipid-heads of the cell membrane, making the uptake easier.

An "in-house" glycerol stock of the *E. coli* strain XL1-Blue was streaked on Lysogenic Broth (LB) -agar plates (Table 2-1) with 12.5 µg/mL tetracycline (TET), and left for incubation at 37°C, overnight (o/n). Two parallel pre-cultures were prepared, with 5 mL LB media (Table 2-1) with 12.5 µg/mL Tet, inoculated with one XL1-Blue cell colony each, and incubated at 37°C o/n. 100 mL LB media were inoculated with 1 mL pre-culture (1:100) and incubated at 250 rpm at 37°C until cell density/ optical density (OD_{600}) reached log-phase (0.3-0.9) [90]. The bacterial cultures were then centrifuged at 4000 rpm for 10 min at 4°C, before the media was carefully removed from the cell pellet. The pellet was resuspended in 10 mL ice cold 0.1 M $CaCl_2$ (sterilized solution), incubated on ice for 1 hour, before cells were collected by centrifugation. Finally, the pellet was resuspended in 2 mL 0.1 M $CaCl_2$ and 10% glycerol (sterilized solution), before being transferred to pre-frozen Eppendorf-tubes as 50 µL aliquots, and stored at -80°C.

2.1.1.3 Site-directed mutagenesis of OXA-48

For the site-dierected mutagenesis, a construct of bla_{OXA-48} in a pDEST17 vector with Ampicillin resistance (Figure 2-2) (prepared by PhD. Bjarte Lund) was used as a template, with the previously described primers, and the QuikChange II Site-Directed Mutagenesis Kit (Agilent). In the construct, a hexa-histidine tag had been inserted together with a TEV protease cleavage site, and a linker sequence (HHHHHH-LESTSLYG-ENLYFQG). While the predicted native leader sequence (residues 1-22, see Figure 1-7) at the 5′-end had been removed, normally transporting the protein from the cell interior to the periplasma [39, 91].
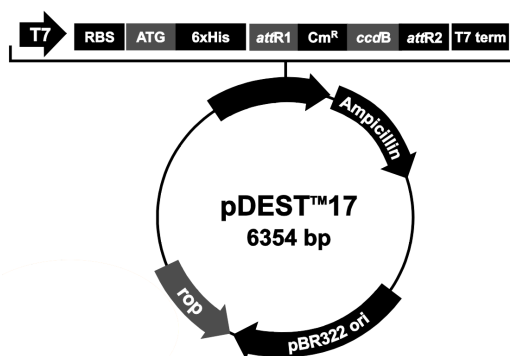
Figure 2-2: Illustration of the vector pDEST17. The gene of interest is inserted between the *att*R1 and *att*R2 sites (removing the Cm[R] and ccdB gene). Figure from ThermoFisher Scientific-Gateway pDEST17 vector map.

The mutant strand synthesis reaction was carried out according to the QuikChange II Site-directed Mutagenesis Kit supplied instruction manual (Agilent). Some modifications were applied to the manual, due to different optimizations of the site-directed mutagenesis process. The reaction was set up with approximately 50 ng template, 125 ng fwd. primer, 125 ng rev. primer, 2.5 µL 10x *PfuUltra* HF reaction buffer, 0.5 µL dNTP mix (10 mM each), 1% DMSO, and 0.5 µL *PfuUltra* HF DNA polymerase (2.5 U/µL). Nuclease-free water was added to a final volume of 25 µL, for each mutant. Samples were mixed by flicking the PCR tubes, before a brief centrifugation. Mutant strand synthesis reaction was performed using Thermo Scientific Arktik Thermal Cycler with the following Polymerase Chain Reaction (PCR) -conditions: initial 30 sec denaturation at 95°C, 16 cycles of [30 sec denaturation at 95°C, 1 min annealing at 60°C, 5.5 min elongation at 68°C], before cooling to 37°C. These conditions were used for all the mutants with the exception of OXA-48 P68A/Y211S, where the conditions were modified slightly; initial 30 sec denaturation at 95°C, 16 cycles of [30 sec denaturation at 95°C, 1 min annealing at 55°C, 6 min elongation at 68°C], before cooling to 37°C.

The amplified products were treated with 0.5 µL DpnI (10 U/µL), and incubated at 37°C for 1 hour. This was done to remove the non-mutated template. DpnI recognizes a commonly methylated sequence by *E. coli*. Mutated DNA created in the PCR process will not be methylated, and hence is not affected. 2 µL DpnI treated DNA was added to 50 µL XL1-Blue competent cells and mixed carefully. The cells were then heat-shock treated; incubated on ice for 30 min, transferred 42°C water-bath for 45 sec, before 2 min on ice. The cells were then incubated in 0.5 mL preheated NZY[+] broth (Table 2-1) at 37°C and 225 rpm for 1 hour, and spread on LB-agar plates with 100 µg/mL ampicillin (Amp). For OXA-48 P68A/Y211S mutant LB-agar plates with 50 µg/mL Amp were used instead. Plates were incubated o/n at 37°C.

2.1.1.4 *Amplicon screening and DNA analysis with gel electrophoresis*

PCR amplification reaction was conducted for the constructs and analyzed by gel electrophoresis. The thermophilic Taq DNA polymerase was used for this purpose. It is commonly used to amplify PCR products of 5 kb or less, but has no proof reading activity. For routine PCR amplification the Taq polymerase is sufficient, but for mutation analysis of amplified product *Pfu* DNA polymerase (which has one of the lowest error rates of all known thermophilic DNA polymerases) should be used [92].

For each mutant construct 3 colonies were picked for colony PCR, using a sterile pipette tip, lightly stroked onto a LB-agar 100 µg/mL (or 50 µg/mL) Amp plate (reference plate), and transferred to reaction mix; 22.5 µL Taq DNA polymerase 1.1x Master Mix RED (Ampliqon), 1 µL T7 primer fwd. (0.4 mM), 1 µL T7 primer rev. (0.4 mM), and 0.5 µL ddH$_2$O. In addition to the mutant construct samples, one negative control (only reaction mix), and one positive control (reaction mix and 10 ng pDEST17 *bla*$_{OXA-48}$ construct) were prepared. The reference plate was incubated at 37°C for minimum 6 hours. PCR-conditions used for amplicon screening; initial 5 min denaturation at 98°C, before 30 cycles of [30 sec denaturation at 98°C, 30 sec annealing at 55°C, 30 sec elongation at 72°C], before termination with 7 min elongation at 72°C, and finally cooling to 10°C.

The PCR reaction products were analyzed using gel electrophoresis. 1% agarose gel (Table 2-1) was casted with 0.05% (w/v) RedSafe nucleic acid staining solution (ChemBio). The gel was run with 1xTEA buffer (Table 2-1) at 90V for about 45 min, to separate DNA fragments. For OXA-48 S70T, S70A, R189A and S70T/T71S mutants 10µL PCR product was loaded directly to the wells, using 5 µL 0.1-12 kbp DNA ladder (Invitrogen) as a standard. This gave overloaded samples and a very weak ladder, but still a visible result. For the OXA-48 P68A, P68A/Y211S, R189A/R206A mutants 5 µL PCR product was loaded to the gel, using 10 µL ladder, instead. The gel and DNA-bands were analyzed under UV-light using Geldoc (BioRad).

2.1.1.5 Plasmid purification and Big-Dye 3.1 sequencing

A bacterial colony from the reference plate was picked, for the OXA-48 mutants showing DNA-bands at the correct size on the agarose gel (~1 kbp for all mutants), transferred to 5 mL LB-media with 100 µg/mL (50 mg/mL) Amp, and incubated at 37°C and 225 rpm o/n. The Wizard Plus SV Minipreps DNA Purification System Kit (Promega) was used for plasmid purification. The purification was conducted as described in the System supplied protocol. 5 mL cell culture was harvested after incubation o/n, and centrifuged (4000 rpm, 15 min, 4°C), supernatant was removed. The cell pellet was completely resuspended in 250 µL Cell Resuspension Solution, and transferred to 1.5 mL sterile Eppendorf tubes. 250 µL Cell Lysis Solution was added to the samples, mixed by inverting the tube 4 times, and left for incubation in room temperature for 4-5 min until clearing of the cell suspension was observed. 10 µL Alkaline Protease Solution was added, incubated for 4-5 min, before 350 µL Neutralization Solution was added, and the bacterial lysate was centrifuged (13000 rpm, 15 min, 21°C). The cleared lysate (without precipitate) was then transferred to a Spin Column (inserted in Collection Tube) and centrifuged (13000 rpm, 1 min, 21 °C). 750 µL Column Wash Solution (diluted in 95% ethanol) was added to the Spin Column, samples were centrifuged, and flow-through was discarded. Procedure was repeated with 250 µL Column Wash Solution, before the Spin Column was transferred to a new Collection Tube. The plasmid DNA was eluted by adding 100 µL nuclease free water to the Spin Column. The DNA concentration of the purified plasmids were measured at OD_{280} using NanoDrop 2000c (Thermo Scientific), before storing samples at -20°C.

The purified DNA samples were prepared for Sanger sequencing (using BigDye 3.1), according to the BigDye Terminator v3.1 Cycle Sequencing Kit Protocol (Applied Biosystems). Approximately 200 ng purified DNA was mixed with 1 µL BigDye 3.1, 4 µL 5x Sequencing Mix, 1 µL T7 primer fwd/rev (0.5 mM), and ddH_2O up to 20 µL reaction volume. One fwd. and one rev. reaction was prepared for each OXA-48 mutant. The PCR cycle program was set to; initial 5 min denaturation at 96°C, 25 cycles of [10 sec denaturation at 96°C, 5 sec annealing at 50°C, and 4 min elongation at 60°C], before cooling to 10°C. The sample products were sent to the University Hospital of Northern Norway for BigDye 3.1 Sanger sequencing.

The sequences were analyzed to confirm the correct mutation, using the program BioEdit Sequence Alignment Editor Version 7.2.5.0 [93]. ClustalW [94] alignment was used to align the provided OXA-48 mutant sequences with the bla_{OXA-48} gene (GeneBank: NC_019154), to identify codon substitutions.

2.1.2 Protein expression of OXA-48 mutants, OXA-48 and OXA-163

Table 2-3: Solutions used for protein expression of OXA-48, OXA-163, and OXA-48 mutants

Solution	Content
SOC	2% tryptone 0.5% yeast extract 10 mM NaCl 2.5 mM KCl 10 mM MgCl$_2$ 10 mM MgSO$_4$ 20 mM glucose
LB-agar (1 L)	10 g peptone 5 g yeast extract 10 g NaCl 15 g agar
LB media (1 L)	10 g peptone 5 g yeast extract 10 g NaCl
1xSB (10 mL)	1.25 mL 0.5 M Tris pH 6.8 1.15 mL 20% sodium dodecyl sulphate (SDS) 1 mL 87% glycerol 0.5 mL 100% 2-mercaptoethanol 0.1 mL 0.1% bromophenol blue
Running buffer (BioRad)	25 mM Tris pH 8.0 192 mM glycine 0.1% SDS
TB media (1 L)	10 g peptone 5 g yeast extract 4.6 mL 87% glycerol 100 mL 10x TB salt
10x TB salt	0.72 M KH$_2$PO$_4$ 0.17 M K$_2$HPO$_4$

2.1.2.1 Protein expression of OXA-48 and OXA-163

The OXA-48 like enzymes OXA-181, OXA-245, OXA-436, and OXA-163 were needed for crystallization trials and DSC analysis. Purified OXA-181, OXA-245, OXA-436 in sufficient amounts were already available, only OXA-48 and OXA-163 were therefore expressed and purified. OXA-163 was a synthetic DNA gene optimized for *E. coli* expression, while the OXA-48 gene was cloned from *Klebsiella pneumoniae* samples.

OXA-48 had previously been successfully expressed by Dr. Bjarte A. Lund [39], and the same expression conditions were used. Glycerol stocks with OXA-48 and OXA-163 in the in house *E. coli* strains BL21(DE3)pLysS and BL21(DE3)pRARE were available, and were used to start pre-cultures.

Preheated 50 mL LB media with 100 µg/mL Amp and 34 µg/mL CAM was inoculated with one "scoop" from each glycerol stock, pre-cultures were left for incubation at 37°C and 225 rpm o/n. 5 mL pre-culture was added (1:100) to 4 x 500 mL Terrific Broth (TB) media (Table 2-3) with 100 µg/mL Amp and 34 µg/mL CAM, in cultivation flasks, and grown at 37°C and 180 rpm until log-phase was reached. The cell cultures were induced with 0.4 mM isopropyl β-D-1-thiogalactopyranoside (IPTG) (VWR) at log-phase, and expression was continued at 20°C o/n. Cells were collected by centrifugation (6000 rpm, 40 min, 4°C) and the cell pellets stored at -20°C before protein purification.

Before induction (BFI) and after induction (AFI) samples were collected and analyzed using sodium dodecyl sulphate-polyacrylamide gel electrophoresis (SDS-PAGE), to check the effect of the induction and protein expression. BFI and AFI samples were centrifuged at 13000 rpm for 1 min, and the pellet resuspended in 1x sample buffer (SB) solution (Table 2-3), heated to 96°C for approximately 5 min, and loaded (10 µL) to a 4-20% mini-PROTEAN TGX Precast Gel (BioRad). 5 µL Precicion Plus protein dual color marker (BioRad) was used as a ladder. The gel was ran using Running buffer (Table 2-3), for 35 min at 200 V. The gel was stained using SimplyBlue SafeStain (Novex) for 10 min after brief heating, and left to destain in ddH$_2$O on an orbital shaker.

2.1.2.2 Protein expression of OXA-48 mutants

Since the expression of OXA-48 worked well with the given conditions, it was decided to use the same conditions for expression of the OXA-48 mutants in large scale. Previously expressed OXA-48 mutants had generally shown a lower protein yield pr. liter of cell culture, compared to OXA-48 [95]. Since at least two of the designed OXA-48 mutants were expected

to affect the protein stability, it was decided to lower the induction temperature from 20°C to 18°C, and IPTG concentration from 0.4 mM to 0.1 mM. This was done to allow for a slower protein expression, and theoretically, less misfolding and increased protein solubility.

Since 2x 1 L TB media was used in the expression for each mutant (1 L used for the protein purification, 1 L extra in case of unexpected errors), it was decided to test the in house *E. coli* strain Rosetta2(DE3)pLysS, in addition to the BL21Star(DE3)pRARE strain. The Rosetta2(DE3)pLysS strain had previously shown to work well, when expressing OXA-181 (unpublished data). For the transformation of OXA-48 mutant constructs into the selected strains, 1 µL plasmid (50-60 ng) was added to 50 µL chemically competent cells, and heat shock protocol was followed (incubation for 30 min on ice, 45 sec at 42 °C, on ice for 5 min). 1 mL preheated Super Optimal broth with Catabolite repression (SOC) (Table 2-3) was added to the cells, and left for incubation at 37°C and 225 rpm for 1 hour. The cultures were spread (testing different concentrations – 50 µL gave the best result) on preheated LB-agar plates with 100 µg/mL Amp and 34 µg/mL CAM (50 µg/mL Amp and 34 µg/mL CAM for OXA-48 P68A/Y211S mutant), and left for growth at 37°C o/n.

One bacterial colony from both *E. coli* strains for each mutant was picked and used to inoculate 15 mL LB media with Amp/CAM. The pre-cultures were left at 37°C and 225 rpm o/n. 5 mL pre-culture was used to inoculate (1:100) 2x 0.5 L room temperature TB media with Amp/CAM. 7 mL pre-culture from the OXA-48 P68A, P68A/Y211S and R189A/R206A mutants were used to inoculate 2x 0.5 L TB media, as previously expressed OXA-48 mutants (S70A, S70T, S70T/T71S, R189A) grew quite slowly. The cell cultures were grown until log-phase was reached, at 37°C and 180 rpm. At log-phase the cell cultures were induced by 0.1 mM IPTG, expression was continued at 18°C and 180 rpm o/n. The cells were collected by centrifugation (6000 rpm, 40 min, 21°C) and stored at -20°C.

From the pre-cultures 500 µL were collected to make glycerol stocks (carefully mixed with 500 µL 89% glycerol), and sored at -80°C.

SDS-PAGE analysis of the BFI and AFI samples was conducted as previously described, for the OXA-48 P68A, P68A/Y211S and R189A/R206A mutants. For the OXA-48 S70A, S70T, S70T/T71S and R189A mutants SDS-PAGE analysis of the BFI and AFI samples was attempted, but the samples were simply too sticky to allow loading of samples to the gel.

2.1.3 Immobilized metal ion affinity chromatography (IMAC) purification of OXA-48 mutants, OXA-48, OXA-163 and TEV protease

Table 2-4: Solutions used for protein purification using immobilized metal ion affinity chromatography, for OXA-48, OXA-163, TEV protease, and OXA-48 mutants.

Solution	Content
Running buffer (BioRad)	25 mM Tris pH 8.0 192 mM glycine 0.1% SDS
2xSB (1 mL)	500 μL NuPAGE LDS SampleBuffer (4x) (Invitrogen) 400 μL ddH$_2$O 100 μL 2-mercaptoethanol
Buffer A	50 mM Tris pH 7.5 500 mM NaCl 10% glycerol 2 mM 2-mercaptoethanol
Buffer B	50 mM Tris pH 7.5 500 mM NaCl 10% glycerol 2 mM 2-mercaptoethanol 500 mM imidazole
Buffer C	50 mM HEPES pH 7.0 200 mM NaCl 80% glycerol 2 mM 2-mercaptoethanol 1 mM EDTA
Buffer D	50 mM HEPES pH 7.2 50 mM K$_2$SO$_4$
Buffer E	50 mM HEPES pH 7.2 50 mM K$_2$SO$_4$ 500 mM imidazole
Buffer F	50 mM HEPES pH 7.2 50 mM K$_2$SO$_4$ 300 mM NaCl 2 mM 2-mercaptoethanol

2.1.3.1 Protein purification of TEV protease

Transformation of two TEV protease variants; TEVsh (amino acid substitution T17S, N68D, I77V) [96] and TEVpM2 (amino acid substitution T17S, L56V, N68D, I77V, S135G, S219V) [97] (in pTH24 vector, with His-tag) into Rosetta2(DE3)pLysS cells was attempted without success, using an in house protocol based on paper by van den Berg et al. [96].

Due to problems with the TEV expression, one frozen TEVsh pellet from a previous expression (2014) was provided, for purification (herby simply referred to as TEV). 90 mL Buffer A (Table 2-4) was added to the thawed pellet, together with one tablet of EDTA-free protease inhibitor cocktail (Roche Diagnostics). Cells were disrupted by sonication, using 5 seconds pulses with 9 seconds intervals, 35% amplitude, for approximately 1.5 hours total. 10 µL whole cell (WC) sample was collected from the disrupted cells, and mixed with 10 µL 2x sample buffer (SB), for SDS-PAGE analysis as previously described. The supernatant containing soluble proteins was collected by centrifugation (14000 rpm, 40 min, 4°C). 10 µL cell supernatant (CS) sample was collected and mixed with 10 µL 2xSB, before purification of the collected supernatant was started.

Since the TEV protein was constructed with a His-tag for IMAC protein purification, a 5 mL HisTrap FF crude column (GE healthcare) was used. The His-tagged protein have a strong affinity for the nickle-column [98]. ÄKTA prime plus system, and the computer program PrimeView Evaluation (GE Healthcare) were used for the purification, with flowrate set to 2.5 mL/min, 0.5 mPa pressurelimit, and 0.5 mL collected fractions. 5% Buffer B (Table 2-4) was added to the bacterial lysate before purification was started, and the column was washed with ddH$_2$O, before equilibration with Buffer A, and 5% Buffer B (approx. 5 column volumes). The protein sample was injected using a 150 mL super-loop connected to the ÄKTA prime plus system. The injected sample was loaded onto the column using Buffer A and 5% Buffer B. After the flow-through (non-binding proteins), the system was washed with 1 column volume of buffer before a Buffer B gradient from 5-100% over 70 mL was started (imidazole gradient from 25-500 mM). Imidazole functions as a metal ion ligand, reducing the His-tag binding affinity to the Ni^{2+} ions in the column, and eluting the His-tagged TEV protease [98]. This is visible as a protein elution peak in the chromatogram. Samples from the elution-peak fractions (as well as one from the flow-through) were collected for SDS-PAGE analysis as previously described. From the gel, it was determined that the protein was pure enough, and needed no further purification, as instability of the TEV protease could lead to reduced protein yield.

The collected protein fractions (selected from SDS-PAGE analysis) were pooled, and dialyzed o/n at 4°C in Buffer C (Table 2-4). NanoDrop 2000c Spectrophotometer (Thermo Sciences) was used to measure the protein absorbance at OD_{280}. The protein concentration was calculated using equation 2-1, by the NanoDrop software. The online program; ExPASy ProtParam tool [99] was used to determine the molecular weight (Mw) and the extinction coefficient based on the protein sequence.

$$(2\text{-}1) \qquad [Protein] = \frac{OD(A280) \times Mw}{extinction\ coefficient\ (\Delta\ \varepsilon)}$$

The protein sample was diluted to approximately 1 mg/mL, before storage at -80°C.

2.1.3.2 *Protein purification of OXA-48, OXA-163, and OXA-48 mutants*

The same purification conditions were applied for all the OXA-48 mutants, as well as for the purification of OXA-48 and OXA-163.

25 mL Buffer D (Table 2-4) was added to the thawed bacterial pellet, together with one tablet of EDTA-free protease inhibitor cocktail (Roche Diagnostics). Cells were disrupted by sonication, as previously described. The supernatant and soluble protein was collected by centrifugation (14000 rpm, 40 min, 4°C). WC and CS samples were collected for SDS-PAGE analysis. For the OXA-48 mutants the BL21Star(DE3)pRARE cell pellet was used for the purification, while the Rosetta2(DE3)pLysS was used if purification had to be repeated, due to errors.

The same ÄKTA prime plus settings as described for TEV protease were applied, using a 5 mL HisTrap HP column (GE healthcare). The column was washed in ddH$_2$O, and equilibrated using Buffer D (approx. 5 column volumes), before injecting the protein sample using a 50 mL super-loop connected to the ÄKTA prime plus system. The injected sample was loaded onto the column using Buffer D. After the flow-through, 5% Buffer E (Table 2-4) was loaded to the column (25 mM imidazole). A low imidazole concentration of 10-50 mM is used to elute weakly non-specific binding proteins from the nickle-column [98]. After the contaminants had been eluted, a Buffer E gradient from 5-100% was started, over 70 mL (25-500 mM imidazole), eluting the protein binding strongly to the column. Samples from the eluted-protein peak, flow-through and contaminant-peak was collected for SDS-PAGE analysis. Based on the SDS-PAGE results, fractions containing the protein of interest were

pooled, and left for dialysis o/n at 4°C in Buffer F (Table 2-4), with approximately 1 ml TEV protease (1 mg/mL), per 5 mL of collected protein sample.

In the second HisTrap purification step the His-tag has been removed from the protein, by TEV protease cleavage, and is therefore found in the flow-through. The settings and procedure were the same as for the first purification step, except for the Buffer E gradient being set from 0-100%. TEV and other strongly binding contaminant proteins were eluted during this gradient. Protein samples from the flow-through and one sample from the contaminant peak were collected for SDS-page analysis. Based on the SDS-PAGE OXA-48, OXA-163, and the OXA-48 mutants were determined to be more than 95% pure after this second purification step. No further purification was needed, the fractions containing the desired protein were pooled, and left for dialysis at 4°C o/n in Buffer D.

Protein concentration was measured using NanoDrop as previously described, and concentrated to around 10 mg/mL. For OXA-48, OXA-163, and OXA-48 S70T, 15 mL Amicon Ultra Centrifugal Filter (Millipore) with 10 kilo Dalton (kDa) cut-off membrane was used for the concentration. For the rest of the OXA-48 mutants it was decided to use Centriprep centrifugal filters (Merck) with 10 kDa cut-off membrane instead, due to a higher degree of protein recovery after the concentration.

2.2 Protein X-ray crystallography

2.2.1 Crystallization of OXA-48 mutants, and OXA-181, OXA-163 and OXA-436

2.2.1.1 Crystallization of OXA-163

A new crystal structure of OXA-163 was desired (previously published structures PDB: 5HAR, 4S2L, 4S2M). Favorable conditions from initial screening trials, conducted by Dr. Bjarte A. Lund, were used as a starting point for optimization trials. Two 24-well plates were set up manually at room temperature, using the hanging-drop method, around two conditions; 1) 0.1 M Tris pH 8.5, 26.5% PEG MME 500, from in house screening. 2) 0.1 M HEPES pH 7.7, 14% PEG 8000, from crystallization conditions for OXA-163 reported by Stojanoski et al. [100]. Micro crystals were obtained for several drops from the screen set up around the in-house conditions. Another optimization screen was therefore set up around the same conditions, varying the protein concentration systematically. Good crystals were obtained from this screen. The final crystallization conditions from the diffracting crystal are listed in Table 2-5.

Cryo solution were prepared identically to the crystallization conditions yielding good crystals, with 17% ethylene glycol (> 30% cryo protectant). With the assistance from Dr. Bjarte A. Lund crystals were transferred from the drop into the cryo solution, before being collected in a crystal mounting loop, and flash frozen in liquid nitrogen.

2.2.1.2 Crystallization of OXA-436

A crystal structure of the novel OXA-48 like, class D β-lactamase OXA-436 was desired. Multiple screens were set up using the Phoenix DT crystallization robot (Rigaku), in 96-wells MRC plates, with the sitting drop method (drop-size 500 + 500 nL, protein concentration 12.5 mg/mL). Structure screen 1 and 2, PGA screen, PACT premiere screen and SG1 screen were used for OXA-436 crystallization attempt. Multiple crystals were obtained from this, and other manually set up, optimization screens. It was however, discovered that most of the crystals were salt crystals. Most likely being $CaSO_4$, from a reaction between the $CaCl_2$ in many of the crystallization conditions and K_2SO_4 in the protein storage buffer. New SG1 screens with dialyzed OXA-436 in 50 mM HEPES pH 7.2, and concentrated dialyzed OXA-436 (25.1 mg/mL) were therefore set up using the crystallization robot. The latter gave a crystal for the conditions; 0.1 M HEPES pH 7.5, 0.2 M $NaCH_3COO$, 25% PEG3350.

An optimization screen for the given conditions was set up manually using the hanging-drop method. This gave one condition with good crystals. Another optimization screen was

fine-tuned around these crystallization conditions, with varying protein concentration. This also gave one condition with good crystals. The final crystallization conditions are listed in Table 2-5.

The crystals obtained from the two different optimization screens were transferred to the same cryo solution, as the crystallization conditions were very similar. 25% ethylene glycol was added, giving >30% cryo-protectant in the solution. The cryo-protecting and flash freezing of protein-crystals was conducted with assistance from Dr. Bjarte A. Lund.

Table 2-5: Crystallization conditions for OXA-163, OXA-436 and OXA-181. OXA-181 was not crystallized during this master thesis (expressed, purified and crystallized during bachelor thesis), but the structure was solved during this thesis, and the crystallization conditions is therefore included.

	OXA-163	OXA-436	OXA-181
Method	Vapor diffusion		
Plate-type	Hampton Research VDX 24-well plate with sealant		
Temperature (K)	294	294	294
Protein concentration (mg/mL)	9.4	25.1	11.1
Buffer composition of protein solution	50 mM HEPES pH 7.2, 50 mM K_2SO_4	50 mM HEPES pH 7.2	50 mM Tris pH 7.2, 50 mM K_2SO_4
Composition of reservoir solution	0.1 Tris pH 9.0, 28% PEG MME 500	0.1 M HEPES pH 8.0, 0.2 M $NaCH_3COO$, 26% PEG 3350	0.1 M Tris pH 7.0, 0.2 M $(NH_4)_2SO_4$, 20.5% PEG MME 5000
Drop volume (µL)	2	2	1
Reservoir volume (µL)	1000	1000	1000
Protein:reservoir ratio	3:20	1:1	1:1

2.2.1.3 *Crystallization of OXA-48 mutants; S70A, S70T, S70T/T71S, and R189A*

Previous in-house crystallization trials conducted by master student Birgit Nesheim, with different OXA-48 mutants showed good results for the conditions; 0.1 M BIS-Tris propane pH 9.0 and 9.5, 14-18% PEG MME 5000 [95]. Manually designed 24-well plate screens were therefore set up for the OXA-48 mutants R189A, S70A, S70T, S70T/T71S for the reported conditions at room temperature. This gave promising results with a lot of micro-crystals, and even some good crystals. New optimization screens with varying protein concentration were set up at 4°C. This also yielded some good crystals. But sufficiently large crystals were not yet

obtained for all the mutants. One manually set up, 24 well screen was also done at room temperature for the reported crystallization conditions of OXA-48 [101]; 0.1 M HEPES pH 7.5, 8-11% PEG 8000, 4-8% 1-butanol.

Two 96-well plate sitting-drop crystallization screens; SG1 and Structure screen, were set up using the new crystallization robot; NT8 – Drop Setter (Formulatrix). This showed crystal formation at very different conditions. It was therefore decided to design a 24 well crystallization screen spanning a broad pH and precipitant concentration range, with varying protein concentration at 4°C; 0.1 M BIS-Tris propane pH 6.5-9.5, 5-30% PEG MME 5000. The screens were set up using Formulator Liquid dispenser (Formulatrix).

Three crystals from each mutant was sent to the synchrotron. The final crystallization conditions for the diffracting crystals are listed in Table 2-6.

Cryo-solutions identical to the crystallization conditions, with ethylene glycol added to >30% cryo-protectant in the solution was prepared. The crystals were transferred to the cryo-solution, mounted, and flash frozen in liquid nitrogen, with the assistance of Dr. Bjarte A. Lund.

Table 2-6: Crystallization conditions for the OXA-48 mutants; R189A, S70A, S70T, and S70T/T71S

	R189A	S70A	S70T	S70T/T71S
Method	Vapor diffusion			
Plate-type	Hampton Research VDX 24-well plate with sealant			
Temperature (K)	294	277	294	277
Protein concentration (mg/mL)	7.6	10.1	12.8	11.9
Buffer composition of protein solution	50 mM HEPES pH 7.2, 50 mM K_2SO_4	50 mM HEPES pH 7.2, 50 mM K_2SO_4	50 mM HEPES pH 7.2, 50 mM K_2SO_4	50 mM HEPES pH 7.2, 50 mM K_2SO_4
Composition of reservoir solution	0.1 M BIS-Tris propane pH 9.5, 16% PEG MME 5000	0.1 M BIS-Tris propane pH 9.5, 38% PEG 400	0.1 M BIS-Tris propane pH 9.5, 19% PEG MME 5000	0.1 M BIS-Tris propane pH 8.5, 20% PEG MME 5000
Drop volume (μL)	3	2	3	2
Reservoir volume (μL)	1000	1000	1000	200
Protein:reservoir ratio	1:2	1:1	1:1	1:3

2.2.2 X-ray data collection and structure determination

The protein crystals (OXA-181, OXA-163, OXA-436, and OXA-48 mutants; S70A, S70T, S70T/T71S and R189A) were sent to the beamline 14.1 at BESSY II, Berlin, Germany. The diffraction data were collected by the NorStruct team.

The crystal structures for OXA-181 and OXA-436 were solved by Dr. Bjarte A. Lund. The crystal structures for OXA-163 and the OXA-48 mutants S70A, S70T, S70T/T71S and R189A were solved by researcher Hanna-Kirsti S. Leiros.

2.3 Protein stability

2.3.1 Differential scanning calorimetry (DSC)

Table 2-7: Solutions used for differential scanning calorimetry (DSC) for selected OXA-48 mutants, OXA-48, OXA-181, OXA-245, OXA-163, and OXA-436.

Solution	Content
Buffer G	50 mM HEPES pH 7.0 50 mM K_2SO_4
Buffer H	50 mM NaH_2PO_4/ Na_2HPO_4 pH 7.2

DSC analysis were conducted for the OXA-48 like enzymes OXA-181, OXA-163, OXA-436 and OXA-245 to investigate the differences between the enzymes. OXA-245 differs from OXA-48 only by one amino acid substitution. The experimental method was conducted according to the method description in the User`s Manual; model CSC 6300 Nano-Differential Scanning Calorimeter III chapter 4 [102]. OXA-245, OXA-181, OXA-163, OXA-48, and OXA-48 mutants; R206A, R189A, and R189A/R206A were analyzed in duplicate measurements, dialyzed against Buffer G and Buffer H (Table 2-7). OXA-436 was dialyzed only against Buffer G, and analyzed in duplicate measurements. All samples were dialyzed o/n at 4°C, with a few exceptions. The experiments were performed using a CSC N-DSC III instrument, and all data were analyzed using the program NanoAnalyze 3.6 (TA Instruments).

All solutions used; water, buffer, and protein samples were filtrated and degassed before use. The temperature gradient was set from 10-80°C, with an increase/decrease in temperature of 1°C/min. Protein sample concentration was in the range of 0.7-1.0 mg/mL.

For every experiment, a run with water in both cells were conducted first. Then both the reference and the sample cell were flushed with buffer once, before buffer was loaded to both cells, making sure there were no air bubbles in the cells. The system was pressurized to 3 atm, and the program could be started. This was done to allow for the determination of the experiment baseline. After one heating cycle, buffer was removed from the sample cell, and the protein sample added instead. After one more heating cycle, the program was ended. And data could be analyzed. For the clean-up of the DSC instrument, 50% formic acid was added to both cells, and an own formic acid program (25-80°C) was ran, without pressurizing the system. After completion of the program the cells were washed with 1 L ddH_2O, before water was loaded to both cells and the water-program was run again (4-110°C, multiple heating cycles).

2.3.2 Microscale thermophoresis (MST)

Table 2-8: Solutions used for Microscale Thermophoresis (MST) of OXA-48 R189A and R189A/R206A

Solution	Content
Buffer I	50 mM HEPES pH 7.0 50 mM K_2SO_4 0.05% Tween-20

To determine the dimer affinity of OXA-48 R189A and R189A/R206A a microscale thermophoresis experiment was conducted. The experimental method was conducted according to a previous MST experiment with the OXA-48 R206A mutant (unpublished data).

OXA-48 R189A and R189A/R206A were labelled using the Monolith NT Protein Labelling Kit RED-NHS (NanoTemper Technologies). According to the manufacturer's User Manual the proteins were diluted to 20 μM in the provided Labelling Buffer with a molar protein:dye ratio of 1:3, before being incubated at room temperature for 30 min in darkness. Unreacted dye was then removed using the supplied Gravity Flow dye removal Column. The column was equilibrated using 6 mL Buffer I (Table 2-8).

Three individual series of 16 two-fold dilutions of unlabeled OXA-48 R189A/R206A from 500 nM to 15 pM were prepared (MST analysis of OXA-48 R189A was unsuccessful). Labelled OXA-48 R189A/R206A was added to each dilution with a final concentration of 150 pM. Both labeled and unlabeled protein was diluted in Buffer I.

Samples were incubated for 10-20 min in room temperature, before being loaded into Monolith NT.115 Standard Treated Capillaries (NanoTemper Technologies). The Monolith NT.115 instrument (NanoTemper Technologies) settings were adjusted to 60% LED power, 40% (medium) MST power, and temperature of 25°C. Data from three measurements, using the signal from an MST-on time of 20 seconds, were analyzed using the MO.Affinity Analysis software version 2.1.3 (NanoTemper Technologies).

2.3.3 Size-exclusion chromatography

To further investigate the dimer stability, and how the dimer formation is affected at different pH, size-exclusion chromatography (SEC) using a pH gradient from 4.0-7.0 for OXA-48 and OXA-48 R206A, R189A, and R189A/R206A mutants were conducted. Through SEC it is possible to separate proteins based size. Larger molecules will move around the porous beads in the column material, and hence move through the column more quickly than smaller molecules which may enter through the pore of the beads [103]. In this manner, it should also be possible to separate monomer and dimer forms of the enzyme.

The method conditions were the same as when testing OXA-48 and OXA-48 R206A in a previous experiment, by Trine J. O. Carlsen and Bjarte A. Lund (unpublished data). From the results, it was clear that both OXA-48 and OXA-48 R206A eluted as monomers with phosphate-citrate buffer pH 4.0 with 50 mM K_2SO_4, and dimers at pH 5.0. It was therefore interesting to test the elution with phosphate-citrate buffer pH 4.5 for these enzymes.

The proteins were run through a Superdex 200 10/300 GL gel column with phosphate-citrate buffers supplemented with 50 mM K_2SO_4 at pH 4.0, 4.5, 5.0, 6.0, and 7.0, with a protein concentration of 10 μM. The proteins were injected into the column through a 200 μL loop. The ÄKTA explorer Fast Protein Liquid Chromatography (FPLC) system with the computer program Unicorn 5.0 (GE Healthcare) was used for the size-exclusion chromatography. Flow rate was set to 1 mL/min, and the pressure limit to 0.5 mPa. Before use, the column was equilibrated with phosphate-citrate buffer supplied with potassium sulphate, at the appropriate pH, for one-column volume. To correlate the molecular weight to the elution volume (cannot be correlated directly, as protein charge and shape differ in addition to their molecular weight), the standards Conalbumin (Mw: 75 kDa) and Carbonic anhydrase (Mw: 29 kDa) were used, as these are quite similar in size to the OXA-48 monomer (Mw: 28 kDa) and dimer (Mw: 56 kDa).

2.4   Enzyme kinetics

Table 2-9: Solutions used to investigate the enzyme kinetics activity of OXA-48 and a selection of OXA-48 mutants with nitrocefin, ampicillin, imipenem and ceftazidime.

Solution	Content
Buffer J	100 mM Na_2HPO_4/NaH_2PO_4 pH 7.0 50 mM $NaHCO_3$
Buffer K	100 mM Na_2HPO_4/NaH_2PO_4 pH 7.0 50 mM $NaHCO_3$ 0.2 mg/mL BSA

It was originally planned to test the enzyme activity of OXA-48 and all the OXA-48 mutants designed during this thesis with nitrocefin (reporter substrate), ampicillin (penicillin), imipenem (carbapenem), and ceftazidime (cephalosporin). Due to time-limitations it was decided to test OXA-48 and all the OXA-48 mutants with nitrocefin, OXA-48 and OXA-48 S70T, S70T/T71S, P68A, P68A/Y211S with ampicillin and imipenem, and only OXA-48 and OXA-48 P68A, P68A/Y211S with ceftazidime.

The enzyme assays were conducted according to the method description of the enzyme kinetic experiments for OXA-48 by Lund et al. [39]. The enzyme- and substrate concentrations used as a starting point for the assays were also based on the reported concentrations used in the previously mentioned article [39]. For the substrate concentration starting point for OXA-48 P68A and P68A/Y211S mutants MIC values from the studies by PhD. student Christopher Fröhlich, were compared to MIC values of OXA-48 and OXA-163 in a study by Poirel et al. [53] which also reported enzyme activity.

A small amount of ampicillin, imipenem and ceftazidime was dissolved in 1 mL Buffer J (Table 2-9) (nitrocefin was dissolved in DMSO). To determine the substrate concentration 10 μL of the dissolved substrate was added to 990 μL Buffer J in an UV-cuvette, and the initial OD was measured at the appropriate wavelength (individual for each substrate – see Table 2-10). 1 μL OXA-48 (~7 mg/mL) was then added (mixed well), and the absorbance was measured at regular intervals until substrate was hydrolysed. Using equation 2-2 the substrate concentration was calculated. For substrate concentration determination of ceftazidime 10 μL VIM-2 (~10 mg/mL) was used for the hydrolysis (due to OXA-48 being considered inactive against ceftazidime), the enzyme concentration was increased due to slow hydrolysis rate. The wavelengths and extinction coefficients for the substrates, are listed in Table 2-10.

$$(2\text{-}2) \qquad [Substrate] = \frac{(end\ OD - initial\ OD) \times dilution\ factor}{\Delta\ \varepsilon}$$

Table 2-10: Wavelengths, extinction coefficients, and plate specific extinction coefficients for the substrates nitrocefin, ampicillin, imipenem and ceftazidime.

Substrate	Wavelength (nm)	Extinction coefficient ($\Delta\varepsilon$)	Plate specific extinction coefficient ($\Delta\varepsilon$, OD/μM)
Nitrocefin (reporter substrate)	482	17400	0.004200
Ampicillin (penicillin)	235	-820	0.0004566
Imipenem (carbapenem)	300	-9000	0.002005
Ceftazidime (cephalosporin)	260	-9000	0.004843

The measurements were performed on a UV spectrophotometer SpectraMax M2[e] (Molecular Devices) with the program SoftMax Pro 5.2 software (Molecular Devices), using Corning 96-well UV-plates. Dilution series of 8 dilutions were prepared for each substrate, with three parallel runs. The assay was set up with 100 μL reaction volume; 40 μL Buffer J, 50 μL substrate - at appropriate concentration diluted in Buffer J, and 10 μL enzyme – at appropriate concentration diluted in Buffer K (Table 2-9). Bovine Serum Albumin (BSA) was added to kinetics Buffer K used to dilute the enzymes, to stabilizes the enzyme at such low concentrations, keeping it from denaturation [104]. The assay was run for 40 min, with reading intervals from 15-25 sec, at 25°C.

The software GraphPad Prism 7 was used to analyse the data. To create the Michaelis-Menten curves the substrate concentration (μM) is plotted against the initial velocity (μM/s). The initial velocity is measured in mOD/min by the spectrophotometer, and is converted to the appropriate unity by the plate specific extinction coefficient. The plate specific extinction coefficient for the given batch of plates was calculated for ampicillin, imipenem and ceftazidime by Dr. Susann Skagseth. Nitrocefin is not measured using UV-plates, and the plate specific extinction coefficient for the 96-well plates used for this experiment was determined.

3 Results and discussion

3.1 Mutagenesis, protein expression and protein purification

3.1.1 Site-directed mutagenesis of residues 68, 70, 71, 189, 206 and 211 in OXA-48

It was set out to investigate the effect of residues 68, 70, 71, 189, 206 and 211 in the active site and dimer interface, to study its effect on the enzyme activity and thermostability. To do this site-directed mutagenesis of OXA-48 was conducted.

Mutagenesis of the first OX-48 mutants; S70A, S70T, S70T/T71S, R189A was challenging, and several optimization methods were tested. After the first attempt, no colonies could be observed growing on the LB-agar plate after transformation. The prepared XL1-Blue cells were first suspected. A different in-house *E. coli* cloning strain DH5α was tested, as well as commercial competent XL1-Blue cells (Agilent), without results. A positive control using the supplied pWhitescript 4.5-kb control plasmid, and oligonucleotide control primers (fwd. and rev.) was also set up using the in-house competent XL1-Blue cells for transformation, and seemed to work fine.

Due to high melting-temperature of the primers (78-83°C, see Table 2-1) the annealing temperature was increased from 55°C to 60°C. The elongation time was increased as well, from 5 min (1 min/1kbp) to 5 min and 30 sec. This did not yield any results, therefore a DMSO gradient from 1-5% was tested. Again, no colonies were obtained.

The annealing temperature is known to affect the purity and yield of a PCR reaction. Increasing the annealing temperature may increase the specificity of the annealing reaction, reducing the amplification of non-specific DNA fragments, and increasing the formation of the correct/desired product [105]. Having a sufficiently long elongation step is also important for the yield of the PCR reaction, as the polymerase requires sufficient time to replicate the sequence of interest. The elongation time is dependent on the polymerase used, and should not be increased by too much compared to the manufacturers recommendations as a too long elongation time may result in higher error rates [106]. As it was suspected that the primers might be the problem, a DMSO gradient was also tested. DMSO has been found to increase the yield of the PCR reaction in GC-rich DNA templates and primers by preventing secondary structure formation [107]. Even though the primers had a recommended GC content of <60% this might have an effect.

The QuikChange II Site-Directed Mutagenesis Kit used for the mutagenesis of OXA-48 was from 2015, and it was decided to test a more recently purchased, available, polymerase; Phusion (BioLabs). The QuikChange II Site-Directed protocol was used with the Phusion polymerase. Even though none of the optimization test had yielded any positive results, it was decided to continue using the increased annealing temperature (60°C), and elongation time (5 min and 30 sec), as well as 1% DMSO. This gave a few colonies for the OXA-48 S70T and S70T/T71S mutants. The constructs were analysed using PCR amplification and gel electrophoresis, showing DNA bands at the appropriate size for OXA-48 S70T/T71S, but none for OXA-48 S70T. Plasmid purification and sequencing of the OXA-48 S70T/T71S construct was carried out, which confirmed the first correct mutation.

It was speculated if the DNA polymerase was the problem, therefore a new QuikChange II Site-Directed Mutagenesis Kit was purchased. An annealing temperature gradient from 55-75°C, and a concentration gradient using 5, 20 and 40 ng template, were set up for the mutant strand synthesis reaction, to identify optimum PCR conditions. Once again, no colonies after the transformation of the OXA-48 mutant construct was observed. The template gradient was investigated since the total amount of DNA in a PCR reaction has an effect on the outcome. Too much DNA may cause packed DNA in the confined reaction space and lead to poor DNA synthesis by the obstruction of the polymerase enzymes. The template:primer ratio should be optimized, as a too high primer ratio compared to template may cause primer self-annealing [106].

The positive control reaction was set up according to protocol, to eliminate any errors with the new kit, which also this time worked fine. It was decided to test the Phusion polymerase instead of *Pfu*Ultra polymerase again, but without results.

It was concluded that the problem most likely was the primers. But why only the OXA-48 S70T/T71S primer should work was not clear, as the primer length, GC contents, secondary structure and melting temperature were quite similar among the different primers. It was then finally discovered, when planning to test a primer concentration gradient, that the primer concentration had been miscalculated, and the primer concentration used had been too high. Then with the correct primer concentration the mutant strand synthesis reaction was finally conducted with success, as specified in the method description, for OXA-48 S70A, S70T, R189A, R189A/R206A and P68A (see section 2.1.1.3).

To create the double mutant OXA-48 R189A/R206A, the OXA-48 R206A gene construct was used as a template. For OXA-48 P68A/Y211S the OXA-48 P68A construct was the template to create the double mutant, but without success. A OXA-48 Y211S mutant was therefore prepared, by applying this template instead, and the P68A primers the second double mutant was made. For the mutant strand synthesis reaction, the temperature was lowered to 55°C (as originally suggested by the protocol), and the elongation time increased to 6 min. In addition, the transformed construct was spread on LB-agar plates with reduced ampicillin concentration. This gave a positive result.

The successful transformation of the OXA-48 mutant constructs were confirmed by PCR amplification and gel electrophoresis analysis. The size of the gene constructs after amplification PCR, using the T7 fwd. and rev primers to transcribe the region between the T7 promotor and terminator region of the pDEST17 vector (see Figure 2-2) is 958 bp. The OXA-48 mutants showed DNA bands around 1000 bp from the gel electrophoresis, as shown in Figure 3-1. The OXA-48 mutant constructs were purified using the Wizard Plus SV Minipreps DNA Purification System Kit. The final DNA concentrations for the purified plasmids are given in Table 3-1. Finally, the correct mutations (nucleotide substitutions) were confirmed by Sanger sequencing (at the Sequencing Lab at the University Hospital of Northern Norway), and identified by sequence alignment in BioEdit. Generally, 3 bacterial colonies for each mutant were selected for cultivation, plasmid purification and sent to sequence analysis, as about half of the sequence analyzed constructs contained the desired mutation(s).

Table 3-1: DNA concentration of the purified OXA-48 mutant constructs after mutagenesis. The DNA concentration was measured from the OD_{280} absorption on the NanoDrop instrument.

OXA-48 mutant	DNA concentration (ng/μL)
S70A	57.9
S70T	54.8
S70T/T71S	38.6
R189A	63.5
R189A/R206A	48.9
P68A	47.9
P68A/Y211S	48.8

Figure 3-1: Agarose-gel image of a selection of positive OXA-48 mutants after PCR screening (STTS is short for the mutant OXA-48 S70T/T71S). Perfect DNA 0.1-12 kbp marker was used, and relevant ladder-bands are indicated with size in kilo base pairs (kbp). As can be seen from the image the positive OXA-48 mutants showed bands around 1000 bp after amplification using T7 primers. Positive control with pDEST17 OXA-48 construct (also amplified using T7 primers) showed the same size, as expected. Negative control showed no bands, as it consisted only of reaction mix (no construct).

3.1.2 Protein expression of OXA-163, OXA-48, and OXA-48 mutants; R189A, R189A/R206A, P68A, P68A/Y211S, S70T, S70T/T71S, and S70A

Glycerol stocks of OXA-163 (BL21(DE3)pRARE) and OXA-48 (BL21(DE3)pLysS) was provided for cultivation and expression of the enzymes. OXA-163 grew faster than OXA-48, and was therefore allowed to reach a higher cell density (measured OD_{600}) before induction. The cells were induced at 20°C with 0.4 mM IPTG o/n. Both OXA-48 and OXA-163 seemed to be expressed well after induction. For the OXA-48 samples less of other cell components seemed to be expressed with the protein, compared to OXA-163. Probably explained by the lower cell density upon induction, visible by the difference between the BFI samples of OXA-48 and OXA-163. The SDS-PAGE gel image from the large scale expression of OXA-48 and OXA-163 is shown in Figure 3-2.

The selection of different *E. coli* expression strains and expression conditions for the OXA-48 mutants in this thesis was based on previous positive results from expression and purification of OXA-48 [39], OXA-181 and other OXA-48 mutants [95]. Small scale optimization would probably have identified more ideal conditions, and given a higher protein yield. Finding the optimal expression conditions was not the goal here however, and identifying the conditions that yielded enough protein for the following experiments was sufficient.

Two strains were used for large scale expression; (1 L) *E. coli* BL121Star(DE3)pRARE and Rosetta2(DE3)pLysS. The first OXA-48 mutants obtained were S70A, S70T, S70T/T71S and R189A, and these were also expressed first. For these mutants, no AFI and BFI samples could be analysed by SDS-PAGE due to sticky samples. It was therefore not possible to determine which strain that gave the best protein expression, or how the expression was affected by the reduced induction temperature and IPTG concentration compared to OXA-48. It was decided to use the cell culture from the previously successful strain BL121Star(DE3)pRARE

60

[39] for protein purification. From the large scale expression of OXA-48 P68A, P68A/Y211S, and R189AA/R206A it was possible to load the AFI and BFI sample to the SDS-PAGE gel, and the expression could be evaluated. From the gel analysis it was concluded that the protein expression was slightly better in Rosetta2(DE3)pLysS cells, than in BL21Star(DE3)pRARE cells. Still, the cell culture from the BL21Star(DE3)pRARE strain were used for protein purified. The SDS-PAGE gel image from the large scale expression of OXA-48 P68A, P68A/Y211S and R189A/R206A is shown in Figure 3-3.
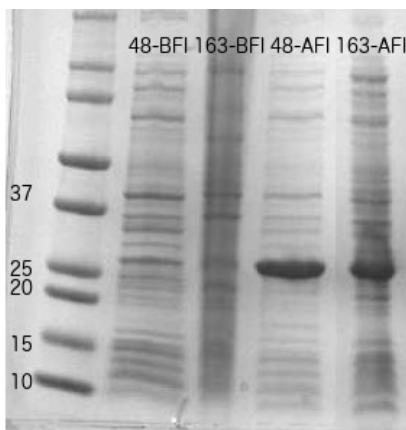

Figure 3-2: SDS-PAGE gel image showing before induction (BFI) and after induction (AFI) samples, from expression of OXA-48 and OXA-163. Precision Plus 10-250 kDa ladder was used, the marks of interest are labelled in kDa. The expressed protein is approximately 30 kDa, and can be seen as a clear band in the AFI samples of both enzymes slightly above the 25 kDa mark.

Figure 3-3: SDS-PAGE gel image showing before induction (BFI) samples **(A)**, and after induction (AFI) samples **(B)**, from expression of OXA-48 P68A (PA), P68A/Y211S (PAYS), and R189A/R206A (RARA) in both Rosetta2(DE3)pLysS and BL21Star(DE3)pRARE cell strains. Precision Plus 10-250 kDa ladder was used, the markers of interest are labelled in kDa. The expressed protein is approximately 30 kDa, and can be seen as a clear band in the AFI samples (B), slightly above the 25 kDa mark.
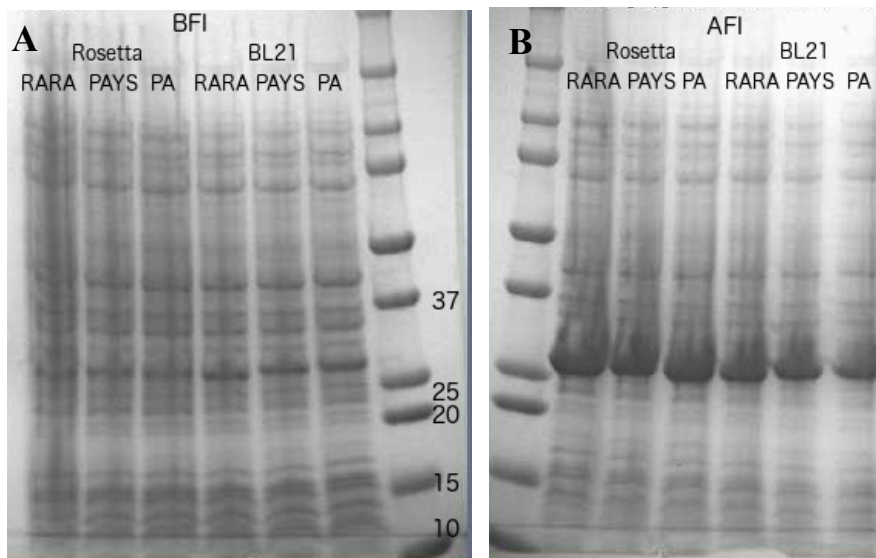
3.1.3 Using immobilized metal ion affinity chromatography for protein purification

To be able to test the enzyme activity, enzyme stability and conduct successful crystallization experiments the purity of the enzyme is crucial, aiming for samples without other cell contaminants and proteins affecting the measurements. OXA-48, OXA-163 and the OXA-48 mutants were all designed with a hexa histidine-tag and a TEV protease cleavage site upstream to the genes. The hexa His-tag is for purification with a HisTrap nickel column followed by a TEV protease to cleave the His-tag and most of the TEV binding site.

TEV protease had to be produced, to cleave the His-tag from the proteins of interest. The TEV protease also carries a His-tag, making it feasible to separate non-cleaved protein and His-TEV protease that will both bind to the nickel column, from the successfully cleaved protein eluting in the flow through, in the second His-tag purification step. Expression and purification of TEV yielded quite a lot of protein.

For the OXA enzymes the highest yield of pure protein was obtained for OXA-163. For OXA-48 and the OXA-48 mutants the total protein yields were significantly lower. This is likely related to OXA-163 being a synthetic DNA gene optimized for *E. coli* expression, while OXA-48 were cloned from a *K. pneumoniae* sample. Still sufficient amounts of OXA-48 and OXA-48 mutants were obtained. The final obtained protein yields are listed in Table 3-2.

Table 3-2: Final obtained protein yield after protein purification, from expression in 1 liter (L) culture.

Enzyme	Protein yield (mg) per litre culture
TEV protease	77.1
OXA-163	98.7
OXA-48	23.9
OXA-48 S70A	15.1
OXA-48 S70T	42.2
OXA-48 S70T/T71S	23.8
OXA-48 R189A	24.5
OXA-48 R189A/R206A	23.7
OXA-48 P68A	9.9
OXA-48 P68A/Y211S	16.7

3.1.3.1 Protein purification of TEV protease

It was clear from the first purification step that there was quite a lot of TEV present in the protein sample, evidenced by a large protein peak measured absorption at OD_{280}, eluting during the imidazole gradient in the chromatogram (Figure 3-4). Samples from the protein peak fractions (35-41) were collected for SDS-PAGE analysis, as well as one sample from the flow-through. The His-tagged TEV protease is around 29 kDa. From the SDS-PAGE gel analysis it was clear that a lot of TEV protease was present, visible as "smeared" bands above the 25 kDa ladder mark. Some contaminants (binding to the HisTrap column) were still in the sample, and the TEV protease sample was estimated to be >90% pure (Figure 3-5).

Since TEV protease and other contaminants binding to the HisTrap column will be removed from the protein of interest in the second purification step, it was decided that TEV was pure enough for its purposes. It was also desirable to conduct the purification of TEV quickly, to obtain as much protein as possible. The total amount of obtained protein is listed in Table 3-2.
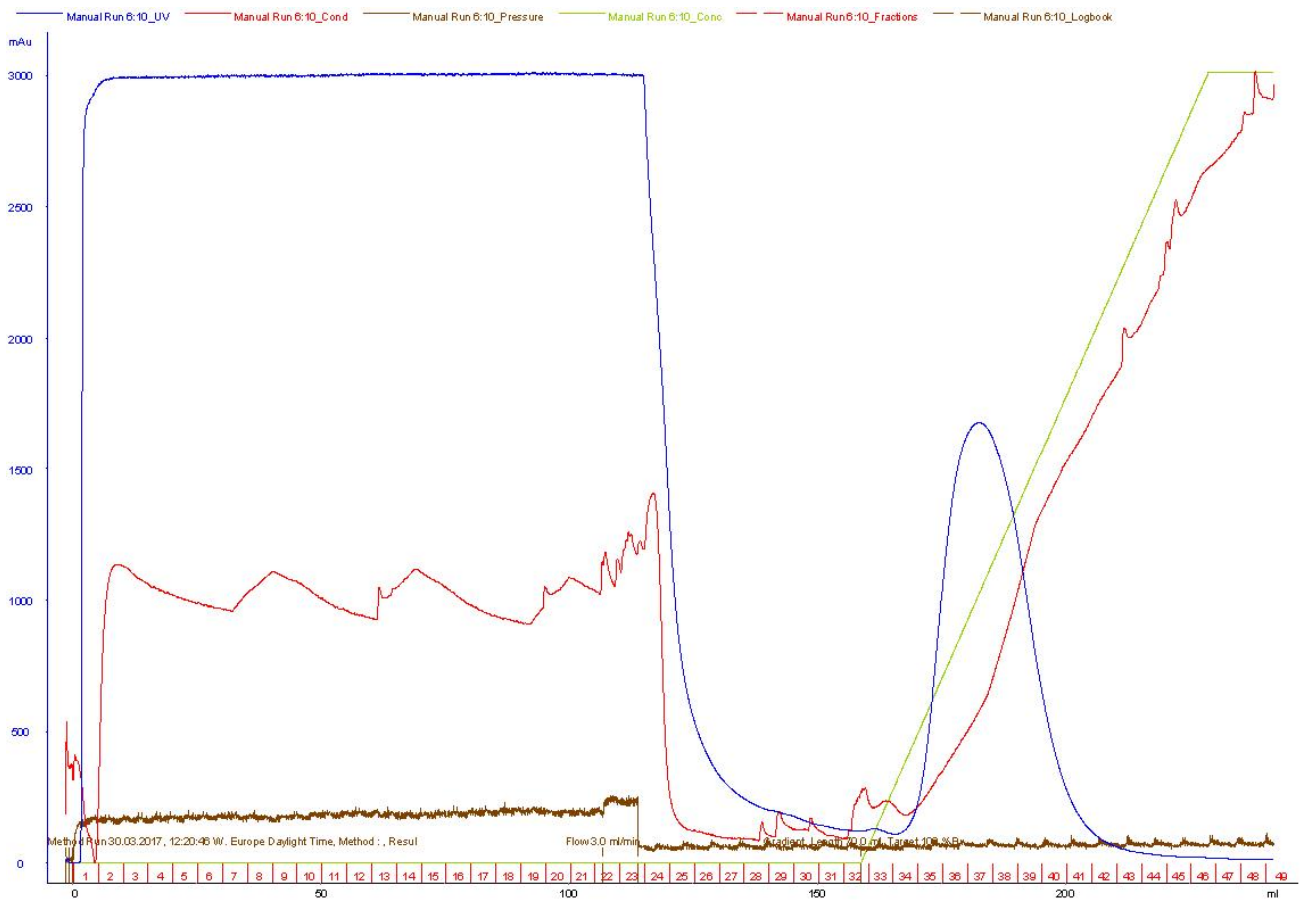
Figure 3-4: Chromatogram from ion metal affinity chromatography purification of TEVsh using a 5 mL HisTrap FF crude column. The blue line is the measured absorbance at 280 nm, show the large flow-through, and the eluted protein peak, thus proteins with affinity for the nickel column. The green line shows the concentration of Buffer B with 500 mM imidazole and the gradient. The other lines show the pressure (brown) and conductivity (red). The fraction number is shown in red along the x-axis, while the absorbance (OD_{280}) is shown in blue along the y-axis.
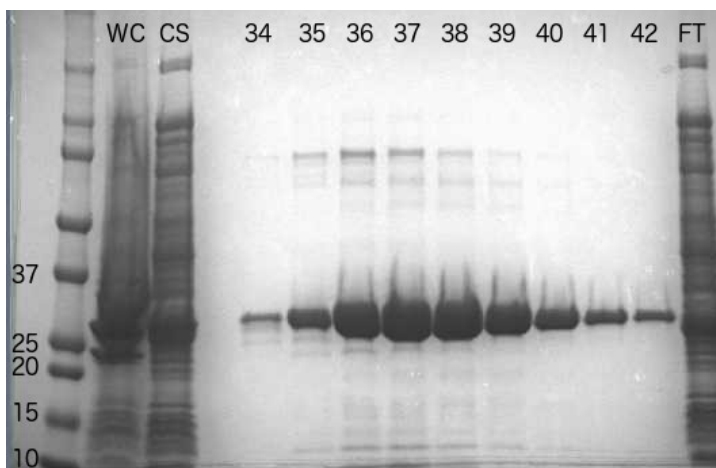
Figure 3-5: SDS-PAGE gel image from the purification of TEV protease. The ladder Precision Plus 10-250 kDa was used (left), and marks of relevance are labelled in kDa. The whole cell (WC) sample (after sonication of the cells) is shown in lane 1, cell supernatant (CS) sample (before purification) is shown in lane 2. One sample from the flow-through is shown in the last lane. Samples from the protein peak, are labelled according to the fractions from the purification shown in Figure 3-4.

3.1.3.2 Protein purification of OXA-163

The chromatogram of OXA-163 showed a quite large protein peak measured absorbance at OD_{280}. The chromatogram is shown in Figure 3-6. Samples from the fractions of the contaminant peak (eluting at 5% Buffer E – Table 2-4, 25 mM imidazole), and from the protein peak (eluting during the imidazole gradient), as well as one sample from the flow-through, were collected for SDS-PAGE gel analysis. The uncleaved, His-tagged, expressed OXA-163 construct (and OXA-48) is 29.8 kDa, while the protein without the His-tag is 28.2 kDa. The SDS-PAGE gel image (Figure 3-9) shows protein bands at the appropriate size for BTEV and ATEV samples. The band of the BTEV sample appears slightly higher up on the gel, while the ATEV sample is visible as two separate bands, most likely being the TEV protease and the cleaved protein slightly further down on the gel. A weak band at the bottom of the gel is also visible for the ATEV sample, this is most likely the cleaved His-tag.

The SDS-PAGE gel analysis showed a high yield of protein in the sample, visible as smeared bands slightly above the 25 kDa ladder mark. Some protein seemed to be present in the contaminant peak (Figure 3-7 A), indicating that the HisTrap column might be overloaded, causing some of the protein to elute at low imidazole concentrations. When analysing the SDS-PAGE gel image from the protein peak fractions (Figure 3-7 B) fraction 20-28 were selected for TEV-cleavage during dialysis.

From the second HisTrap purification step the chromatogram showed a large flow-through, containing the cleaved OXA-163, and two contaminant peaks eluting during the imidazole gradient (Figure 3-8). The first and sharpest of the contaminant peaks is most likely TEV protease due to its high concentration. From the SDS-PAGE gel analysis there seemed to be some uncleaved protein eluting with the contaminants. However, it is difficult to differentiate between the TEV protease and the OXA-48 like enzymes on a SDS-PAGE gel, as they are approximately the same size. The SDS-PAGE gel from the second HisTrap purification step indicate that the OXA-163 sample is >95% pure (Figure 3-9), fraction 4-12 were collected.

OXA-163 was concentrated by centrifugation using Amicon Ultra centrifugal filter (10 kDa MWCO), to 9.4 mg/mL. The total amount of OXA-163 that was obtained after protein purification from 1 L cell culture is listed in Table 3-2.

Figure 3-6: Chromatogram from the first HisTrap purification step of OXA-163 using a 5 mL HisTrap HP column The blue line is the measured absorbance at 280 nm, show the large flow-through, and the eluted protein peak, thus proteins with affinity for the nickel column. The green line shows the concentration of Buffer E with 500 mM imidazole and the gradient. The other lines show the pressure (brown) and conductivity (re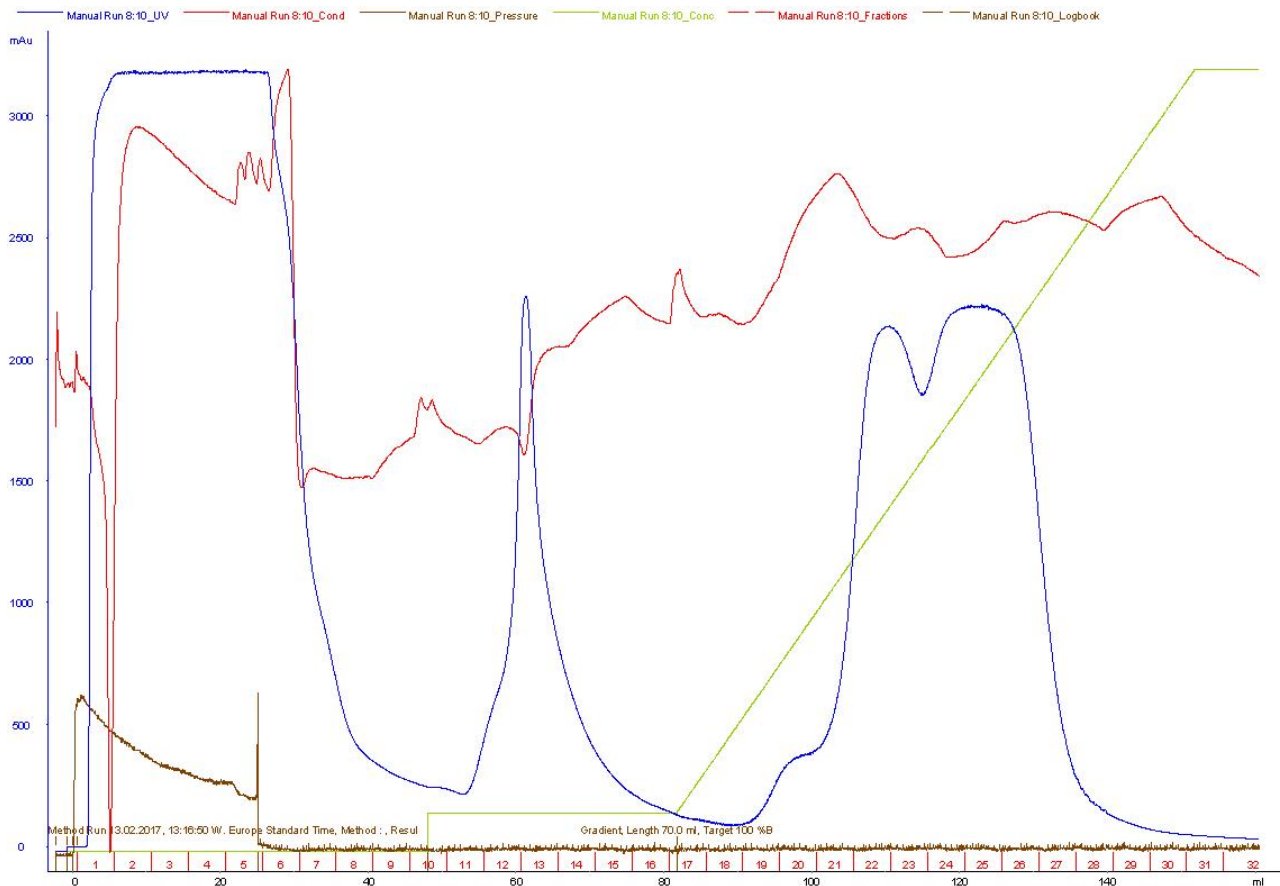d). The fraction number is shown in red along the x-axis, while the absorbance (OD_{280}) is shown in blue along the y-axis.

Figure 3-7: SDS-PAGE gel image from the first purification step of OXA-163. The ladder Precision Plus 10-250 kDa was used, and marks of relevance are labelled in kDa. **A)** The whole cell (WC) sample (after sonication of the cells) are shown in lane 1, cell supernatant (CS) sample (before purification) is shown in lane 2, and the flow-through (FT) in lane 3. Samples are labelled according to the fractions from which they were collected (see Figure 3-6). **B)** Shows the samples collected from the protein peak fractions.

66

Figure 3-8: Chromatogram from the second HisTrap purification step of OXA-163 using a 5 mL HisTrap HP column. The blue line is the measured absorbance at OD_{280}, showing the protein flow-through first, and two contaminant peaks at increasing imidazole concentrations, the first one of those most likely being TEV protease. The green line shows the concentration of Buffer E with 500 mM imidazole and the gradient gradient. The other lines show the pressure (brown) and conductivity (red). The fraction number is shown in red along the x-axis, while the absorbance (OD_{280}) is shown in blue along the y-axis.
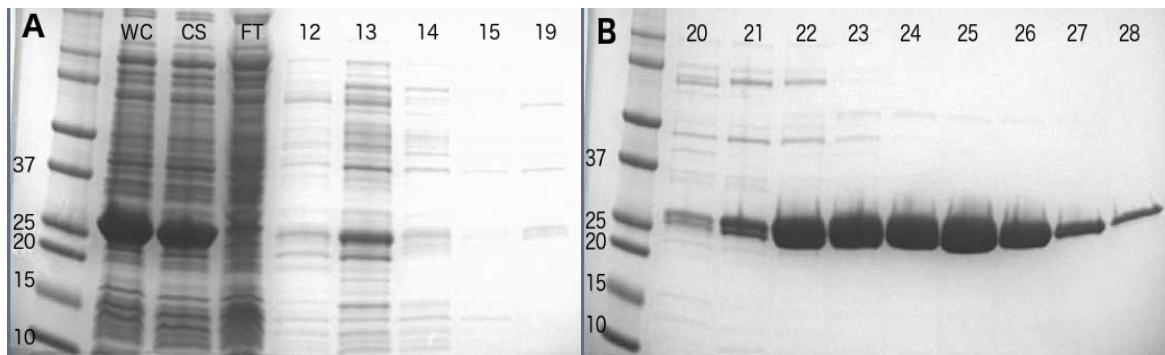

Figure 3-9: SDS-PAGE gel image from the second purification step of OXA-163. The ladder Precision Plus 10-250 kDa was used, and marks of relevance are labelled in kDa. Selected samples from the protein flow-through (4-13), are labelled according to the fractions from which they were collected (see Figure 3-8). Samples from fraction 17 and 20 are collected from the contaminant peaks (at increased imidazole concentration). Before TEV (BTEV) and after TEV (ATEV) samples show the cleavage of the His-tag from the protein.

67

3.1.3.3 Protein purification of OXA-48

Cells from 1 L cell culture was used to purify OXA-48, the observed protein peak in the chromatogram from the first HisTrap column the protein concentration seems to be quite high (Figure 3-10). This was confirmed on the SDS-PAGE gel (Figure 3-11), where the protein was quite pure already after the first purification step. Fraction 21-26 were collected for TEV-cleavage by dialysis. The chromatogram of the second HisTrap purification step (Figure 3-12) had a smaller flow-through than OXA-163, but the protein yield was still sufficient. A sharp TEV protease peak was visible at the beginning of the imidazole gradient, and one small contaminant peak containing other proteins with a high affinity to the HisTrap column. From the SDS-PAGE gel analysis (Figure 3-13) it seemed that the contaminant peaks this time as well contained mostly uncleaved OXA-48, thus confirming the separation of cleaved and non-cleaved OXA-48. BTEV sample was not collected, but the ATEV sample was analysed by SDS-PAGE (Figure 3-13).

Fraction 5-10 were collected after the purification. It was clear that the protein sample was >95% pure. OXA-48 was concentrated by centrifugation using the Amicon Ultra centrifugal filter (10 kDa MWCO) to 7.8 mg/mL. The total amount of OXA-48 that was obtained after protein purification from 1 L cell culture is listed in Table 3-2.
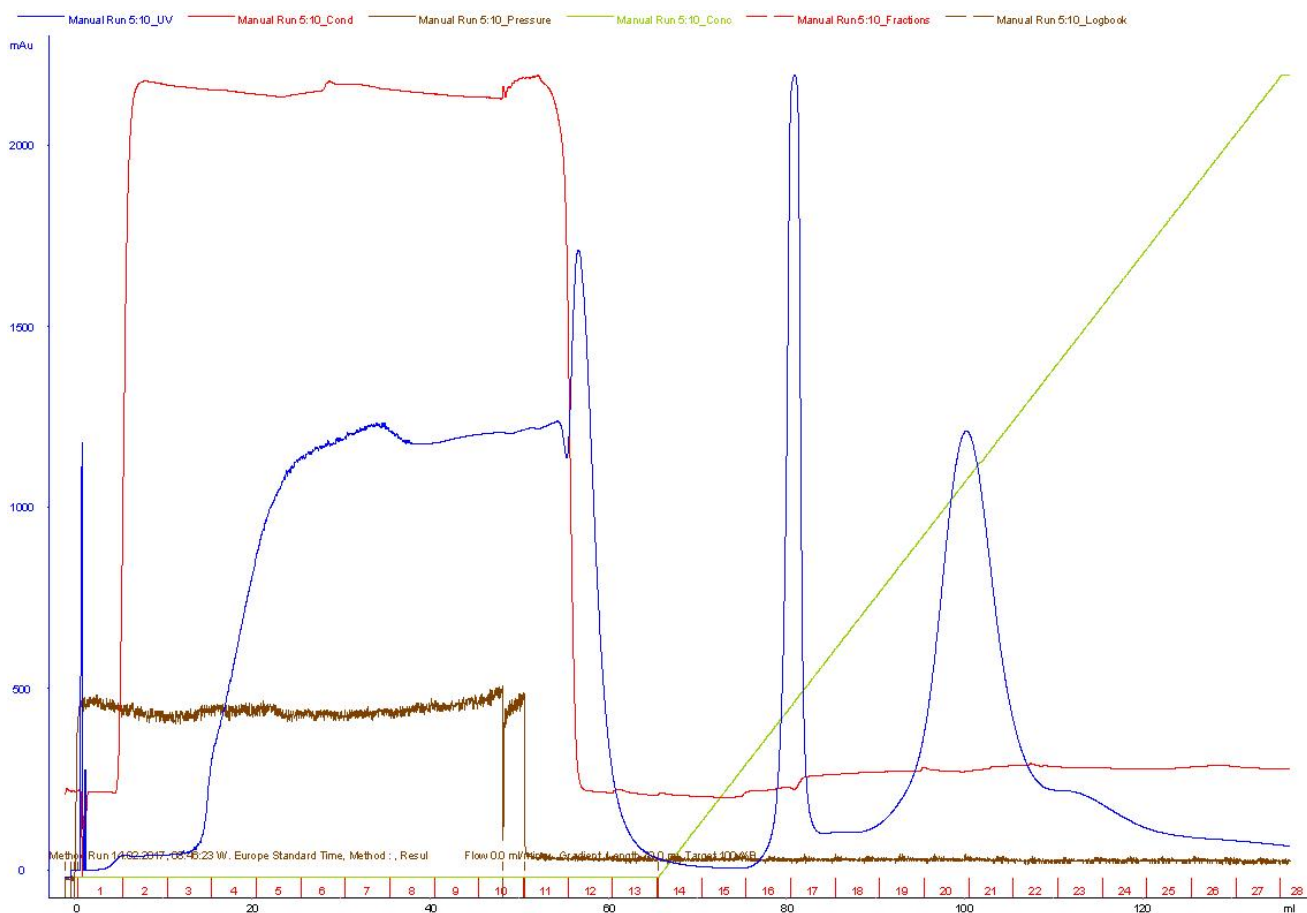
Figure 3-10: Chromatogram from the first HisTrap purification step of OXA-48 using a 5 mL HisTrap HP column. The blue line is the measured absorbance at 280 nm, showing the large flow-through, and the eluted protein peak, thus proteins with affinity for the nickel column. The green line shows the concentration of Buffer E with 500 mM imidazole and the gradient. The other lines show the pressure (brown) and conductivity (red). The fraction number is shown in red along the x-axis, while the absorbance (OD_{280}) is shown in blue along the y-axis.

Figure 3-11: SDS-PAGE gel image from the first purification step of OXA-48. The ladder Precision Plus 10-250 kDa was used, and marks of relevance are labelled in kDa. The cell supernatant (CS) sample (before purification) is shown in lane 1, and the flow-through (FT) in lane 2. Samples from the contaminant peak (12-14) and protein peak (19-26), are labelled according to the fractions from which they were collected (see Figure 3-10).
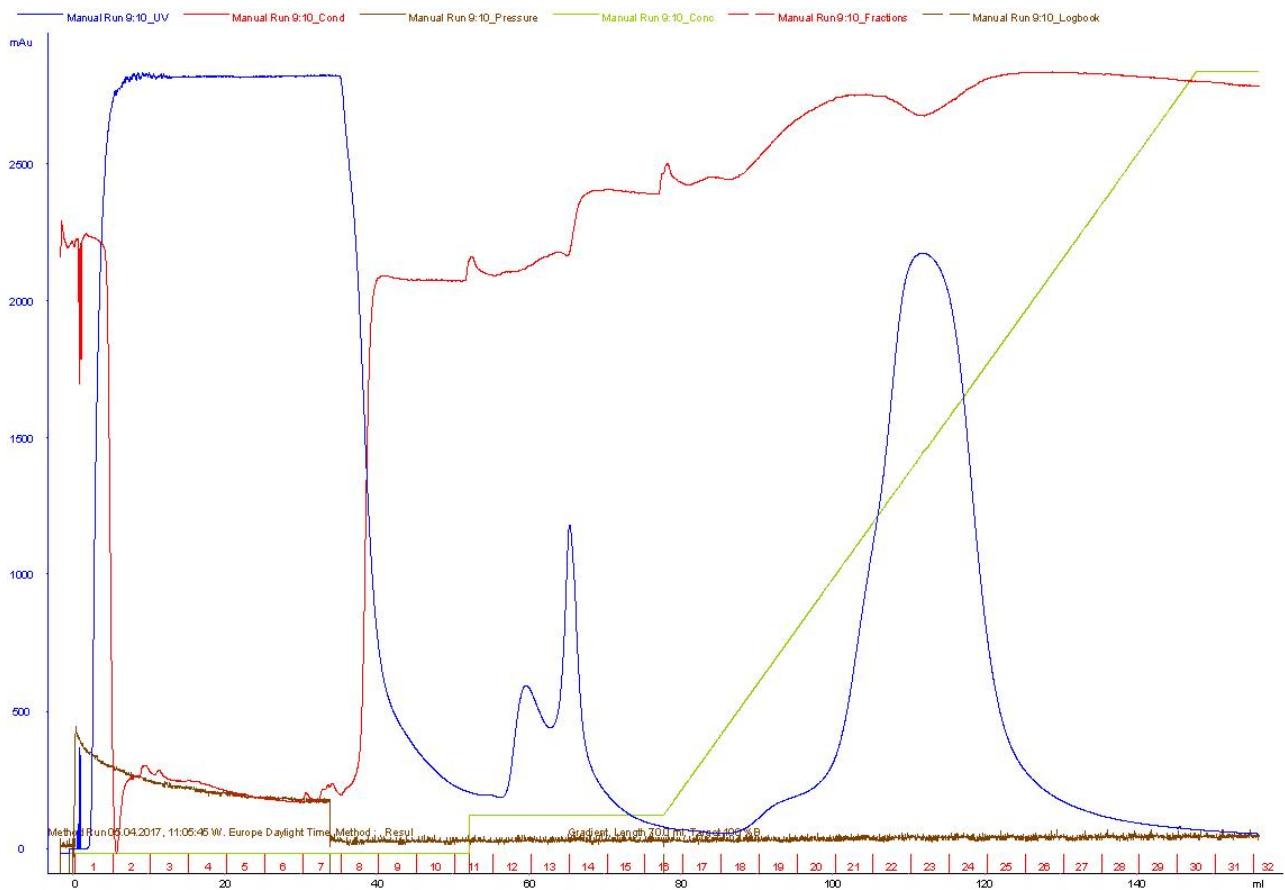
69
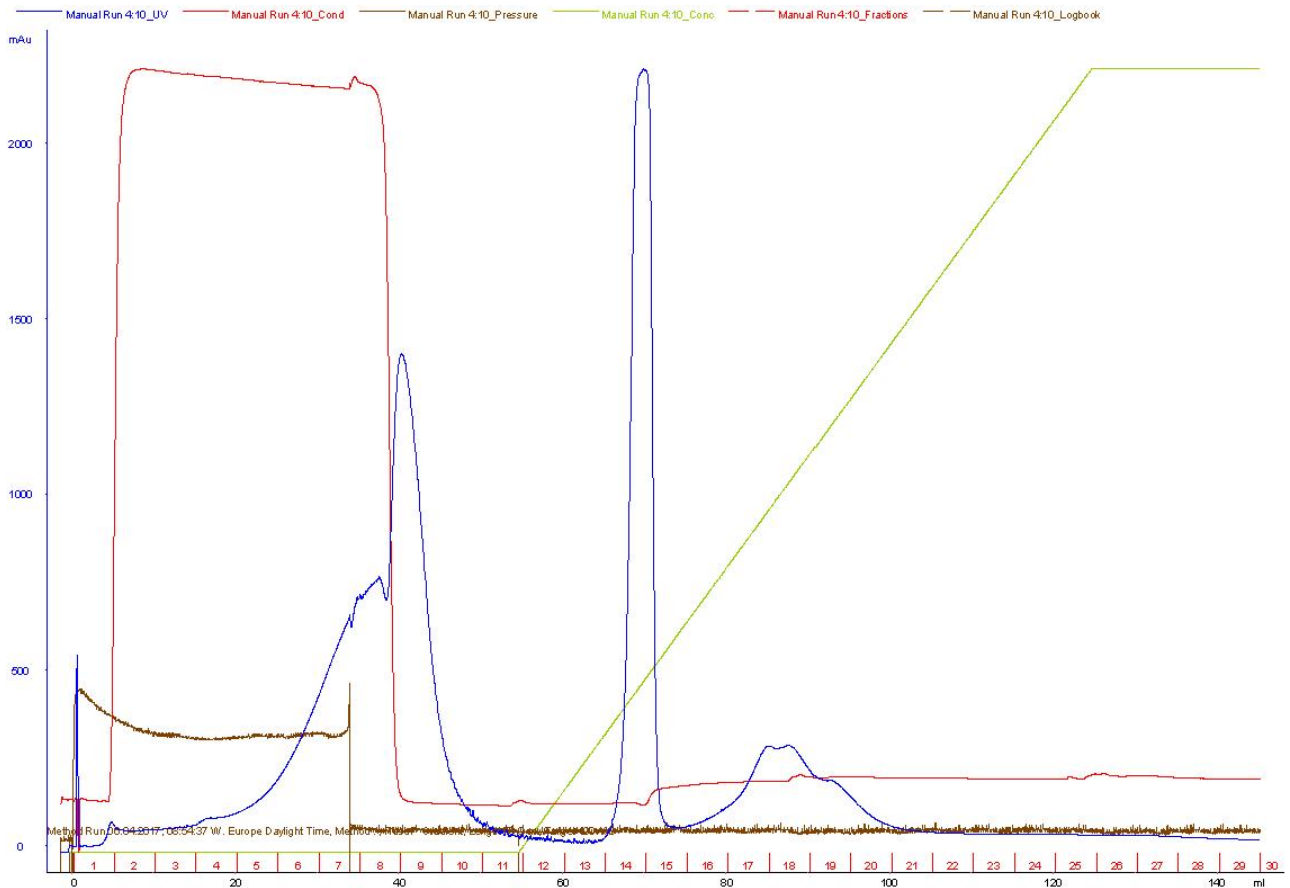
Figure 3-12: Chromatogram from the second HisTrap purification step of OXA-48 using a 5 mL HisTrap HP column. The blue line is the measured absorbance at OD_{280}, showing the protein flow-through first, and two contaminant peaks at increasing imidazole concentrations, the first one of those most likely being TEV protease. The green line shows the concentration of Buffer E with 500 mM imidazole and the gradient gradient. The other lines show the pressure (brown) and conductivity (red). The fraction number is shown in red along the x-axis, while the absorbance (OD_{280}) is shown in blue along the y-axis.
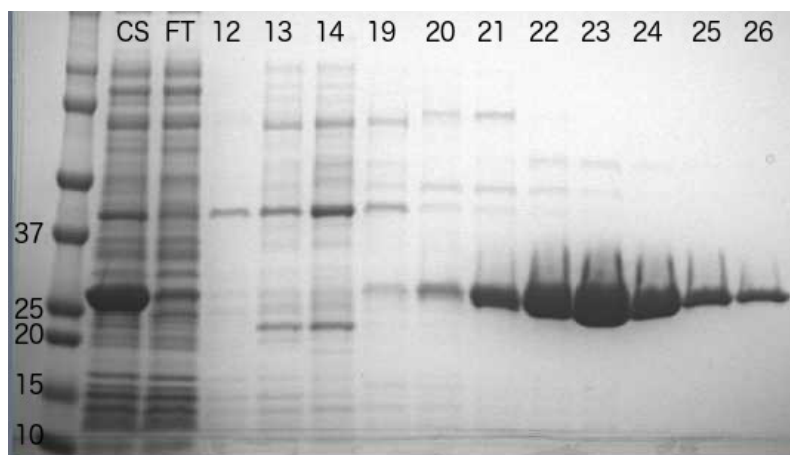

Figure 3-13: SDS-PAGE gel image from the second purification step of OXA-48. The ladder Precision Plus 10-250 kDa was used, and marks of relevance are labelled in kDa. Samples from the protein flow-through (4-10), are labelled according to the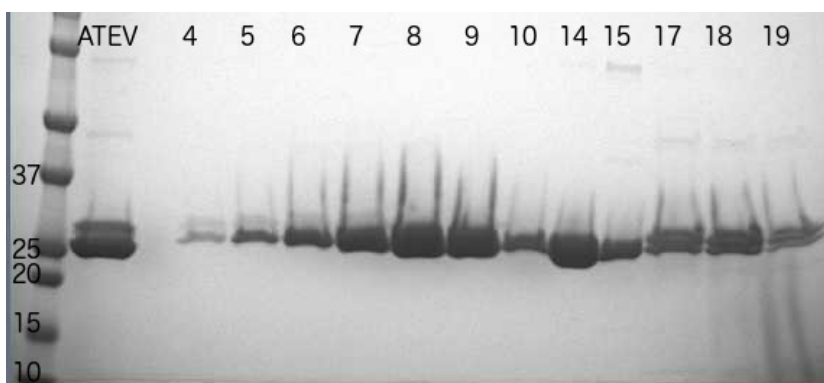 fractions from which they were collected (see figure 3-12). Samples from fraction 14, 15 and 17-19 are collected from the imidazole gradient. After TEV (ATEV) sample is shown in lane 1.

70

All the mutants were expressed in both BL21Star(DE3)pRARE and Rosetta2(DE3)pLysS, the BL21Star(DE3)pRARE cells were used for protein purification for most of the mutants. OXA-48 S70A showed a lower concentration of protein after the purification from Rosetta2(DE3)pLysS cells (15.1 mg) compared to BL21Star(DE3)pRARE cells (~30 mg), while OXA-48 R189A displayed the opposite effect (Rosetta2(DE3)pLysS cells 24.5 mg, BL21Star(DE3)pRARE cells ~10 mg).

The chromatogram from purification of OXA-48 P68A/Y211S are showed in Figure 3-14 and Figure 3-15, as an example of the chromatograms from the first and second purification steps of the different OXA-48 mutants, as the chromatograms displayed the same trends, with varying peak intensity (OD_{280}), also reflected in the final protein concentrations. The protein peak absorbance (OD_{280}) from the first HisTrap purification step (Figure 3-14) varied from 500-1500 mAu. The late protein flow-through elution in the second HisTrap purification step, displayed in Figure 3-15 for OXA-48 P68A/Y211S, was similar for most mutants, and OXA-48 (Figure 3-12). This may indicate a weak affinity for the nickel column even after cleavage of the His-tag, and the protein should perhaps have been loaded onto the column with a low concentration (eg. 20 mM) of imidazole. The sharp peak with absorbance (OD_{280}) around 1000 mAu, eluting first of the two contaminant peaks, was observed in all the chromatograms from the second HisTrap purification step, and is most likely TEV protease.
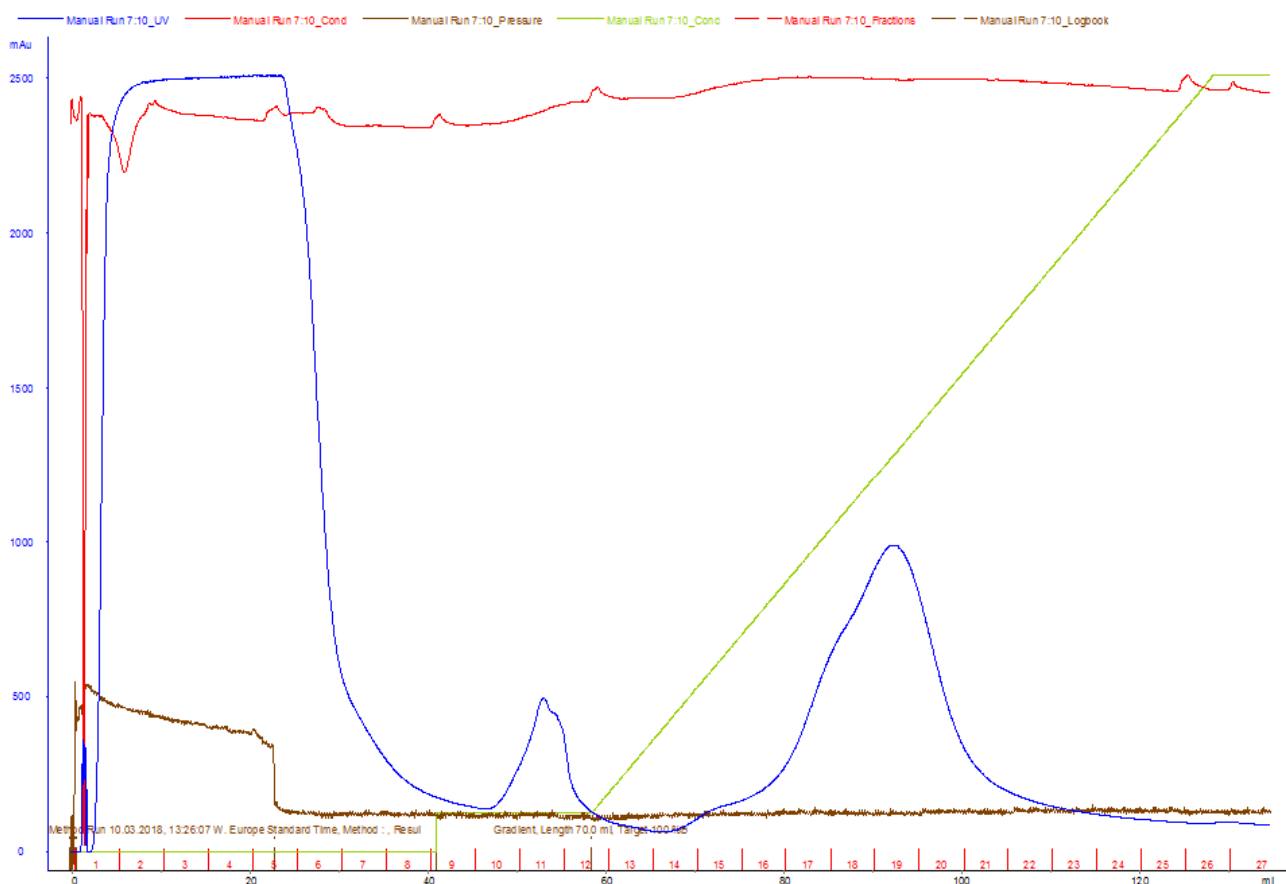
Figure 3-14: Chromatogram from the first HisTrap purification step of OXA-48 P68A/Y211S, shown as an example from the purification of the OXA-48 mutants. A 5 mL HisTrap HP column was used for the purification. The blue line is the measured absorbance at 280 nm, showing the large flow-through, and the eluted protein peak, thus proteins with affinity for the nickel column. The green line shows the concentration of Buffer E with 500 mM imidazole and the gradient. The other lines show the pressure (brown) and conductivity (red). The fraction number is shown in red along the x-axis, while the absorbance (OD_{280}) is shown in blue along the y-axis.
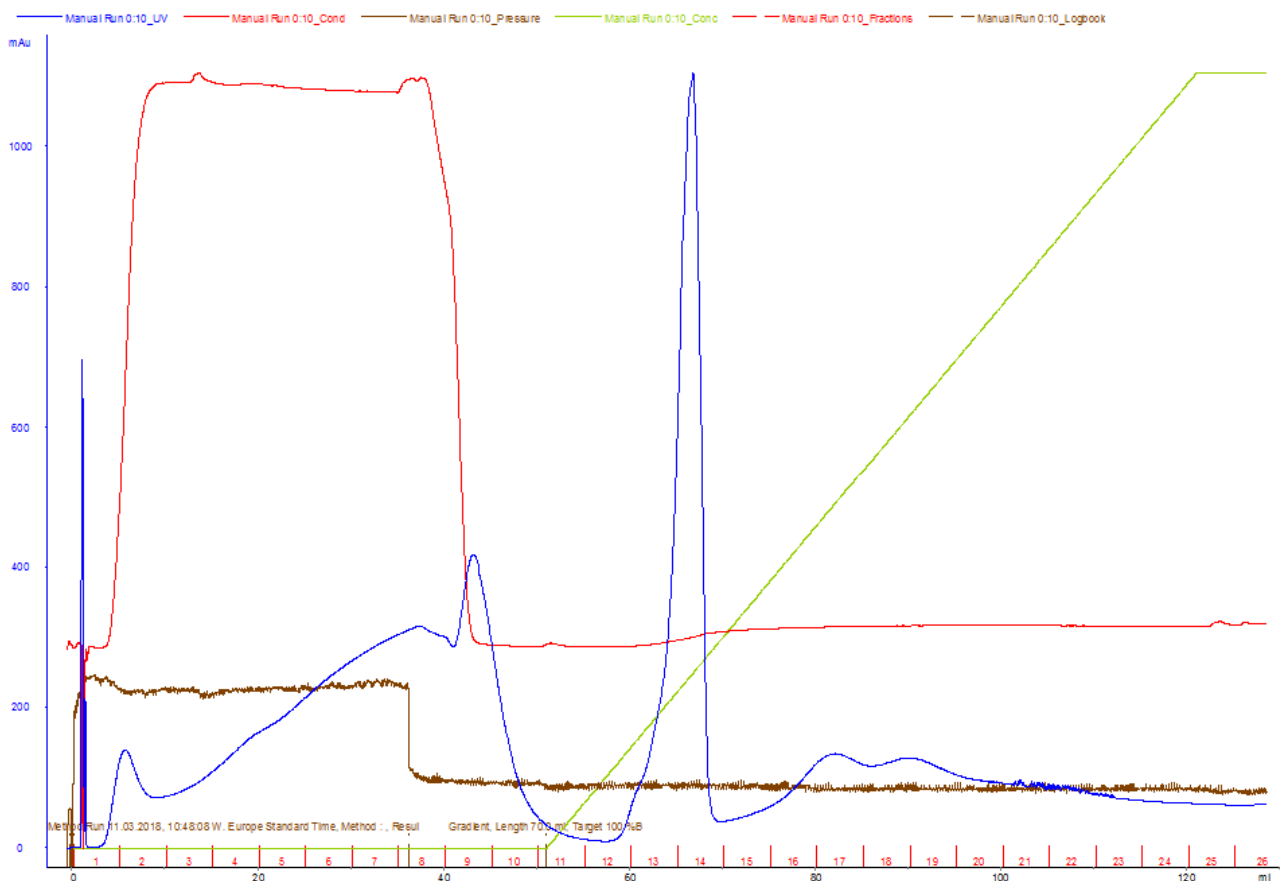
Figure 3-15: Chromatogram from the second HisTrap purification step of OXA-48 P68A/Y211S, shown as an example from the purification of the OXA-48 mutants. A 5 mL HisTrap HP column was used for the purification. The blue line OD_{280}, show the protein flow-through first, and two contaminant peaks at increasing imidazole concentrations. The green line shows the concentration of Buffer E with 500 mM imidazole and the gradient. The other lines show the pressure (brown) and conductivity (red). The fraction number is shown in red along the x-axis, while the absorbance (OD_{280}) is shown in blue along the y-axis.

Concerning the purification of the OXA-48 S70T/T71S mutant, samples from fractions selected from chromatogram protein peak absorbance at OD_{280} were collected for SDS-PAGE gel analysis for the first and second HisTrap purification for estimation of the sample purity, as previously described for OXA-48 and OXA-163. The SDS-PAGE gel images from both the HisTrap purification steps of OXA-48 S70T/T71S are shown in Figure 3-16. The wrong light source was used when imaging the gels, thus explaining the black background.

The protein was quite pure already after the first purification step, and fraction 12-17 were collected for dialysis and TEV cleavage. After the second HisTrap purification the protein was clearly >95% pure, and fraction 3-7 were collected for concentration. OXA-48 S70T/T71S was concentrated to 11.7 mg/mL. The total amount of obtained OXA-48 S70T/T71S after protein purification from 1 L cell culture is listed in Table 3-2.
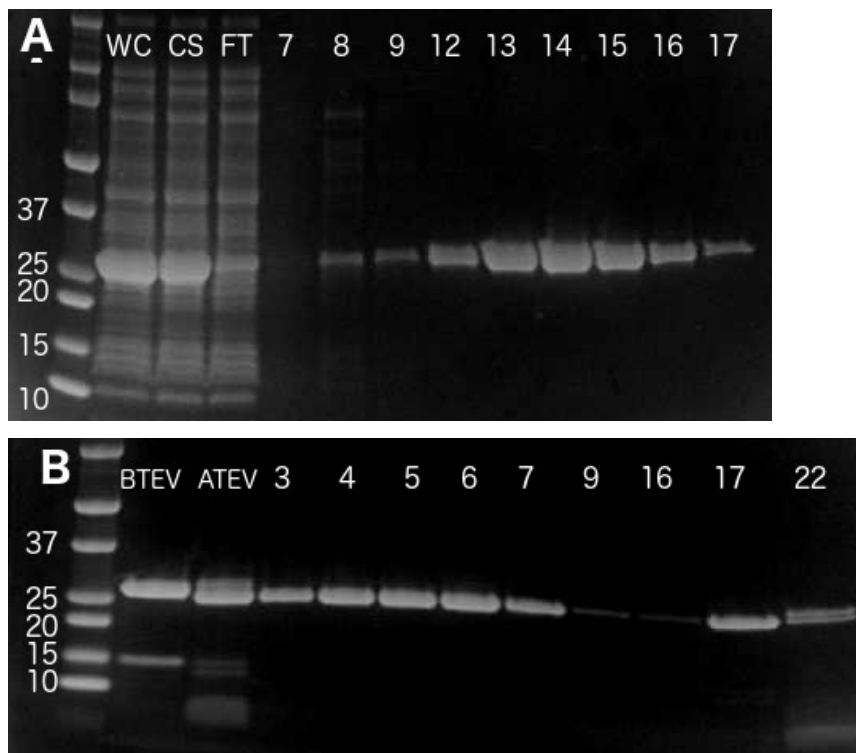
Figure 3-16: SDS-PAGE gel images from the purification of OXA-48 S70T/T71S, where incorrect light setting was used thus explaining the black background. The ladder Precision Plus 10-250 kDa (left) show relevant molecular weight standards in kDa. **A)** SDS-PAGE gel image from the first HisTrap purification step. The whole cell (WC) sample and cell supernatant (CS) sample are shown to indicate the protein solubility. The flow-through (FT) sample is shown as a control to check that no protein is eluted there, as would indicate an error. Samples from the contaminant peak (7-9) and protein peak (12-17), are labelled according to the fractions from which they were collected. **B)** SDS-PAGE gel image from the second HisTrap purification step. Samples from the protein flow-through (3-9), are labelled according to the fractions from which they were collected. Samples from fraction 16, 17 and 22 were collected from the contaminant peaks (at increased imidazole concentration). Before TEV (BTEV) and after TEV (ATEV) samples are shown.

OXA-48 S70T were purified in the same manner as previously described. SDS-PAGE gel image from the first HisTrap purification is shown in Figure 3-17 A, where fractions 22-26 were collected for TEV cleavage by dialysis. From the second HisTrap purification step the flow-through peak (OD_{280}) was quite broad, and fraction 6-19 were collected for SDS-PAGE gel analysis (Figure 3-17 B). Fraction 6-11 were pooled and concentrated by centrifugation using the Centriprep centrifugal filters (10 kDa MWCO) to 12.8 mg/mL. It was clear from the gel image that OXA-48 S70T was >95% pure. The total amount of OXA-48 S70T that was obtained after protein purification from 1 L cell culture is listed in Table 3-2.

Figure 3-17: SDS-PAGE gel images from the purification of OXA-48 S70T. The ladder Precision Plus 10-250 kDa (left) show relevant molecular weight standards in kDa. **A)** SDS-PAGE gel image from the first HisTrap purification step. The whole cell (WC) sample and cell supernatant (CS) sample are shown to indicate the protein solubility. The flow-through (FT) sample is shown as a control to check that no protein is eluted there, as would indicate an error. Sample(s) from the contaminant peak (14) and protein peak (22-26), are labelled according to the fractions from which they were collected. **B)** SDS-PAGE gel image from the second purification step. Samples from the protein flow-through (6-15), are labelled according to the fractions from which they were collected. Samples from fraction 19 and 23 were collected from the contaminant peaks (at increased imidazole concentration). Before TEV (BTEV) and after TEV (ATEV) samples are also shown.

The purification of OXA-48 S70A was performed with cells from the expression in Rosetta2(DE3)pLysS, samples were collected for SDS-PAGE gel analysis after the first HisTrap purification step (Figure 3-18 A). Fraction 18-23 were collected for dialysis and TEV cleavage. Fraction 4-8 was collected for protein concentration by centrifugation using Centriprep centrifugal filters (10 kDa MWCO), and OXA-48 S70A was concentrated to 10.1 mg/mL. Form the SDS-PAGE gel analysis from the second HisTrap purification it was clear that the protein was >95% pure. The total amount of OXA-48 S70A that was obtained after protein purification from 1 L cell culture is listed in Table 3-2.
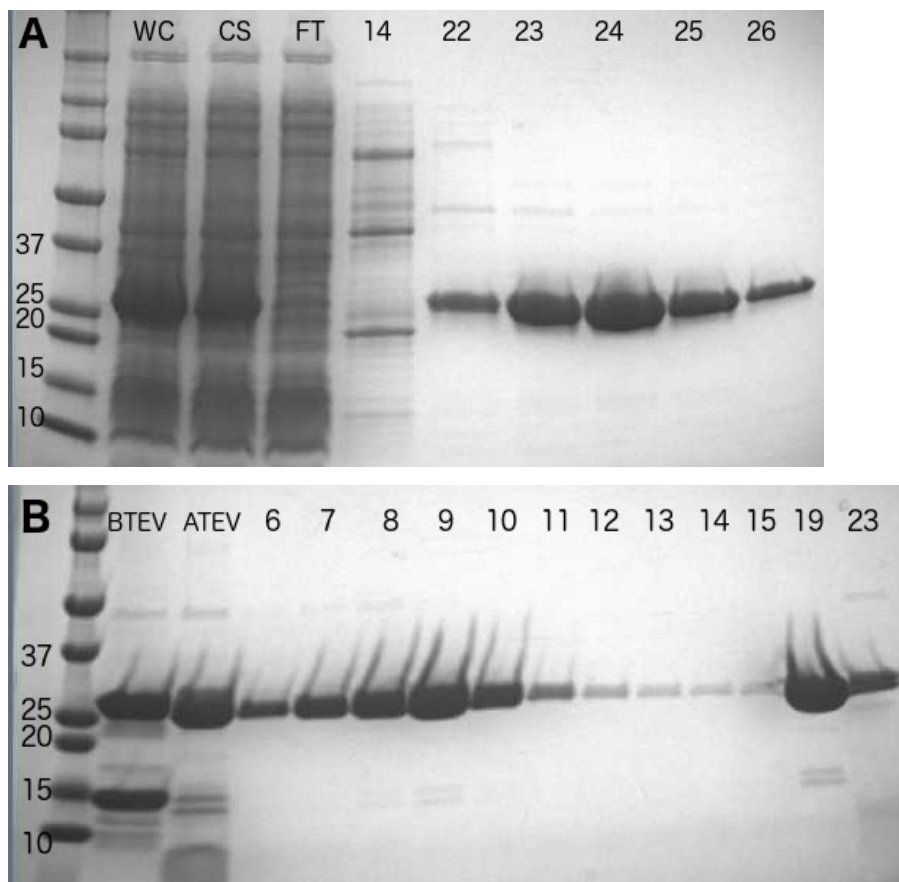

Figure 3-18: SDS-PAGE gel images from the purification of OXA-48 S70A. The ladder Precision Plus 10-250 kDa (left) show relevant molecular weight standards in kDa. **A)** SDS-PAGE gel image from the fist HisTrap purification step. The whole cell (WC) sample and cell supernatant (CS) sample are shown to indicate the protein solubility. The flow-through (FT) sample is shown as a control to check that no protein is eluted there, as would indicate an error. Sample(s) from the contaminant peak (11) and protein peak (17-23), are labelled according to the fractions from which they were collected. **B)** SDS-PAGE gel image from the second HisTrap purification step. Samples from the protein flow-through (3-8), are labelled according to the fractions from which they were collected. Samples from fraction 12 and 16 were collected from the contaminant peaks (at increased imidazole concentration). Before TEV (BTEV) and after TEV (ATEV) samples are shown.

OXA-48 R189A was purified from Rosetta2(DE3)pLysS cells as well, and the SDS-PAGE gel image form the first HisTrap purification step is shown in Figure 3-19 A. At this stage, the protein already seemed pure, based on the SDS-PAGE gel analysis, and fractions 11-15 were collected for dialysis and TEV cleavage. From the second HisTrap purification step fractions 2-7 were collected from the flow-through and pooled. OXA-48 R189A was concentrated to 9.8 mg/mL by centrifugation using the Centriprep centrifugal filters (10 kDa MWCO). It was clear from the gel analysis that the protein sample was >95% pure (Figure 3-19 B). The total amount of obtained OXA-48 R189A after protein purification from 1 L cell culture is listed in Table 3-2.
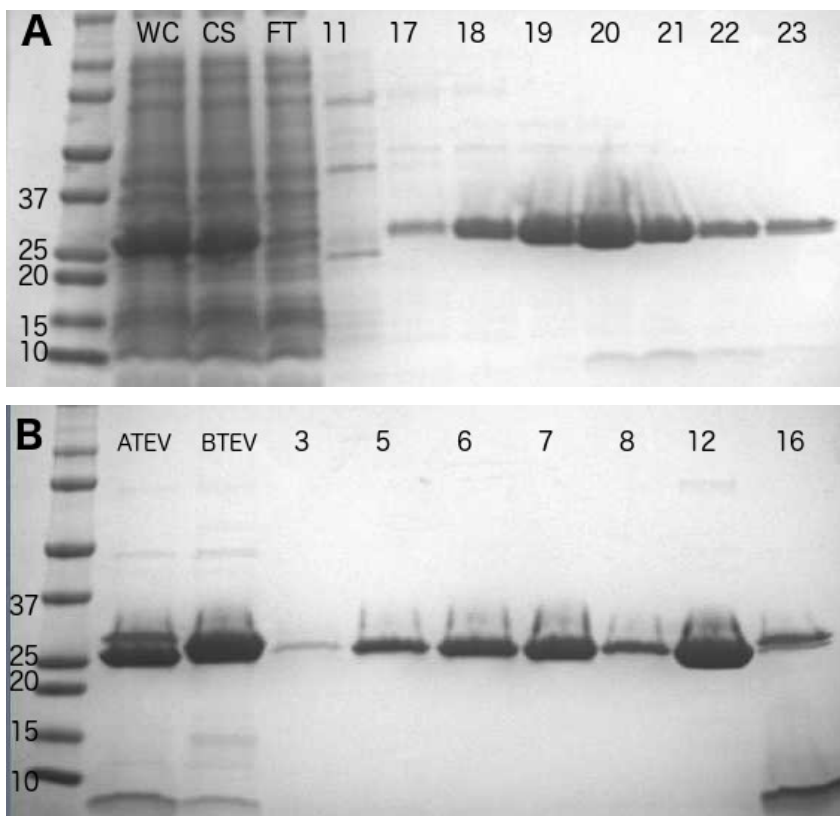

Figure 3-19: SDS-PAGE gel images from the purification of OXA-48 R189A. The ladder Precision Plus 10-250 kDa (left) show relevant molecular weight standards in kDa. **A)** SDS-PAGE gel image from the fist HisTrap purification step. The whole cell (WC) sample and cell supernatant (CS) sample are shown to indicate the protein solubility. The flow-through (FT) sample is shown as a control to check that no protein is eluted there, as would indicate an error. Sample(s) from the contaminant peak (8) and protein peak (11-15), are labelled according to the fractions from which they were collected. **B)** SDS-PAGE gel image from the second HisTrap purification step. Samples from the protein flow-through (2-7), are labelled according to the fractions from which they were collected. Samples from fraction 9 and 12 were collected from the contaminant peaks (at increased imidazole concentration). Before TEV (BTEV) and after TEV (ATEV) samples are shown.

From the SDS-PAGE gel analysis of OXA-48 R189A/R206A after the first HisTrap purification step (Figure 3-20 A), fractions 18-23 were collected for dialysis and TEV cleavage. Fraction 17 was also a part of the protein peak eluting during the imidazole gradient, but was excluded based on the SDS-PAGE gel analysis, where the sample contained almost as much contaminants as the protein of interest. From the second purification step HisTrap fraction 3-10 were pooled, based on the SDS-PAGE gel analysis (Figure 3-20 B). It was clear that OXA-48 R189A/R206A was >95% pure, and the protein sample was concentrated to 7.0 mg/mL by centrifugation using the Centriprep centrifugation filters (10 kDa MWCO). The total amount of obtained OXA-48 R189A/R206A after protein purification from 1 L cell culture is listed in Table 3-2.
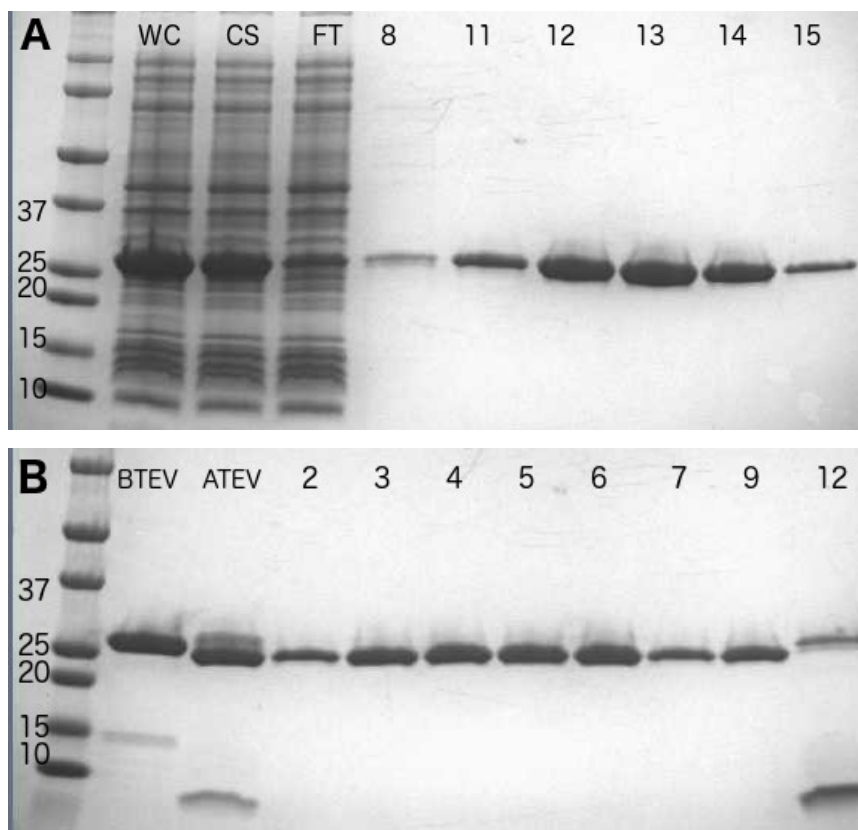

Figure 3-20: SDS-PAGE gel images from the purification of OXA-48 R189A/R206A. The ladder Precision Plus 10-250 kDa (left) show relevant molecular weight standards in kDa. **A)** SDS-PAGE gel image from the fist HisTrap purification step. The whole cell (WC) sample and cell supernatant (CS) sample are shown to indicate the protein solubility. The flow-through (FT) sample is shown as a control to check that no protein is eluted there, as would indicate an error. Sample(s) from the contaminant peak (12) and protein peak (17-23), are labelled according to the fractions from which they were collected. **B)** SDS-PAGE gel image from the second HisTrap purification step. Samples from the protein flow-through (2-10), are labelled according to the fractions from which they were collected. Samples from fraction 14 and 18 were collected from the contaminant peaks (at increased imidazole concentration). Before TEV (BTEV) and after TEV (ATEV) samples are shown.

The SDS-PAGE gel of OXA-48 P68A from the first HisTrap purification (Figure 3-21 A) does not include the whole cell (WC), cell supernatant (CS) and flow-through (FT) samples as these were lost. Fractions 17-21 were collected for dialysis and TEV cleavage. After the second HisTrap purification step the SDS-PAGE gel analysis (Figure 3-21 B) showed that the protein was >95% pure, thus fraction 3-14 were collected. Fractions 12-14 were also pooled with the other HisTrap fractions despite a very low protein concentration, since they appeared pure on the SDS-PAGE gel. OXA-48 P68A was concentrated to 5.5 mg/mL by centrifugation using the Centriprep centrifugal filters (10 kDa MWCO). The total yield of OXA-48 P68A after protein purification from 1 L cell culture is listed in Table 3-2.
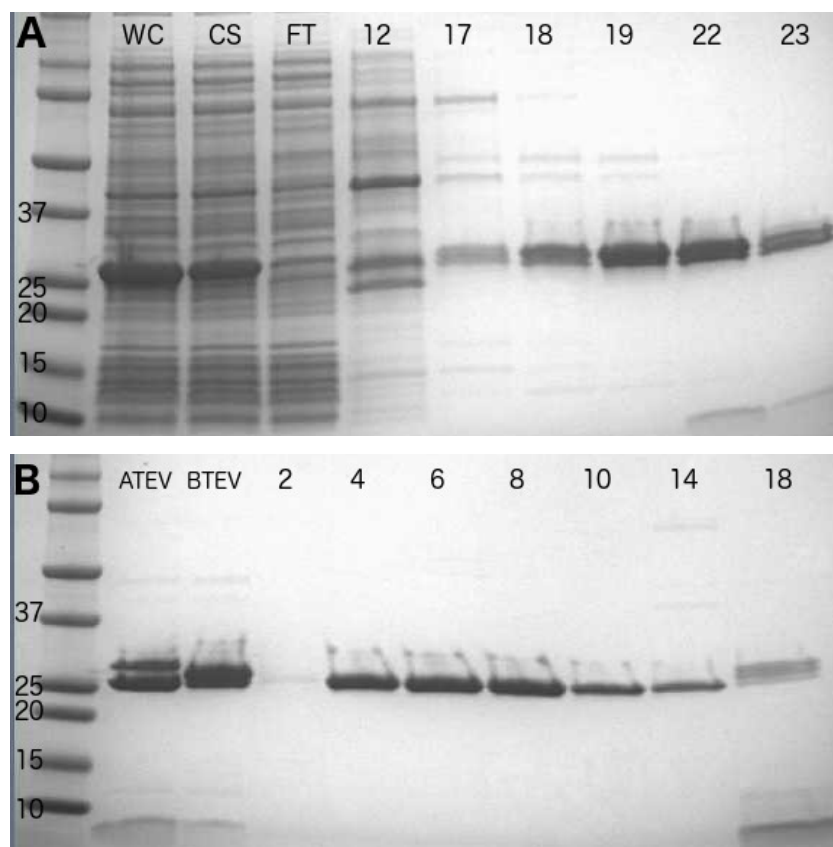

Figure 3-21: SDS-PAGE gel images from the purification of OXA-48 P68A. The ladder Precision Plus 10-250 kDa (left) show relevant molecular weight standards in kDa. **A)** SDS-PAGE gel image from the fist HisTrap purification step. WC, CS and FT samples were lost. The gel had to be re-ran, and before TEV (BTEV) and after TEV (ATEV) samples were included. Sample(s) from the contaminant peak (11) and protein peak (17-21), were labelled according to the fractions from which they were collected. **B)** SDS-PAGE gel image from the second HisTrap purification step. Samples from the protein flow-through (2-14), are labelled according to the fractions from which they were collected. Samples from fraction 19 and 24 were collected from the contaminant peaks (at increased imidazole concentration).

Purification of the double mutant P68A/Y211S showed a good amount of protein after the first HisTrap purification (Figure 3-22 A), fractions 16-21 were collected for dialysis and TEV cleavage. After the second HisTrap purification the protein sample was determined to be >95% pure based on the SDS-PAGE gel analysis (Figure 3-22 B), and fraction 3-10 was collected. OXA-48 P68A/Y211S was concentrated to 6.9 mg/mL by centrifugation using the Centriprerp centrifugal filter (10 kDa MWCO). The total yield of OXA-48 P68A/Y211S after protein purification from 1 L cell culture is listed in Table 3-2.
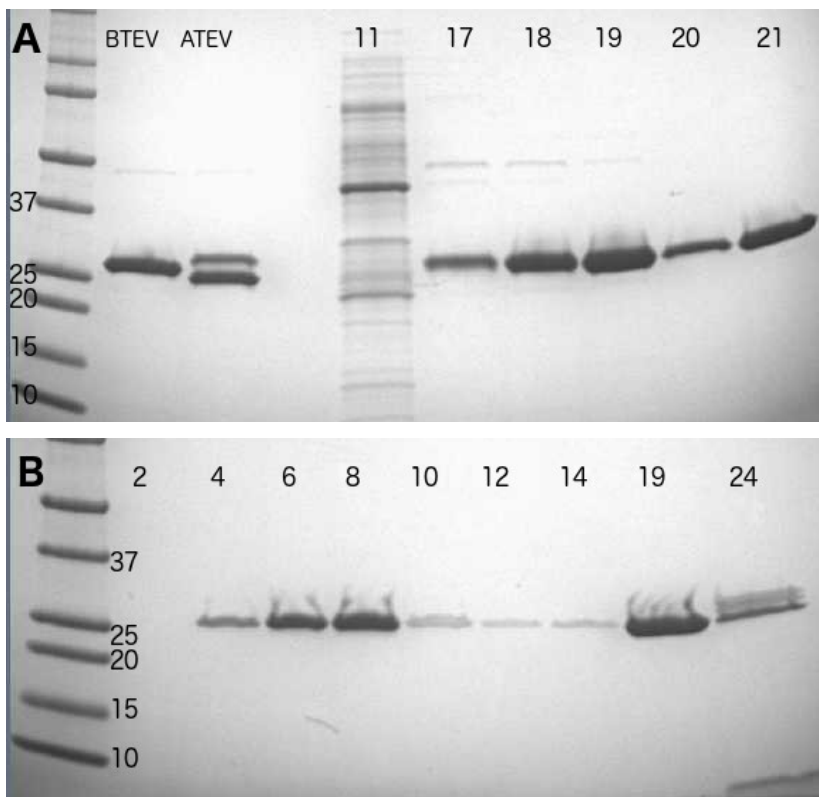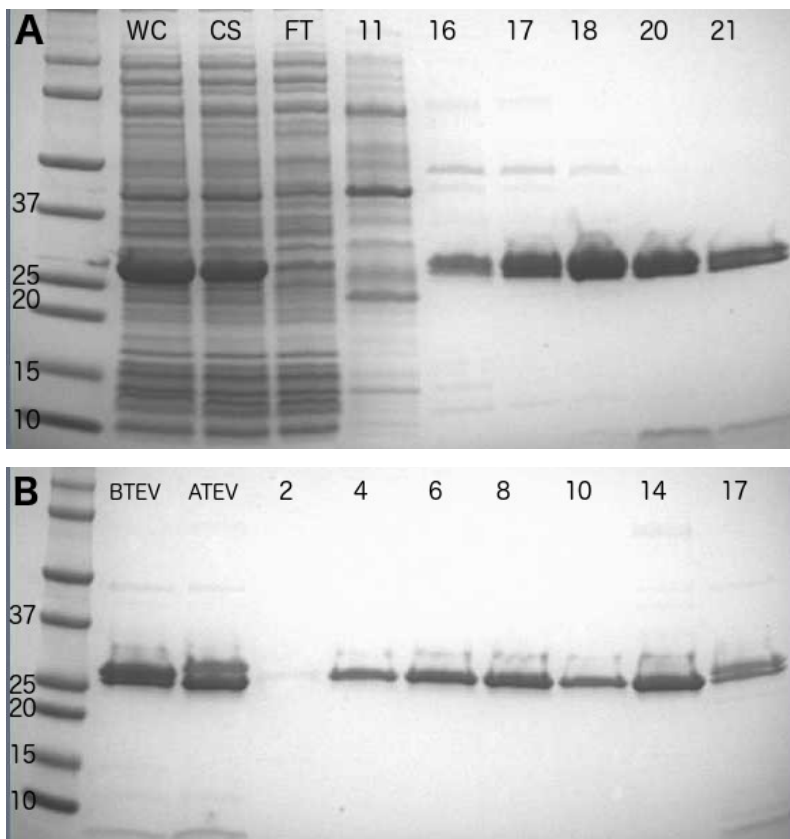

Figure 3-22: SDS-PAGE gel images from the purification of OXA-48 P68A/Y211S. The ladder Precision Plus 10-250 kDa (left) show relevant molecular weight standards in kDa. **A)** SDS-PAGE gel image from the fist HisTrap purification step. The whole cell (WC) sample and cell supernatant (CS) sample are shown to indicate the protein solubility. The flow-through (FT) sample is shown as a control to check that no protein is eluted there, as would indicate an error. Sample(s) from the contaminant peak (11) and protein peak (16-21), are labelled according to the fractions from which they were collected. **B)** SDS-PAGE gel image from the second HisTrap purification step. Samples from the protein flow-through (2-10), are labelled according to the fractions from which they were collected. Samples from fraction 14 and 17 were collected from the contaminant peaks (at increased imidazole concentration). Before TEV (BTEV) and after TEV (ATEV) samples are shown.

3.2 Crystallization and crystal structure analysis

3.2.1 Crystallization of OXA-48 like β-lactamases

A part of this thesis was to gain better insight into the structure activity relationship between OXA-48 like β-lactamases. Therefore OXA-181 and the novel β-lactamase OXA-436 were crystallized and crystal structures solved; and a new crystal structure of OXA-163 was determined to 2.05, 2.20 and 2.07 Å resolution, respectively.

The crystal structure of OXA-181 (PDB: 5OE0) and OXA-436 was solved by Dr. Bjarte A. Lund, and the crystal structure of OXA-163 (PDB: 5ODZ) was solved by researcher Hanna-Kirsti S. Leiros. X-ray data collection and processing statistics for OXA-181 and OXA-163 are given in the article "Structure, activity and thermostability investigations of OXA-163, OXA-181 and OXA-245 using biochemical analysis, crystal structures and differential scanning calorimetry analysis", supplied in Appendix Paper 1.

In order to obtain protein crystals for structure determination, crystallization trials were set up both with the hanging-drop method (by hand) and by the sitting-drop method (crystallization robot). The crystallization conditions yielding diffracting crystals for OXA-181, OXA-163 and OXA-436, used for the structure determination, are listed in Table 2-5.

2-4 protein crystals were collected for each enzyme, from different crystallization conditions, and/or multiple protein crystals within the same crystallization drop. The crystals were cryo-protected, flash frozen, and stored in liquid nitrogen, before being sent to a synchrotron for X-ray data collection. OXA-181 was cryo-protected in 0.1 M Tris pH 7.0, 0.2 M $(NH_4)_2SO_4$, 20.5% PEG MME 5000, and 20% ethylene glycol. A crystal image of a OXA-181 crystal is shown in Figure 3-23 A. OXA-181 protein crystallization yielded long, but solid, needle-like crystals. OXA-163 was cryo-protected in 0.1 Tris pH 9.0, 28% PEG MME 500, and 17% ethylene glycol. OXA-163 crystallization yielded few, small, and square-looking crystals, as shown in Figure 3-23 B. The cryo-solution for OXA-436 was 0.1 M HEPES pH 8.0, 25% PEG 3350, 0.2 M $NaCH_3COO$, and 25% ethylene glycol. Small square-shaped crystals were obtained.
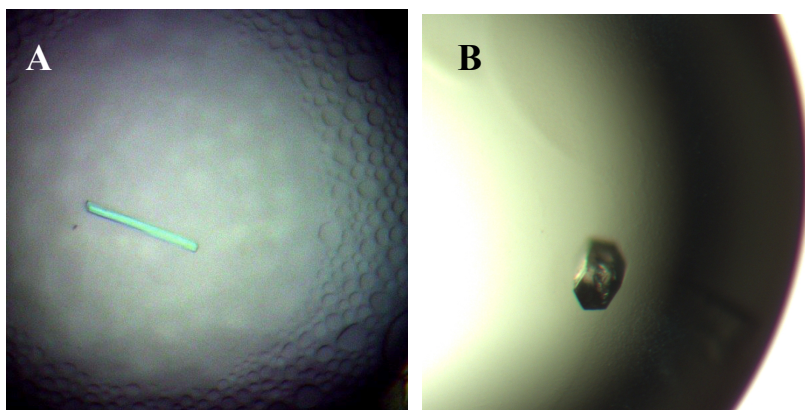
Figure 3-23: A) Protein crystal of OXA-181, grown from well conditions with 0.1 M Tris pH 7.0, 0.2 M $(NH_4)_2SO_4$, 20.5% PEG MME 5000. **B)** Protein crystal of OXA-163, grown from well conditions with 0.1 Tris pH 9.0, 28% PEG MME 500.

3.2.2 Crystallization and structure analysis of OXA-48 R189A, S70A, S70T and S70T/T71S

Crystallization trials were set up using both the hanging-drop method (manually) and the sitting-drop method (crystallization robot), for the OXA-48 mutants S70A, S70T, S70T/T71S, and R189A. This was done to confirm the mutation, and study the effect from the mutation to the surrounding protein structure. Crystallization trials were only set up for the mentioned mutants since these were the first to be expressed and purified.

The resolution of the crystal structures of OXA-48 S70A, S70T, S70T/T71S and R189A were determined to 1.85, 2.50, 1.89, and 2.55 Å resolution, respectively. The crystal structures were solved by researcher Hanna-Kirsti S. Leiros. X-ray data collection and processing statistics for the mutants are supplied in Appendix Table A1.

3 protein crystals were collected for each mutant, from the same crystallization drop, or from different crystallization conditions. The crystallization conditions from the diffracting protein crystals of OXA-48 S70A, S70T, S70T/T71S and R189A are given in Table 2-6. The crystals were sent to the synchrotron BESSY, Berlin for X-ray data collection. Images of the protein crystals, used to determine the crystal structure are shown in Figure 3-24.

The protein crystals were cryo-protected before being flash frozen and stored in liquid nitrogen. S70A was cryo-protected in 0.1 M BIS-Tris propane pH 9.5, and 38% PEG 400. S70T in 0.1 M BIS-Tris propane pH 9.5, 19% PEG MME 5000, and 15% ethylene glycol. S70T/T71S in 0.1 M BIS-Tris propane pH 8.5, 20% PEG MME 5000, and 15% ethylene glycol. And R189A in 0.1 M BIS-Tris propane pH 9.5, 16% PEG MME 5000, and 20% ethylene glycol.
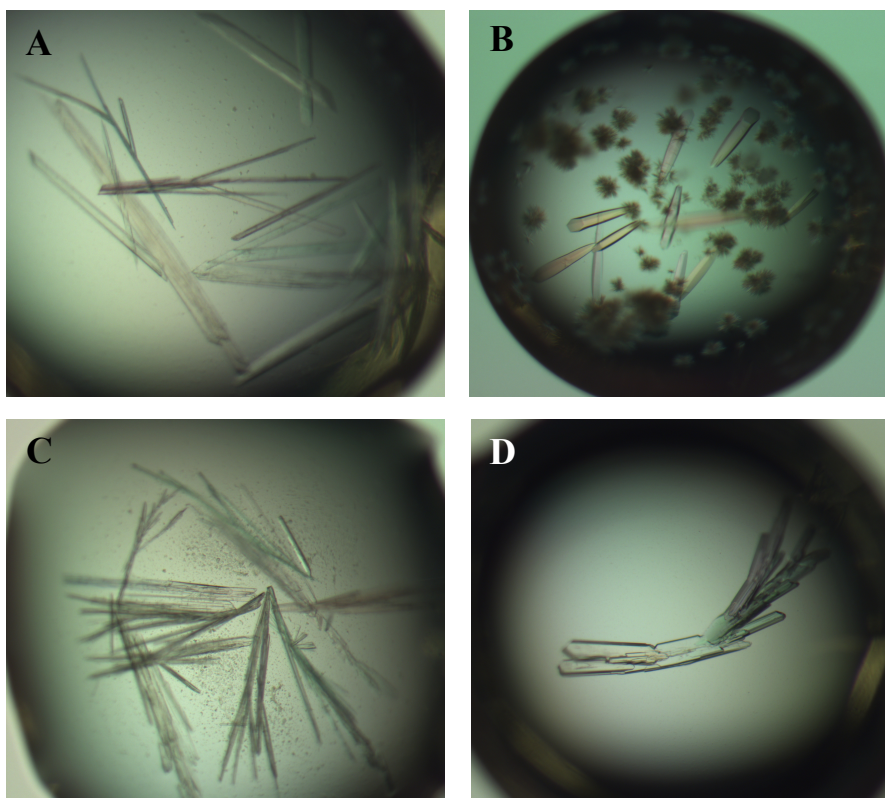
Figure 3-24: A) Protein crystal of OXA-48 R189A, grown from 0.1 M BIS-Tris propane pH 9.5, 16% PEG MME 5000. **B)** Protein crystal of OXA-48 S70A, from reservoir solution with 0.1 M BIS-Tris propane pH 9.5, 38% PEG 400. **C)** Protein crystal of OXA-48 S70T, grown from conditions with 0.1 M BIS-Tris propane pH 9.5, 19% PEG MME 5000. **D)** Protein crystal of OXA-48 S70T/T71S, grown from 0.1 M BIS-Tris propane pH 8.5, 20% PEG MME 5000.

The mutations had already been verified by DNA sequencing and were also confirmed by studying the $2F_o$-F_c electron density map for the substituted residues. OXA-48 S70A crystal structure was solved at quite high resolution (1.85 Å), the $2F_o$-F_c map traced the amino acids clearly. It seemed evident that the polar hydroxyl group of serine was not present in the structure (Figure 3-25 A). For the OXA-48 S70T mutant it was not as clear, since the resolution was significantly lower (2.50 Å), and the serine and threonine residues differ only by a methyl group on threonine (Figure 3-25 B). OXA-48 S70T/T71S had two substituted residues and 1.89 Å resolution, which made it quite clear from the $2F_o$-F_c map that an extra methyl group should be found at residue 70, and be removed from residue 71, giving the correct mutation (Figure 3-25 C). The resolution was quite low for OXA-48 R189A (2.55 Å), but the significant size difference between the amino acids alanine and arginine, made it clear that R189 had been substituted with a much smaller amino acid (Figure 3-25 D).
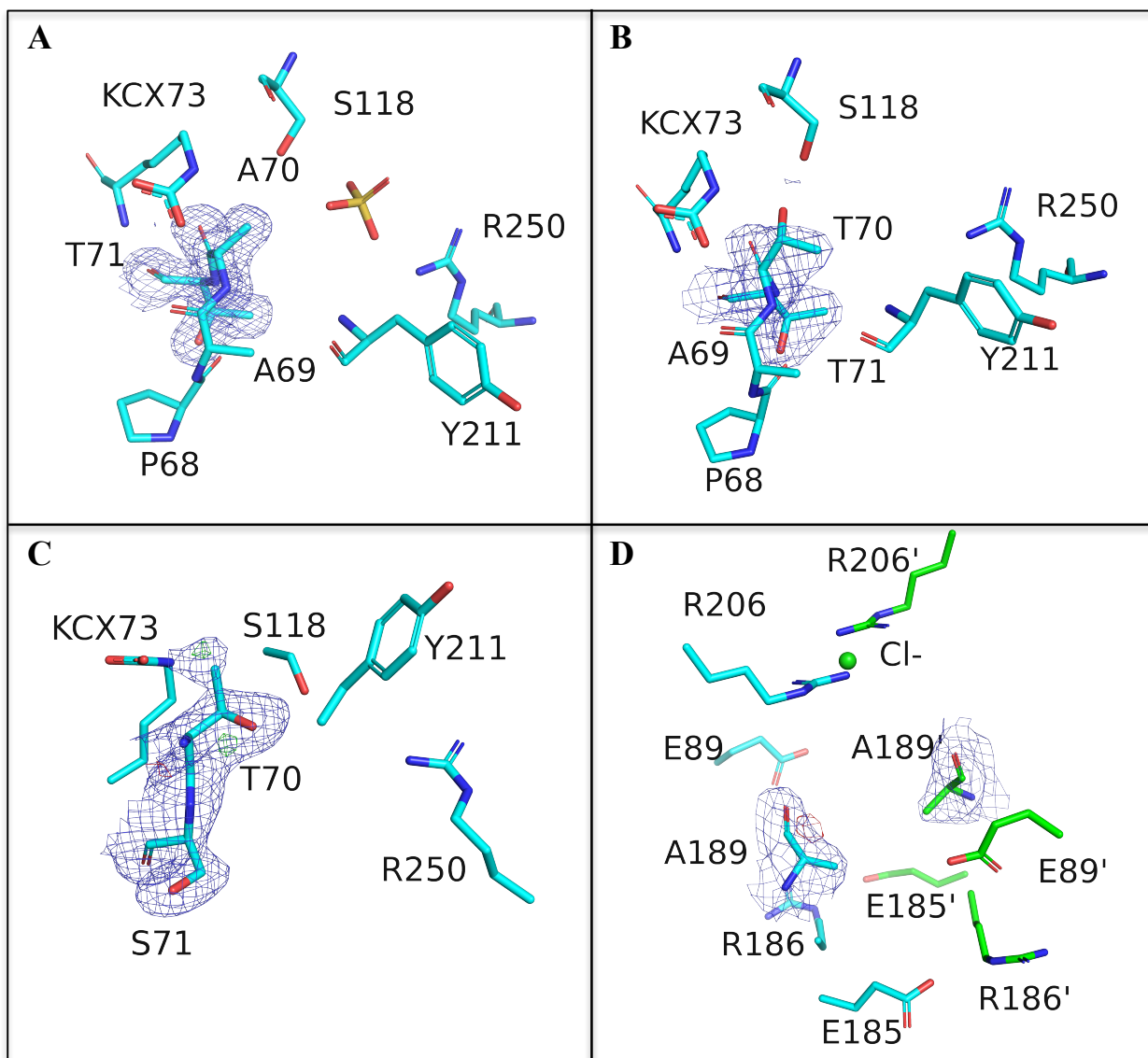
Figure 3-25: Crystal structures of OXA-48 S70A, S70T, S70T/T71S, and R189A. Electron density maps $2F_o$-F_c (1.0σ, blue) and F_o-F_c maps (+4.0σ green/-4.0σ red) are shown for the substituted residues, to give evidence of the mutation. Electron density maps and amino acids from the crystal structures by researcher Hanna-Kirsti S. Leiros. **A)** S70A, with mutation clearly confirmed by the $2F_o$-F_c map. The relatively high resolution makes it possible to easily trace the shape of the amino acid, the polar hydroxyl group of serine seems to be absent. **B)** S70T, due to lower resolution the mutation from serine to threonine (addition of one methyl group) is not that evident in the electron density map. **C)** S70T/T71S, due to a quite high resolution it is easier to trace the $2F_o$-F_c map to the amino acid structure, and it seems clear that the correct mutation has occurred. **D)** R189A, the resolution is lower but the significant size difference makes it evident from the $2F_o$-F_c map that arginine is replaced by alanine.

3.3 Thermal stability and dimer affinity

3.3.1 Thermal stability investigations by differential scanning calorimetry (DSC)

OXA-48 and OXA-48 like enzymes differ only by a few amino acid substitutions and/or deletions, the effect from these mutations is not fully elucidated. Both OXA-181, and OXA-245 for example, have a very similar catalytic activity compared to OXA-48 [54]. OXA-181 differs from OXA-48 by four amino acid substitutions; T104A, N110D, E168Q, and S171A. OXA-245 is the enzyme with the highest sequence identity to OXA-48, differing only by one amino acid substitution; E125Y. OXA-163, which has a more different catalytic activity compared to OXA-48 [53] has a four-amino acid deletion (residue 214-217), shortening the loop between β-sheet 7 and 8, in addition to one amino acid substitution S212D. OXA-436 also displays a kinetic activity similar to that of OXA-48 has the lowest sequence identity to OXA-48 of all the identified OXA-48 like β-lactamases, by 91.3% sequence identity [55]. The sequence alignment of OXA-48, OXA-181, OXA-245, OXA-163 and OXA-436 are shown in Figure 1-7.

To investigate the differences between OXA-48 and the OXA-48 like enzymes the thermal stability of OXA-181, OXA-245, OXA-163 and OXA-436 were studied using DSC to determine the transition midpoint, or melting temperature (T_m) of the proteins. OXA-48 mutants affecting the dimer interface (R206A, R189A, R189A/R206A) were also investigated.

All the enzymes (including the mutants) unfolded in a single transition step, without any stable intermediate, as seen from the shape of the melting curves. This allowed for using the two-state transition model, when calculating the thermodynamic data (see section 1.5.1). The DSC data transition curve, with the fitted theoretical two-state model, for OXA-48 is shown in Figure 3-26, as an example. DSC transition curves for the enzymes dialyzed in 50 mM phosphate buffer pH 7.2, are supplied in Appendix Figure A1. The transition peaks spanned from 5-7°C. The reason that some peaks were slightly broader than others were not completely clear, but protein concentration, sample inhomogeneity and/or minor impurities may affect this.

According to interaction analysis of the crystal structure of OXA-48, OXA-181, OXA-245, and OXA-163 10-20% of the surface is buried in dimerization [54, 108]. Gel filtration experiments as well as microscale thermophoresis also indicated a strong dimer formation for OXA-48 and OXA-48 R206A mutant (unpublished data). The DSC curves were therefore fitted with the molecular weights and concentrations of dimers. This assumption was also confirmed by comparing the van´t Hoff enthalpy (ΔH_{vH}) calculated from the fitted two-state model, and

the calorimetric enthalpy (ΔH_{cal}) from the transition curves. When assuming dimer formation, the two enthalpy values were approximately the same, but when using molecular weights and protein concentrations of the monomeric form the two values deviated more. In the case of the monomer ΔH_{vH}/ ΔH_{cal} generally gave values much higher than 1, indicating that dimer is the most likely state. However, the proportions between the enthalpies varied from run to run, and the method should therefore not be used to determine monomer or dimer form of the protein, merely to determine if the two-state unfolding model fits well with the given conditions.
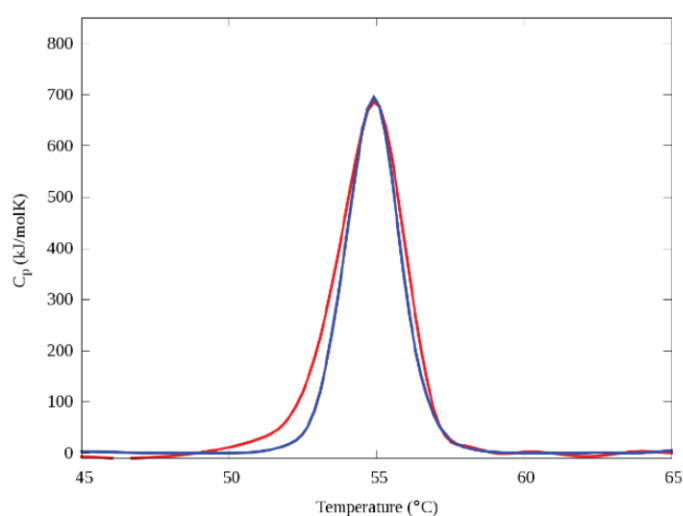
Figure 3-26: DSC transition curve (red) for OXA-48 dimer, with the fitted two-state model (blue) to be able to calculate the enthalpy of protein unfolding. The temperature is given along the x-axis, and the heat capacity along the y-axis. Figure from reference [54].

The enzymes were dialyzed overnight in 50 mM HEPES pH 7.0 and 50 mM K_2SO_4 and the determined T_m and enthalpy from the DSC experiments are given in Table 3-3. A lower thermal stability was found for OXA-181 (52.6°C) and OXA-436 (53.8°C) compared to OXA-48 (55.2°C), while OXA-245 (55.8°C) actually displayed a slightly increased thermal stability compared to OXA-48. OXA-163 showed the lowest stability (49.4°C) of the OXA-48 like enzymes tested. Greater active site flexibility was proposed to explain the observed easier access for cephalosporin hydrolysis, and this might also reduce the thermal stability [53, 109]. These findings together with kinetic and structural data for OXA-48, OXA-181, OXA-245 and OXA-163 were used to discuss which residues were responsible for the difference in thermal stability in the article "Structure, activity and thermostability investigations of OXA-163, OXA-181 and OXA-245 using biochemical analysis, crystal structures and differential scanning calorimetry analysis" by Lund et al [54]. The full article is supplied in Appendix Paper 1. In the article, it was determined that the loss of residues 214-217 in OXA-163 disrupts two

ionic bonds (Arg214-Asp159 and Glu216-Lys218) found in OXA-48, causing a reduced thermal stability by structure destabilization, but which allows for greater flexibility. For OXA-181 the N110D substitution introduces an ionic bond from Asp110 to His90, causing the His90 residue to shift, disrupting the ionic network Asn88-His90-Glu89. The polarity of the protein surface is also decreased by the mutations T104A and S117A for OXA-181. Taken together this may lower the thermal stability of OXA-181 compared to OXA-48. The slightly increased stability of OXA-245 compared to OXA-48 is likely to originate from the one residue substitution Glu125 to Tyr. Glu125 forms an ionic bond with Arg129 in OXA-48. However, Tyr125 forms π-π stacking interactions with Phe126 and Phe93, which may compensate for the loss of the ionic bond [54] and explain the +0.5°C higher temperature stability of OXA-245.

The OXA-48 mutants; R189A, R189A/R206A and R206A showed a quite significant reduction in thermal stability. OXA-48 R206A (50.8°C) and R189A (51.1°C) displayed a similar stability, while the double mutant R189A/R206A (42.8°C) showed a severely reduced thermal stability (Table 3-3). From size-exclusion chromatography experiments OXA-48 is shown to be a monomer at pH 4.0 (phosphate-citrate buffer) (unpublished data by Lund et al.). OXA-48 and OXA-48 R189A were therefore dialyzed in phosphate-citrate buffer pH 4.0 prior to thermal stability investigation by DSC. This resulted in T_m of 41.0°C (OXA-48) and 40.9°C (OXA-48 R189A), thus being quite similar to the T_m obtained for the double mutant (42.8°C for OXA-48 R189A/R206A). This indicate that the dimer:monomer equilibrium has been moved towards monomer formation, and that the thermal stability of monomers have been measured.

The reduced thermal stability for the suspected monomer may be a reason for the dimer formation, to further stabilize the protein. However, the low pH and buffer composition may also affect the thermal stability of the protein in other ways than through monomer formation, and contribute to the observed low T_m. Also, comparison of the enthalpies from fitting of the two-state model still indicated that the dimeric molecular weight and concentration gave the best fit for both the double mutant and OXA-48 at pH 4.0. This indicates that the monomer-formation for the OXA-48 double mutant is not as certain as first assumed.

A study by Stojanoski et al. [110] determined the midpoint melting temperature of OXA-48 to be 58.9°C by circular dichroism using 50 mM phosphate buffer pH 7.2. We then became interested in testing whether the method or the buffer was responsible for the higher T_m, OXA-48 was dialyzed in the 50 mM phosphate buffer pH 7.2, before investigating the thermal stability by DSC. This gave a melting temperature of 59.1°C for OXA-48 (Table 3-4),

consistent with the circular dichroism results. The buffer composition is well known to affect the protein stability, but these buffers composition, HEPES/K_2SO_4 pH 7.0 versus $PO_4{}^{2-}$ pH 7.2, differed mainly by the addition of potassium sulphate, and the relatively large change in thermal stability was therefore interesting. It was decided to test OXA-181, OXA-245, OXA-163 and the mutants OXA-48 R206A, R189A and R189A/R206A in 50 mM phosphate buffer pH 7.2 as well, to study the effect. A comparison of the DSC curves of OXA-48 and OXA-48 R206A, in the two different buffers is shown in Figure 3-27, as an example.

The DSC results from duplicate measurements using 50 mM phosphate buffer pH 7.2, listing the transition midpoint temperatures (T_m) and enthalpies (ΔH) are given in Table 3-4.

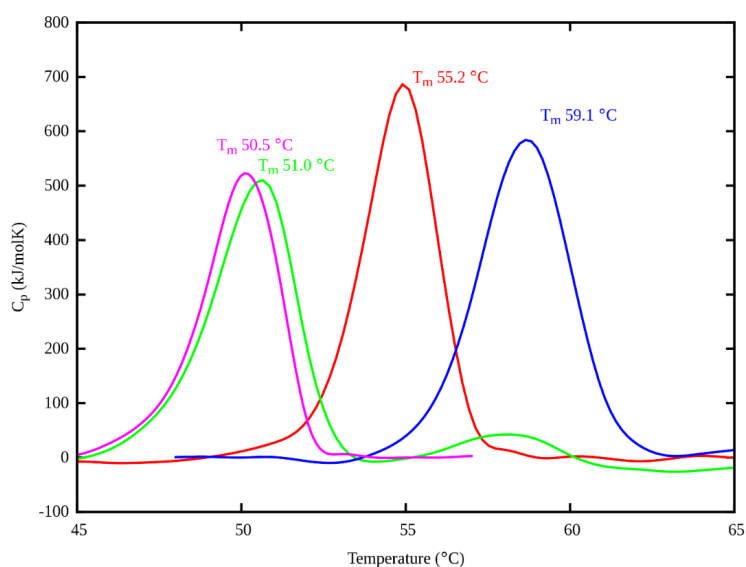**Figure 3-27:** DSC curves for OXA-48 and the mutant R206A, tested in 50 mM HEPES pH 7.0 and 50 mM K_2SO_4 (OXA-48; red, OXA-48 R206A; green) and 50 mM sodium phosphate buffer pH 7.2 (OXA-48; blue, OXA-48 R206A; magenta). The transition midpoint temperatures are indicated. OXA-48 shows a distinct difference in T_m between the two different buffers. Figure by Dr. Bjarte A. Lund (unpublished data).

Table 3-3: Transition midpoint temperature (T_m) and unfolding enthalpy (ΔH) with standard deviations, calculated from two-state model with the enzyme molecular weight and concentration as dimer. Using 50 mM HEPES pH 7.0, 50 mM potassium sulpahte buffer for OXA-48, OXA-181, OXA-245, OXA-436 and OXA-48 mutants R189A, R206A, and R189A/R206A, determined by differential scanning calorimetry (DSC).

Enzyme	Run 1		Run 2	
	T_m (°C)	ΔH(kJ/mol)	T_m (°C)	ΔH(kJ/mol)
OXA-48	55.12 ± 0.01	1336 ± 6	55.37 ± 0.01	1638 ± 8
OXA-163	49.40 ± 0.01	1247 ± 6	49.39 ± 0.01	1311 ± 4
R206A	50.94 ± 0.01	1386 ± 7	51.02 ± 0.01	1432 ± 6
OXA-181	52.53 ± 0.04	1248 ± 17	52.96 ± 0.02	1606 ± 13
OXA-245	55.67 ± 0.01	1800 ± 12	55.87 ± 0.01	1639 ± 9
R189A	49.77 ± 0.01	1256 ± 6	50.23 ± 0.02	1313 ± 11
R206A/R189A	43.55 ± 0.02	957 ± 5	43.61 ± 0.02	965 ± 6
OXA-436	53.92 ± 0.01	1547 ± 9	53.71 ± 0.01	1384 ± 5

Table 3-4: Transition midpoint temperature (T_m) and unfolding enthalpy (ΔH) with standard deviations, calculated from two-state model with the enzyme molecular weight and concentration as dimer. Using 50 mM phosphate buffer pH 7.2, for OXA-48, OXA-181, OXA-245 and OXA-48 mutants R189A, R206A, and R189A/R206A, determined by differential scanning calorimetry (DSC). Standard deviation and enthalpy was not obtained for one of the OXA-48 R189A measurements, due to baseline error. However, the melting temperature was very similar between the duplicates, and the second measurement was considered reliable.

Enzyme	Run 1		Run 2	
	T_m (°C)	ΔH(kJ/mol)	T_m (°C)	ΔH(kJ/mol)
OXA-48	59.08 ± 0.01	1558 ± 11	59.07 ± 0.01	1518 ± 9
OXA-163	54.15 ± 0.01	1521 ± 9	53.73 ± 0.01	1461 ± 5
R206A	50.54 ± 0.01	1371 ± 6	51.15 ± 0.01	1306 ± 4
OXA-181	55.14 ± 0.01	1371 ± 6	55.34 ± 0.01	1419 ± 6
OXA-245	59.41 ± 0.02	1402 ± 13	59.35 ± 0.02	1425 ± 13
R189A	51.17	---	51.01 ± 0.01	1142 ± 4
R206A/R189A	42.65 ± 0.02	887 ± 4	42.96 ± 0.01	921 ± 3

Comparison of T_m between the two buffers for OXA-48, OXA-245 and OXA-163 showed a 3.5-4.5°C increased melting temperature in 50 mM phosphate buffer pH 7.2, compared to 50 mM HEPES pH 7.0 and 50 mM potassium sulphate. The T_m for OXA-181 increased by only 2.5°C. OXA-48 R189A and R189A/R206A differed by an increased temperature of approximately 1°C, while R206A did not differ at all. One possible explanation for this is that the sulphate ion from the first buffer replaces the chloride ion observed in the anion binding between Arg206 and Arg206´ in the dimer interface (see Figure 1-8). A sulphate molecule has a large molecular radius than the chloride ion observed in the crystal structure of OXA-48, and could therefore potentially destabilize the dimer. This would explain why OXA-48 R206A is unaffected, as this interaction is already disrupted. R189A could be only slightly affected by this as the dimer is already destabilized, while the native enzymes will be affected the most since the dimer is stable. However, this does not explain why OXA-48 R189A/R206A is not also unaffected. It must also be taken into consideration that there is a significant size difference between the chloride and sulphate ion, and thus it is uncertain how likely the suggested $SO_4{}^{2-}$ Arg206 binding is.

3.3.2 Investigating the dimer affinity by microscale thermophoresis (MST)

From previous MST experiments the dimer affinity for the OXA-48 R206A mutant was determined to be 700 ± 300 pM. It was not possible to obtain any reliable dose-response curves for OXA-48, and it was reasoned that this might be due to an even stronger dimer affinity in OXA-48, compared to OXA-48 R206A (unpublished data). It was attempted to measure the dimer affinity (K_d) for OXA-48 R189A and R189A/R206A to more accurately study the amino acid substitution upon dimer formation. However, determining the dimer affinity by MST for OXA-48 R189A was unsuccessful. K_d value was obtained for OXA-48 R189A/R206A and determined to 21.8 ± 4.4 nM, with good signal to noise ratio, as shown in the dose-response curve from the MST experiments (Figure 3-28), from which the dissociation constant is calculated. As previously mentioned OXA-10 and OXA-14 was reported with a dimer affinity in the nano molar to micro molar range [58]. A K_d value of 22 nM, therefore means the dimer affinity for OXA-48 R189A/R206A is still quite strong compared to other OXA-dimers, even though the double mutant has a lower dimer affinity than the one reported for OXA-48 R206A. This indicates that OXA-48 has an unusually strong dimer formation, where salt-bridges are important for the affinity.
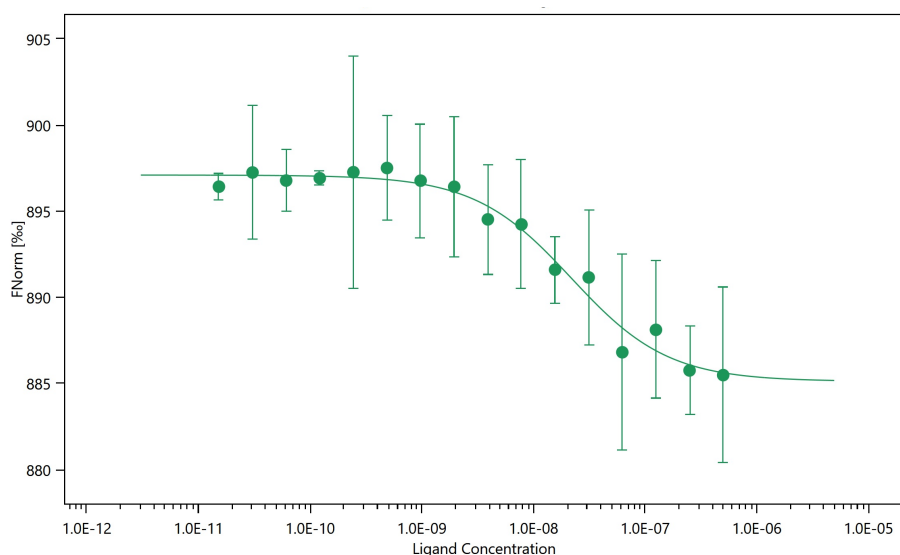
Figure 3-28: Microscale thermophoresis curve from three individual measurements with error bars representing the standard deviation. OXA-48 R189A/R206A was labelled using RED-dye, and measured at a concentration of 150 pM, with unlabeled OXA-48 R189A/R206A from 0.015 nM-500 nM. A dissociation constant (K_d) of 21.8 ± 4.4 nM was derived for the dimer interaction from the normalized fluorescence (ΔFNorm; y-axis), plotted against the concentration of the unlabelled OXA-48 R189A/R206A (x-axis).

3.3.3 Size-exclusion chromatography analysis of the dimer and monomer formation

To study the dimer interaction and stability OXA-48 and OXA-48 R206A were tested at different protein concentrations, as well as different pH values (phosphate-citrate buffer with 50 mM K_2SO_4 pH 4.0, 5.0, 6.0, 7.0) by staff engineer Trine Carlsen and Dr. Bjarte A. Lund in a previous size-exclusion chromatography experiment. Both proteins were determined to be dimers from pH 5.0-7.0, and monomers at pH 4.0. Indicating that salt-bridges are important for the dimer association. Both proteins also eluted as dimers at protein concentrations down to 35 nM, indicating a dimer affinity in the nM range and lower (unpublished data).

To further investigate the dimer affinity size-exclusion chromatography was conducted for OXA-48 mutants R189A and R189A/R206A using the same buffer conditions as previously mentioned. In addition, OXA-48 and OXA-48 R206A were tested by SEC using a phosphate-citrate buffer at pH 4.4 to hopefully, better study the transition between dimer and monomer. The resulting elution volumes are shown in Figure 3-29.

The molecular weight standards Conalbumin (76 kDa) and Carbonic anhydrase (29 kDa) were eluted at 14.4 and 16.8 mL respectively, using phosphate-citrate buffer pH 7.0 with 50 mM potassium sulphate. From the previous SEC experiments the OXA-48 dimer eluted at 15.4 mL, and the monomer at 16.5 mL, which correlates well with the elution volumes of the standards used. At pH 4.4 OXA-48 R206A eluted at 16.5 mL, indicating monomer formation. OXA-48 eluted at 15.8 mL, which was a bit surprising. We anticipated to obtain two separate

91

peaks showing both monomer and dimer formation from the same elution, however one slightly displaced elution peak was obtained instead. This was also observed for OXA-48 R189A which eluted at 16.6 mL using pH 4.4, indicating monomer formation, and at 15.8 mL at both pH 7.0 and 6.0 suggesting more of an equilibrium. OXA-48 R189A/R206A was clearly the most destabilized of the mutants tested, and eluted at 16.6 mL, indicating monomer formation, at both pH 6.0 and 7.0. At pH 7.0 a small shoulder-like peak was observed at 14.4 mL next to the main elution peak. The reason for this was not clear.

Elution peak displacement was also reported by Woodbury et al. [111] for an oligomeric protein, observing that the elution volume increased with decreasing protein concentrations. It was suggested that the monomer:dimer equilibrium favored the monomer formation at lower concentrations. The protein dimer might therefore dissociate into a monomer during the column migration as the sample is diluted during the experiment. Woodbury et al. observed a slightly asymmetric shape to their elution peaks, suggested as a result of the monomer trailing [111]. It is possible that this is also the case for our results presented here. A slight asymmetric elution peak shape is observable, especially for OXA-48 at pH 4.4 (Figure 3-29). Even though OXA-48 was previously reported to not be significantly affected by concentration changes, it is possible that the dimer interface mutations destabilized the protein enough to be affected by this. Whether or not this is the case, R189A/R206A has shown to be the least stable dimer, eluting in fact, as a monomer even in neutral pH. R189A is more stable eluting as a mix of monomer and dimer at neutral pH, while R206A is the most stable dimer requiring a pH as low as 4.4 to elute as a monomer (Figure 3-29).
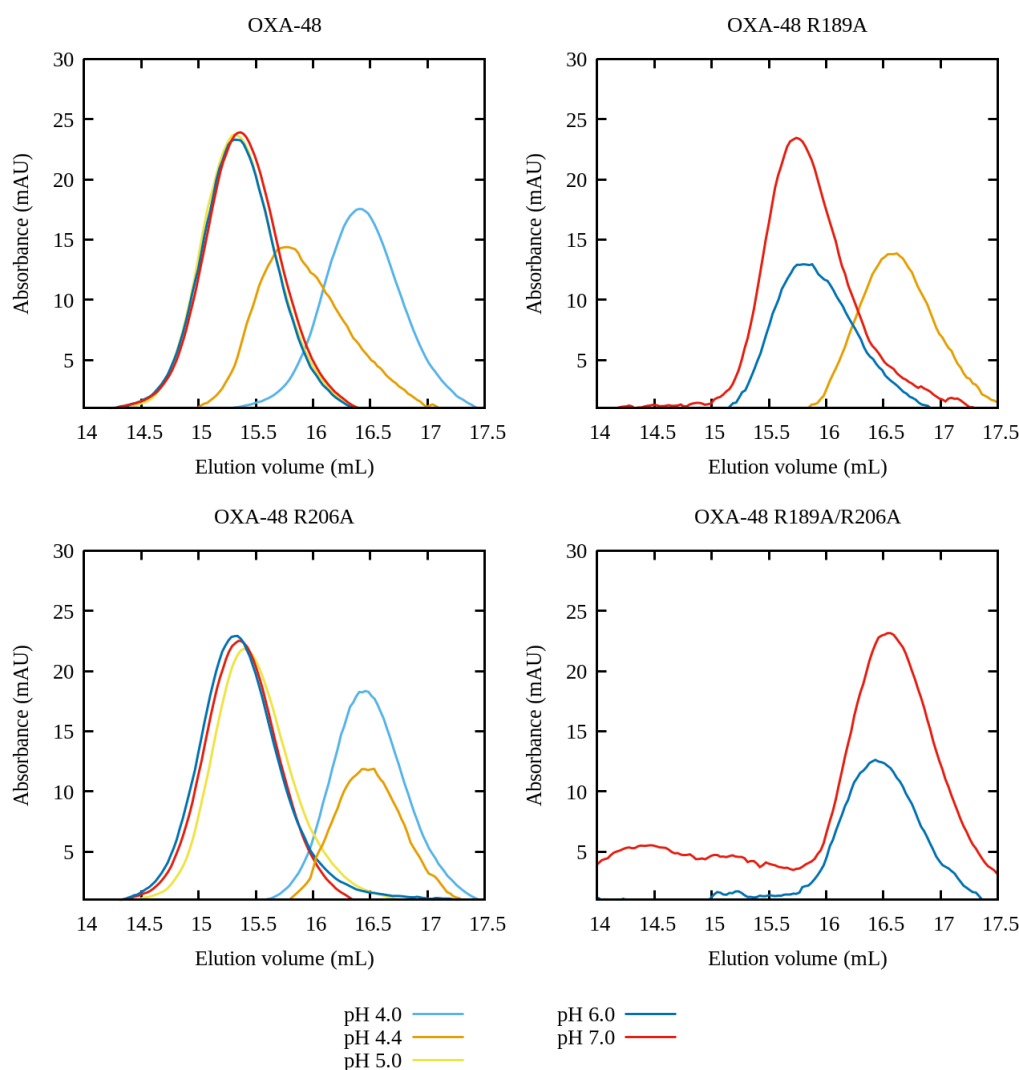
Figure 3-29: Chromatogram from size-exclusion chromatography with Superdex 200 10/300 GL, showing elution volumes for OXA-48, and OXA-48 R206A, R189A and R189A/R206A using phosphate citrate buffer with 50 mM potassium sulphate at different pH. The elution peaks for the proteins are indicated by color; pH 4.0 – light blue, pH 4.4 – orange, pH 5.0 – yellow, pH 6.0 – blue, pH 7.0 – red. Figure by Dr. Bjarte A. Lund (unpublished data).

From the dimer affinity and thermal stability experiments it is clear that the mutants affecting the dimer interface destabilizes the dimer, compared to the wild type OXA-48. And it seems OXA-48 R206A and R189A effect the dimer to a lesser extent compared to the double mutant OXA-48 R189A/R206A. However, it is not quite clear from the methods used if R189A/R206A is predominantly in the monomeric form. Based on the DSC experiments, comparing the enthalpy values from the measurement and the fitted two-state model it seems that assuming a dimer yields the best results. The MST experiments indicate a reduced dimer association for OXA-48 R189A/R206A (K_d 22 nM), through an increased dissociation constant compared to OXA-48 R206A. But the determined K_d value is still quite low compared to the reported values for other OXA-dimers, indicating that R189A/R206A still has a quite strong

dimer association. While DSC and MST experiments suggest dimer formation for OXA-48 R189A/R206A, the gel filtration (SEC) elutes the protein at a volume consistent with monomer formation at neutral pH.

As it is puzzling that the different methods applied to study the dimer interface mutants does not seem to yield the same results, it is perhaps not surprisingly. The different techniques use different methods to analyze the protein, not to mention that different buffers were used for all the techniques; 50 mM HEPES pH 7.0, 50 mM K_2SO_4/ 50 mM phosphate buffer pH 7.2 for DSC, 50 mM HEPES pH 7.0, 50 mM K_2SO_4, 0.05% Tween-20 for MST, and citrate-phosphate buffer with 50 mM K_2SO_4 for SEC. DSC measures the thermal stability, or the heat capacity difference between the denatured and native protein sample. SEC measures the absorbance (OD_{280}) of the proteins eluting from the size-exclusion column, after interacting with the gel column material. The differently charged mutants could then interact slightly different with the column material. MST measures the movement of molecules in a thermal gradient, using fluorescence to detect the florescent tagged protein.

Taken together it is only possible to conclude that the OXA-48 dimer interface mutations has shifted the monomer:dimer equilibrium towards monomer formation, thus destabilizing the dimer observed through lower melting temperatures, lower dissociation constant, and altered elution volumes using the same pH gradient in SEC experiments.

3.4 Enzyme activity

To study the enzyme activity, effects from different mutations, steady state enzyme kinetic assays were performed. The substrates nitrocefin, ampicillin, imipenem, and ceftazidime were investigated at different concentrations with a selection of the OXA-48 mutants. The substrate concentrations used for the different kinetic measurements are listed in Table 3-5. The final steady-state enzyme kinetic parameters are listed in Table 3-6. Enzyme kinetic curves for the OXA-48 mutants compared to OXA-48 with different substrates are shown in Figure 3-31. The individual Michaelis-Menten curves are suppled in Appendix Figure A2-A5.

Table 3-5: Concentration-range used for the different substrates; nitrocefin, ampicillin, imipenem, and ceftazidime, when measuring the enzyme activity for OXA-48 and the prepared OXA-48 mutants.

	Nitrocefin	Ampicillin	Imipenem	Ceftazidime
OXA-48	3.4-300 μM	60-1000 μM	1.2-150 μM	11-400 μM
S70A	94-750 μM	NH[a]	ND[b]	ND[b]
S70T	16-2000 μM	NH[a]	210-1000 μM	ND[b]
S70T/T71S	12-1500 μM	NH[a]	210-1000 μM	ND[b]
P68A	3.4-300 μM	45-750 μM	1.2-150 μM	9-320 μM
P68A/Y211S	3.4-300 μM	45-750 μM	1.2-150 μM	9-320 μM
R189A	6.8-750 μM	ND[b]	ND[b]	ND[b]
R189A/R206A	6.8-750 μM	ND[b]	ND[b]	ND[b]

[a]NH, no detectable hydrolysis

[b]ND, not determined

Table 3-6: Steady-state enzyme kinetic parameters for OXA-48 and prepared mutants with nitrocefin, ampicillin, imipenem and cephalosporin. Standard errors are given.

Substrate	Enzyme	K_m (μM)	k_{cat} (s^{-1})	k_{cat}/K_m ($\mu M^{-1}s^{-1}$)	(k_{cat}/K_m mut.)/ (k_{cat}/K_m OXA-48)
Nitrocefin (reporter substrate)	OXA-48	31 ± 4	1260 ± 50	40	
	S70A	90 ± 40	3.4 ± 0.4	0.04	
	S70T	2260 ± 420	285 ± 33	0.1	0.003
	S70T/T71S	640 ± 80	47 ± 3	0.07	0.002
	P68A	32 ± 4	286 ± 11	9	0.2
	P68A/Y211S	39 ± 6	62 ± 3	2	0.04
	R189A	122 ± 21	1950 ± 130	16	0.4
	R189A/R206A	120 ± 20	1550 ± 80	13	0.3
Ampicillin (penicillin)	OXA-48	370 ± 70	1600 ± 140	4	
	S70T	NH[a]	ND[b]	ND[b]	-
	S70T/T71S	NH[a]	ND[b]	ND[b]	-
	P68A	77 ± 12	67 ± 3	0.9	0.2
	P68A/Y211S	211 ± 26	48 ± 2	0.2	0.05
Imipenem (carbapenem)	OXA-48	13 ± 2	12.5 ± 0.5	1	
	S70T	2770 ± 850	58 ± 14	0.02	0.02
	S70T/T71S	1180 ± 450	27 ± 8	0.02	0.02
	P68A	4.2 ± 0.9	2.1 ± 0.1	0.5	0.5
	P68A/Y211S	14 ± 3	1.50 ± 0.09	0.1	0.1
Ceftazidime (cephalosporin)	OXA-48	300 ± 150	8 ± 2	0.03	
	P68A	220 ± 50	68 ± 8	0.3	11
	P68A/Y211S	190 ± 40	110 ± 13	0.6	21

[a]NH, no detectible hydrolysis

[b]ND, not determined

3.4.1 Enzyme activity of OXA-48 mutants affecting the dimer interface

The hydrolytic activity of the OXA-48 mutants R189A and R189A/R206A were studied against nitrocefin to investigate how the potential monomer formation could affect the enzyme activity. Even if it was hard to determine with certainty if OXA-48 R189A/R206A is a monomer, the monomer:dimer equilibrium is most likely shifted towards monomer formation at ~1 nM the enzyme concentrations used during the enzyme assays. This is since the dimer dissociation constant (K_d) was measured to 22 nM by MST. If a monomer had significantly lower activity than a dimer, this should be detectable by enzyme activity measurements. The steady-state enzyme kinetic parameters for OXA-48 and OXA-48 mutants are listed in Table 3-6, and the enzyme kinetic curves are shown in Figure 3-32 G. Here, the enzyme kinetic results showed that OXA-48 displayed only 2 times higher activity than R189A, and approximately 3 times higher activity than R189A/R206A (Table 3-6). Previous enzyme kinetic experiments of OXA-48 and OXA-48 R206A (conducted by Dr. Bjarte A. Lund) showed that the two enzymes possessed almost the same degree of enzyme activity.

In summary, this suggests that the OXA-48 mutants R206A, R189A, and R189A/R206A affect the dimer affinity and thermal stability, but have little effect on the enzyme activity. Based on these observations, OXA-48 R189A and R189A/R206A were not prioritized for further enzyme activity testing.

3.4.2 Enzyme activity of the OXA-48 active site mutants S70A, S70T and S70T/T71S

OXA-48 S70A was designed as an inactive mutant for comparison of the other mutants and OXA-48. However, at a specific concentration range of nitrocefin it was possible to detect a very low activity (k_{cat}/K_m 0.04 $\mu M^{-1}s^{-1}$). S70A was also tested with ampicillin, but no enzyme activity was detected.

OXA-48 S70T and S70T/T71S displayed almost no hydrolytic activity against nitrocefin and imipenem, as can be seen from the enzyme kinetic curves (Figure 3-32 A and E) and determined K_m values (Table 3-6), the substrate specificity was very low. During the kinetics experiment the substrate concentrations were increased to the detection limit (high OD). However, it was still not possible to detect substrate saturation of the enzymes. Enzyme activity experiments with similar active site mutants were reported for TEM (class A β-lactamase) S70T and T71S in the 1980s [63, 64]. They reported no detectable hydrolysis for the S70T mutant, but only a slightly decreased activity for the T71S mutant, and with a much

lower thermal stability compared to the wild type [64]. A different study reported low but detectable activity for a TEM S70C mutant [65].

A low activity was detectable for both OXA-48 S70T and S70T/T71S with nitrocefin and imipenem, but no hydrolysis could be detected with ampicillin. This is shown in the steady-state enzyme kinetics in Table 3-6, and the enzyme kinetic curves in Figure 3-32 A and E. It can be speculated that the additional methyl group in S70T introduced to the active site by the mutation add a steric strain, and prevent the hydroxyl nucleophilic attach from occurring. This could then explain the drastically lowering of the enzyme activity, mainly by reducing the ability to covalently bind to the substrates. It was hypothesized that the double mutation S70T/T71S could compensate for the steric strain of the extra methyl-group introduced for the active site nucleophilic residue S70, by removing one methyl-group from T71. However, a slightly lower activity was actually detected for the double mutant with the substrate nitrocefin, compared to the S70T mutant (Table 3-6). In a study by Stojanoski et al. [110] the S70 residue was substituted by a glycine in a number of serine β-lactamases, including OXA-48. The overall results showed an increased thermal stability for the S70G mutants (no hydrolytic activity). This supports the stability-function hypothesis; stating that active-site residues are optimized for substrate binding and catalysis, which often is not consistent with the requirements for optimal stability [110]. These findings might support our hypothesis that the highly decreased enzyme activity observed for the OXA-48 S70T and S70T/T71S mutants is mainly due to an even further increased steric strain in the active site, and reduced optimal orientation of the active site residues.

In the crystal structure of OXA-48 in complex with imipenem (PDB: 5QB4), by Dr. Bjarte A. Lund, a covalent bond between Ser70 and the carbonyl carbon of the β-lactam ring of imipenem was observed. It is possible that the correct orientation of the substrate and the hydroxyl-group of residue 70 is affected by addition of the methyl group of threonine. Thr71 does not seem to be directly involved in the reaction mechanism of class D β-lactamases, but is a conserved active site residue. The hydroxyl-group of Thr71 forms hydrogen bonds with nearby residues (main chain of Pro68, and sidechain of Gln169), and herein the methyl-group seem important for the sidechain orientation (Figure 3-30). So, by introducing the double mutant we not only disturb the orientation of the active site nucleophile, but also the interaction of residue 71, potentially lowering the enzyme stability as well as the activity.
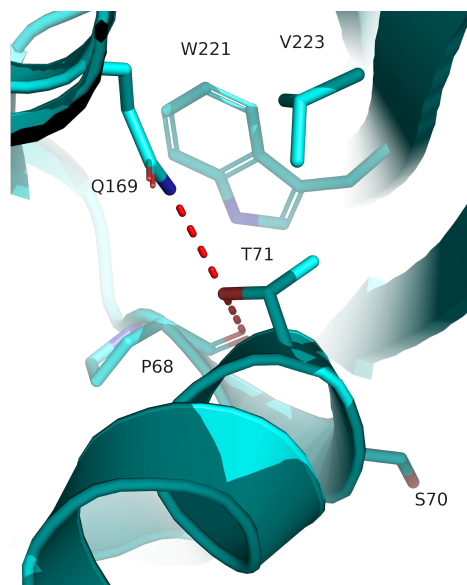
Figure 3-30: Crystal structure of OXA-48 (PDB: 5QB4) showing the interactions of the hydroxyl group of Thr71 to the residues Pro68 and Gln169. The methyl group of Thr71 seem important for the side-chain orientation. Ser70 is also shown residing on the same α-helix as Thr71. Figure made in PyMOL in collaboration with researcher Hanna-Kirsti S. Leiros.

3.4.3   Enzyme activity of OXA-48 mutants introducing ceftazidime activity

OXA-48 P68A and P68A/Y211S showed reduced enzyme activity compared to the wild type OXA-48 for the substrates nitrocefin, imipenem and ampicillin. P68A displayed the highest enzyme activity of the two mutants, with 2-5 times lower activity than OXA-48. P68A/Y211S had a 10-20 times lower activity than OXA-48 respectively. Differently with the substrate ceftazidime, P68A showed an approximately 10 fold increase in activity, and P68A/Y211S 20 fold increase, compared to the wild type OXA-48. The steady-state enzyme kinetic parameters are listed in Table 3-6, and enzyme kinetics curves are shown in Figure 3-32 B, C, D and F.

Residue Pro68 is found at the beginning of the α3-helix in OXA-48, where Ser70 is located (Figure 3-30). Proline makes the structure more rigid, and the introduction of alanine will most likely increase the flexibility and affect the helix orientation. This may reduce the activity of the mutant, as Ser70 may not occupy an ideal conformation for hydrolysis of nitrocefin, ampicillin and imipenem. However, both the R1 and R2 sidechains of ceftazidime are bulkier than the sidechains of other substrates. Hence the more flexible helix and location of Ser70 in the P68A and P68A/Y211S mutants may better accommodate the binding of such a large substrate. The molecular structure of ceftazidime is shown in Figure 3-31. Figure 1-9 shows the binding of imipenem in the active site of OXA-48 for comparison.
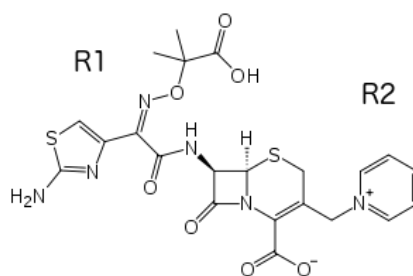
Figure 3-31: Molecular structure of ceftazidime, showing the bulky side-groups R1 and R2. Figure from Wikipedia.

OXA-48 P68A/Y211S probably increases the accessibility of the active site even further by substituting tyrosine with the smaller serine. This may make binding and hydrolysis of ceftazidime easier, but reduces its ability to bind smaller substrates accurately in the active site.

The measured activity of OXA-48 wild type with ceftazidime was at first surprisingly high, with a k_{cat}/K_m value of 0.03 $\mu M^{-1}s^{-1}$ (Table 3-6). Kinetic parameters for OXA-48 with ceftazidime was by Docquier et al. [46] reported to be inactive (2009), Poirel et al. [50] reported a very low activity of 0.001 $\mu M^{-1}s^{-1}$ (2004). However, both studies measured the kinetic data in the absence of a carbonate (CO_3^{2-}) source. Docquier et al. conducted their kinetic measurements in 100 mM Tris-H_2SO_4 pH 7.0, 300 mM K_2SO_4 buffer, and Poirel et al. used 100 mM sodium-phosphate pH 7.0 buffer. It has been shown that the presence of a carbonate source is highly important for reliable and reproducible enzyme kinetic results for the class D β-lactamases, to allow for carboxylation of Lys73. Kinetic data obtained with a CO_2 source, can therefore not be meaningfully compared to data obtained without a CO_2 source [24]. The higher enzyme activity of OXA-48 with ceftazidime reported here, compared to previously reported kinetic parameters, can therefore most likely be explained by the lack of a carbonate source in the previous enzyme assays.

Chloride inhibition has long been a distinct feature in the field of the class D β-lactamases [37]. Later it turned out that the presence of chloride does only display an inhibitory effect in the absence of a carbonate source, thus when Lys73 is not carboxylated. Our DSC experiments of OXA-48 like enzymes with two different buffers (with and without PO_4^{3-}/ K_2SO_4) suggest that the presence of sulphate ions destabilizes the dimer, and reduces the thermal stability of the enzyme. This is an interesting observation as many previous kinetic experiments concerning OXA-enzymes used K_2SO_4, since Cl^- was thought to be an inhibitor. The presence of K_2SO_4 in addition to the absence of a carbonate source might contribute to further lower the enzyme activity.
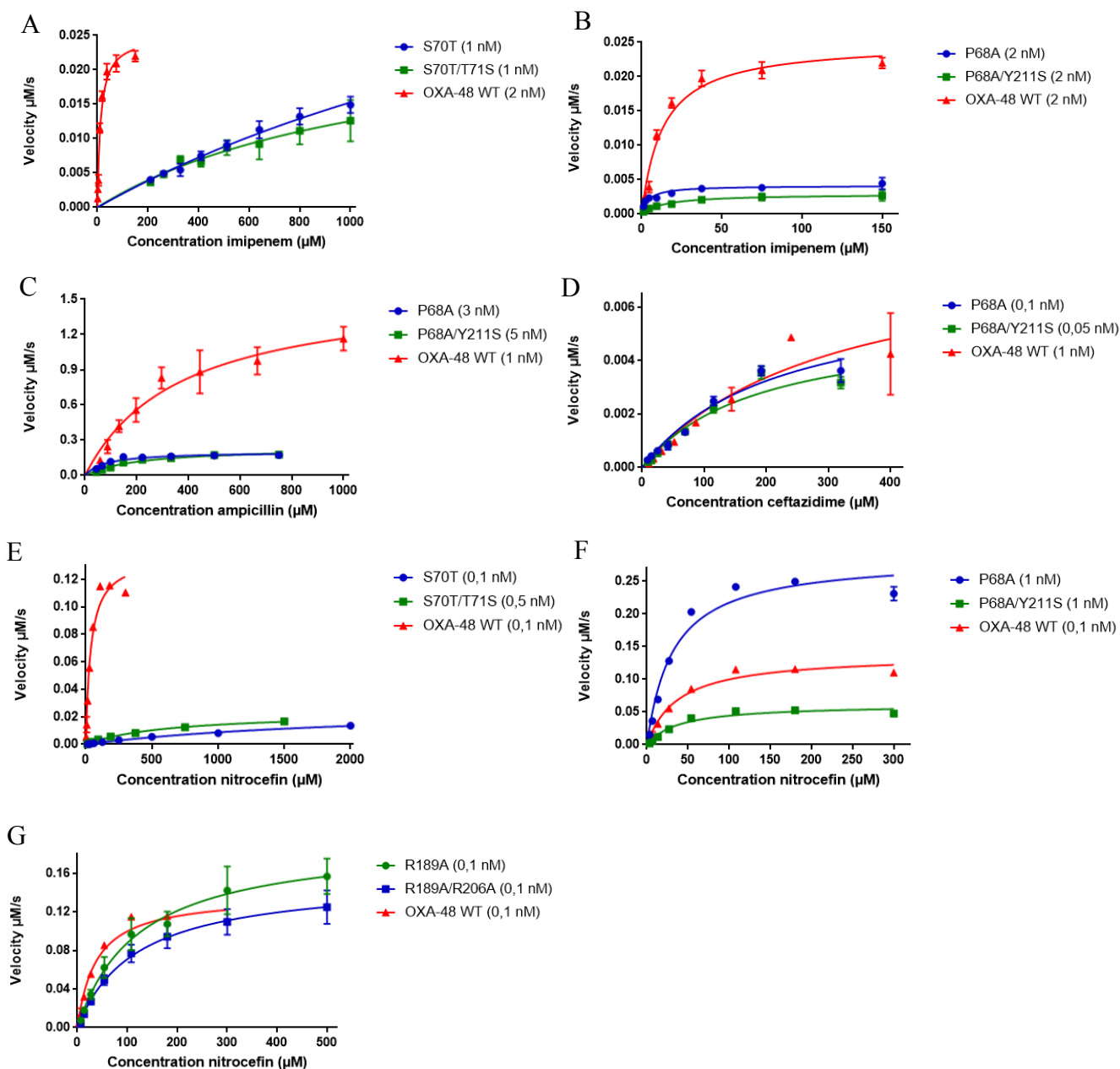
Figure 3-32: Enzyme kinetics curves comparing OXA-48 to the OXA-48 mutants S70A, S70T, S70T/T71S, P68A, P68A/Y211S, R189A and R189A/R206A with different substrates. The substrate concentrations are given along the x-axis, while the reaction velocity is given along the y-axis. The enzyme concentrations used in the assays are listed. OXA-48 is labelled OXA-48 WT. **A)** Imipenem with 1 nM S70T (blue), 1 nM S70T/T71S (green), and 2 nM OXA-48 (red). **B)** Imipenem with 2 nM P68A (blue), 2 nM P68A/Y211S (green), and 2 nM OXA-48 (red). **C)** Ampicillin with 3 nM P68A (blue), 5 nM P68A/Y211S (green), and 1 nM OXA-48 (red). **D)** Ceftazidime with 0.1 nM P68A (blue), 0.05 nM P68A/Y211S (green), and 1 nM OXA-48 (red). **E)** Nitrocefin with 0.1 nM S70T (blue), 0.5 nM S70T/T71S (green), and 0.1 nM OXA-48 (red). **F)** Nitrocefin with 1 nM P68A (blue), 1 nM P68A/Y211S (green), and 0.1 nM OXA-48 (red). **G)** Nitrocefin with 0.1 nM R189A (blue), 0.1 nM R189A/R206A (green), and 0.1 nM OXA-48 (red).

101

4   Conclusion

The *bla*_{OXA-48} gene, with the signal peptide removed and an inserted N-terminal hexa-histidine tag and TEV cleavage site were used as a template to create OXA-48 mutants affecting the active site and dimer interface. The mutants OXA-48 S70A, S70T, S70T/T71S, R189A, R189A/R206A, P68A, and P68A/Y211S were designed, produced and sequence analysed. In addition to the mutants, OXA-163 and OXA-48 were also expressed and purified. The highest yield of pure protein was obtained when purifying OXA-163, likely related to OXA-163 being a synthetic DNA gene that was codon optimized for *E. coli*. Still sufficient amounts of protein were obtained for OXA-48 and its mutants.

The crystal structures for OXA-48 S70A, S70T, S70T/T71S and R189A were determined, displaying that residue substitutions did not alter the overall conformation. The first crystal structures of OXA-181 and the novel β-lactamase OXA-436 were also obtained, as well as the structure of a new crystal form of OXA-163.

Differential scanning calorimetry was used to investigate the thermal stability of OXA-48, OXA-181, OXA-163, OXA-245, OXA-436 and the OXA-48 mutants R206A, R189A, and R189A/R206A, using two different buffer systems. Taken together, these studies suggest that the addition of sulphate in OXA-buffers reduces the thermal stability, possibly caused by the binding of a sulphate ion by residue R206 instead of a chloride ion, destabilizing the dimer. The DSC analysis were also used to investigate the differences between selected OXA-48 like enzymes, as well as determine the destabilizing effect of the dimer interface mutations, suggesting that the dimer formation is important for the thermal stability. These results together with the structural data were used to investigate the structure and thermostability relationship between OXA-181, OXA-163 and OXA-245 in the article "Structure activity and thermostability investigations of OXA-163, OXA-181 and OXA-245, using biochemical, crystal structures and differential scanning calorimetry analysis".

Based on previous dimer affinity investigations, size-exclusion chromatography and microscale thermophoresis were used to inspect the dimer affinity further for OXA-48, and OXA-48 mutants affecting the dimer interface. From the MST analysis, the dissociation constant for OXA-48 R189A/R206A were determined to 22 nM, which taken together with previous MST results suggests that the OXA-48 dimer affinity is very strong. The strong dimer affinity was considered to be further confirmed by size-exclusion chromatography, which indicated monomer formation of OXA-48 only at pH 4.0. However, monomer formation was indicated for OXA-48 R189A/R206A at neutral pH. This suggest that salt-bridges are highly

important for stability of the OXA-48 dimer. The deviating results may be explained by the different methods employed.

Enzyme activity investigations for OXA-48 and a selection of the OXA-48 mutants were conducted with the substrates nitrocefin, ampicillin, imipenem and ceftazidime. This showed almost no activity for the active site mutants S70T and S70T/T71S, with S70T/T71S having the lowest activity of the two. The mutants affecting the dimer interface, namely R189A and R189A/R206A, showed only a slightly reduced enzyme activity, with OXA-48 having 2 times higher catalytic activity. The active site mutants P68A and P68A/Y211S, discovered by evolutionary studies selecting for ceftazidime resistance, did hydrolyse ceftazidime at a higher rate than OXA-48. P68A showed a 10 fold increase in catalytic activity, and P68A/Y211S a 20 fold increase, compared to OXA-48. However, this seemed to come at a cost of reduced hydrolytic activity for other substrates, compared to OXA-48.

To conclude, the reported results suggest that the strong dimer affinity for OXA-48 is dependent on salt-bridges for its formation. It appears that destabilizing the dimer does not affect the enzyme activity significantly, but is important for the thermal stability. Substituting residues in the active site greatly affect the enzyme activity, possible by increasing the steric strain in the active site, and affect the optimal residue orientation. The suspected increased flexibility in the active site for P68A and P68A/Y211S mutants may allow for the hydrolysis of larger substrates, but reduces the ability to hydrolyse substrates to which OXA-48 displays activity.

5   Future Work

Crystal structures were not obtained for the OXA-48 mutants P68A/Y211S and R189A/R206A, and this would be a natural next step in studying the structural details of the mutants. It would be especially interesting to study the binding of different substrates by the active site mutants P68A and P68A/Y211S. At a very late phase of this thesis, the crystal structure of OXA-48 P68A binding ceftazidime was obtained by PhD. student Christopher Fröhlich.

Even though the OXA-48 R189A, R206A and R189A/R206A mutants affecting the dimer interface did not display a significantly reduced enzyme activity with the substrate nitrocefin compared to OXA-48, the enzymes could be measured towards additional β-lactam classes. The aim could be to determine if the relatively similar activity to OXA-48 for mutants with different thermal stability, is a general effect, or if the amino acid substitutions could affect the hydrolysis of certain, but not all substrates.

Further, the thermal stability of the active site mutants S70T and S70T/T71S could be analysed. It was suspected that the amino acid substitutions S70T/T71S increased the steric strain of the active site, and potentially could destabilize the structure. This could be an important step in elucidating the function of the highly conserved residue Thr71.

There is a need for further studies to determine the complete reaction mechanism for class D β-lactamases. Mutational studies involving multiple active sites residues, such as Val119, Lys208 and Ser118 may be especially useful.

References

1. Blair, J.M., M.A. Webber, A.J. Baylay, D.O. Ogbolu, and L.J. Piddock, *Molecular mechanisms of antibiotic resistance.* Nat Rev Microbiol, 2015. **13**(1): p. 42-51.
2. Lin, J., K. Nishino, M.C. Roberts, M. Tolmasky, R.I. Aminov, and L. Zhang, *Mechanisms of antibiotic resistance.* Frontiers in Microbiology, 2015. **6**: p. 34.
3. O´Neill, J., *Tackeling Drug-Resistant Infections Globally: Final Report and Recommendations*. 2016.
4. World Economic Forum, *The Global Risks Report 2018*. 2018.
5. WHO, *Antimicrobial resistance: Global report on surveillance.* 2014.
6. Rodríguez-Rojas, A., J. Rodríguez-Beltrán, A. Couce, and J. Blázquez, *Antibiotics and antibiotic resistance: A bitter fight against evolution.* International Journal of Medical Microbiology, 2013. **303**(6): p. 293-297.
7. King, D.T., S. Sobhanifar, and N.C.J. Strynadka, *The Mechanisms of Resistance to β-Lactam Antibiotics*, in *Handbook of Antimicrobial Resistance*, A. Berghuis, et al., Editors. 2017, Springer New York: New York, NY. p. 177-201.
8. Hall, B.G. and M. Barlow, *Evolution of the serine beta-lactamases: past, present and future.* Drug Resist Updat, 2004. **7**(2): p. 111-23.
9. Laxminarayan, R., A. Duse, C. Wattal, A.K. Zaidi, H.F. Wertheim, N. Sumpradit, E. Vlieghe, G.L. Hara, I.M. Gould, H. Goossens, C. Greko, A.D. So, M. Bigdeli, G. Tomson, W. Woodhouse, E. Ombaka, A.Q. Peralta, F.N. Qamar, F. Mir, S. Kariuki, Z.A. Bhutta, A. Coates, R. Bergstrom, G.D. Wright, E.D. Brown, and O. Cars, *Antibiotic resistance-the need for global solutions.* Lancet Infect Dis, 2013. **13**(12): p. 1057-98.
10. Wise, E.M. and J.T. Park, *Penicillin: its basic site of action as an inhibitor of a peptide cross-linking reaction in cell wall mucopeptide synthesis.* Proceedings of the National Academy of Sciences of the United States of America, 1965. **54**(1): p. 75-81.
11. Miller, E.L., *The penicillins: a review and update.* J Midwifery Womens Health, 2002. **47**(6): p. 426-34.
12. Stapley, E.O., M. Jackson, S. Hernandez, S.B. Zimmerman, S.A. Currie, S. Mochales, J.M. Mata, H.B. Woodruff, and D. Hendlin, *Cephamycins, a new family of beta-lactam antibiotics. I. Production by actinomycetes, including Streptomyces lactamdurans sp. n.* Antimicrob Agents Chemother, 1972. **2**(3): p. 122-31.
13. Calderwood, S. and A. Letourneau. *Cephalosporins* 2018 15.03.2018]; Available from: https://www.uptodate.com/contents/cephalosporins.
14. Sykes, R.B., D.P. Bonner, K. Bush, and N.H. Georgopapadakou, *Azthreonam (SQ 26,776), a synthetic monobactam specifically active against aerobic gram-negative bacteria.* Antimicrob Agents Chemother, 1982. **21**(1): p. 85-92.
15. Birnbaum, J., F.M. Kahan, H. Kropp, and J.S. MacDonald, *Carbapenems, a new class of beta-lactam antibiotics. Discovery and development of imipenem/cilastatin.* Am J Med, 1985. **78**(6a): p. 3-21.
16. Papp-Wallace, K.M., A. Endimiani, M.A. Taracila, and R.A. Bonomo, *Carbapenems: past, present, and future.* Antimicrob Agents Chemother, 2011. **55**(11): p. 4943-60.
17. Toth, M., C.A. Smith, N.T. Antunes, N.K. Stewart, L. Maltz, and S.B. Vakulenko, *The role of conserved surface hydrophobic residues in the carbapenemase activity of the class D beta-lactamases.* Acta Crystallogr D Struct Biol, 2017. **73**(Pt 8): p. 692-701.
18. Stewart, N.K., C.A. Smith, H. Frase, D.J. Black, and S.B. Vakulenko, *Kinetic and Structural Requirements for Carbapenemase Activity in GES-Type β-Lactamases.* Biochemistry, 2015. **54**(2): p. 588-597.

19.   Naas, T., S. Oueslati, R.A. Bonnin, M.L. Dabos, A. Zavala, L. Dortet, P. Retailleau, and B.I. Iorga, *Beta-lactamase database (BLDB) – structure and function.* Journal of Enzyme Inhibition and Medicinal Chemistry, 2017. **32**(1): p. 917-919.

20.   Bush, K., G.A. Jacoby, and A.A. Medeiros, *A functional classification scheme for beta-lactamases and its correlation with molecular structure.* Antimicrob Agents Chemother, 1995. **39**(6): p. 1211-33.

21.   Bush, K. and G.A. Jacoby, *Updated functional classification of beta-lactamases.* Antimicrob Agents Chemother, 2010. **54**(3): p. 969-76.

22.   Ambler, R.P., *The structure of beta-lactamases.* Philos Trans R Soc Lond B Biol Sci, 1980. **289**(1036): p. 321-31.

23.   Poirel, L., T. Naas, and P. Nordmann, *Diversity, epidemiology, and genetics of class D beta-lactamases.* Antimicrob Agents Chemother, 2010. **54**(1): p. 24-38.

24.   Antunes, N.T. and J.F. Fisher, *Acquired Class D β-Lactamases.* Antibiotics, 2014. **3**(3): p. 398-434.

25.   WHO, *Global priority list of antibiotic-resistant bacteria to guide research, discovery, and development of new antibiotics* E. Tacconelli and N. Magrini, Editors. 2017.

26.   Leonard, D.A., R.A. Bonomo, and R.A. Powers, *Class D β-Lactamases: A Reappraisal after Five Decades.* Accounts of Chemical Research, 2013. **46**(11): p. 2407-2415.

27.   Schneider, K.D., C.R. Bethel, A.M. Distler, A.M. Hujer, R.A. Bonomo, and D.A. Leonard, *Mutation of the Active Site Carboxy-Lysine (K70) of OXA-1 β-Lactamase Results in a Deacylation-Deficient Enzyme.* Biochemistry, 2009. **48**(26): p. 6136-6145.

28.   Walther-Rasmussen, J. and N. Hoiby, *OXA-type carbapenemases.* J Antimicrob Chemother, 2006. **57**(3): p. 373-83.

29.   Verma, V., S.A. Testero, K. Amini, W. Wei, J. Liu, N. Balachandran, T. Monoharan, S. Stynes, L.P. Kotra, and D. Golemi-Kotra, *Hydrolytic mechanism of OXA-58 enzyme, a carbapenem-hydrolyzing class D beta-lactamase from Acinetobacter baumannii.* J Biol Chem, 2011. **286**(43): p. 37292-303.

30.   Maveyraud, L., D. Golemi-Kotra, A. Ishiwata, O. Meroueh, S. Mobashery, and J.-P. Samama, *High-Resolution X-ray Structure of an Acyl-Enzyme Species for the Class D OXA-10 β-Lactamase.* Journal of the American Chemical Society, 2002. **124**(11): p. 2461-2465.

31.   Li, J., J.B. Cross, T. Vreven, S.O. Meroueh, S. Mobashery, and H.B. Schlegel, *Lysine carboxylation in proteins: OXA-10 beta-lactamase.* Proteins, 2005. **61**(2): p. 246-57.

32.   Isom, D.G., C.A. Castaneda, B.R. Cannon, and B. Garcia-Moreno, *Large shifts in pKa values of lysine residues buried inside a protein.* Proc Natl Acad Sci U S A, 2011. **108**(13): p. 5260-5.

33.   Sun, T., M. Nukaga, K. Mayama, E.H. Braswell, and J.R. Knox, *Comparison of beta-lactamases of classes A and D: 1.5-A crystallographic structure of the class D OXA-1 oxacillinase.* Protein Sci, 2003. **12**(1): p. 82-91.

34.   Paetzel, M., F. Danel, L. de Castro, S.C. Mosimann, M.G. Page, and N.C. Strynadka, *Crystal structure of the class D beta-lactamase OXA-10.* Nat Struct Biol, 2000. **7**(10): p. 918-25.

35.   Golemi, D., L. Maveyraud, S. Vakulenko, J.P. Samama, and S. Mobashery, *Critical involvement of a carbamylated lysine in catalytic function of class D beta-lactamases.* Proc Natl Acad Sci U S A, 2001. **98**(25): p. 14280-5.

36.   Baurin, S., L. Vercheval, F. Bouillenne, C. Falzone, A. Brans, L. Jacquamet, J.L. Ferrer, E. Sauvage, D. Dehareng, J.M. Frere, P. Charlier, M. Galleni, and F. Kerff, *Critical role of tryptophan 154 for the activity and stability of class D beta-lactamases.* Biochemistry, 2009. **48**(47): p. 11252-63.

37. Vercheval, L., C. Bauvois, A. di Paolo, F. Borel, J.L. Ferrer, E. Sauvage, A. Matagne, J.M. Frere, P. Charlier, M. Galleni, and F. Kerff, *Three factors that modulate the activity of class D beta-lactamases and interfere with the post-translational carboxylation of Lys70.* Biochem J, 2010. **432**(3): p. 495-504.

38. Escobar, W.A., A.K. Tan, and A.L. Fink, *Site-directed mutagenesis of .beta.-lactamase leading to accumulation of a catalytic intermediate.* Biochemistry, 1991. **30**(44): p. 10783-10787.

39. Lund, B.A., T. Christopeit, Y. Guttormsen, A. Bayer, and H.K. Leiros, *Screening and Design of Inhibitor Scaffolds for the Antibiotic Resistance Oxacillinase-48 (OXA-48) through Surface Plasmon Resonance Screening.* J Med Chem, 2016. **59**(11): p. 5542-54.

40. Sharma, S. and P. Bandyopadhyay, *Investigation of the acylation mechanism of class C beta-lactamase: pKa calculation, molecular dynamics simulation and quantum mechanical calculation.* J Mol Model, 2012. **18**(2): p. 481-92.

41. Sgrignani, J., G. Grazioso, and M. De Amici, *Insight into the Mechanism of Hydrolysis of Meropenem by OXA-23 Serine-beta-lactamase Gained by Quantum Mechanics/Molecular Mechanics Calculations.* Biochemistry, 2016. **55**(36): p. 5191-200.

42. Queenan, A.M. and K. Bush, *Carbapenemases: the versatile beta-lactamases.* Clin Microbiol Rev, 2007. **20**(3): p. 440-58, table of contents.

43. Nordmann, P., T. Naas, and L. Poirel, *Global spread of Carbapenemase-producing Enterobacteriaceae.* Emerg Infect Dis, 2011. **17**(10): p. 1791-8.

44. Pitout, J.D. and K.B. Laupland, *Extended-spectrum beta-lactamase-producing Enterobacteriaceae: an emerging public-health concern.* Lancet Infect Dis, 2008. **8**(3): p. 159-66.

45. Antunes, N.T., T.L. Lamoureaux, M. Toth, N.K. Stewart, H. Frase, and S.B. Vakulenko, *Class D beta-lactamases: are they all carbapenemases?* Antimicrob Agents Chemother, 2014. **58**(4): p. 2119-25.

46. Docquier, J.-D., V. Calderone, F. De Luca, M. Benvenuti, F. Giuliani, L. Bellucci, A. Tafi, P. Nordmann, M. Botta, G.M. Rossolini, and S. Mangani, *Crystal structure of the OXA-48 beta-lactamase reveals mechanistic diversity among class D carbapenemases.* Chem Biol, 2009. **16**(5): p. 540-7.

47. Santillana, E., A. Beceiro, G. Bou, and A. Romero, *Crystal structure of the carbapenemase OXA-24 reveals insights into the mechanism of carbapenem hydrolysis.* Proceedings of the National Academy of Sciences of the United States of America, 2007. **104**(13): p. 5354-5359.

48. Schneider, K.D., C.J. Ortega, N.A. Renck, R.A. Bonomo, R.A. Powers, and D.A. Leonard, *STRUCTURES OF THE CLASS D CARBAPENEMASE OXA-24 FROM ACINETOBACTER BAUMANNII IN COMPLEX WITH DORIPENEM.* Journal of molecular biology, 2011. **406**(4): p. 583-594.

49. Lohans, C.T., E. van Groesen, K. Kumar, C.L. Tooke, J. Spencer, R.S. Paton, J. Brem, and C.J. Schofield, *A New Mechanism for β-Lactamases: Class D Enzymes Degrade 1β-Methyl Carbapenems through Lactone Formation.* Angewandte Chemie (International Ed. in English), 2018. **57**(5): p. 1282-1285.

50. Poirel, L., C. Heritier, V. Tolun, and P. Nordmann, *Emergence of oxacillinase-mediated resistance to imipenem in Klebsiella pneumoniae.* Antimicrob Agents Chemother, 2004. **48**(1): p. 15-22.

51. Poirel, L., A. Potron, and P. Nordmann, *OXA-48-like carbapenemases: the phantom menace.* J Antimicrob Chemother, 2012. **67**(7): p. 1597-606.

52. Oueslati, S., P. Nordmann, and L. Poirel, *Heterogeneous hydrolytic features for OXA-48-like beta-lactamases.* J Antimicrob Chemother, 2015. **70**(4): p. 1059-63.

53. Poirel, L., M. Castanheira, A. Carrer, C.P. Rodriguez, R.N. Jones, J. Smayevsky, and P. Nordmann, *OXA-163, an OXA-48-related class D beta-lactamase with extended activity toward expanded-spectrum cephalosporins.* Antimicrob Agents Chemother, 2011. **55**(6): p. 2546-51.

54. Lund, B.A., A.M. Thomassen, T.J.O. Carlsen, and H.K.S. Leiros, *Structure, activity and thermostability investigations of OXA-163, OXA-181 and OXA-245 using biochemical analysis, crystal structures and differential scanning calorimetry analysis.* Acta Crystallogr F Struct Biol Commun, 2017. **73**(Pt 10): p. 579-587.

55. Samuelsen, O., F. Hansen, B. Aasnaes, H. Hasman, B.A. Lund, H.S. Leiros, B. Lilje, J. Janice, L. Jakobsen, P. Littauer, L.M. Soes, B.J. Holzknecht, L.P. Andersen, M. Stegger, P.S. Andersen, and A.M. Hammerum, *Dissemination and Characteristics of a Novel Plasmid-Encoded Carbapenem-Hydrolyzing Class D beta-Lactamase, OXA-436, Found in Isolates from Four Patients at Six Different Hospitals in Denmark.* Antimicrob Agents Chemother, 2018. **62**(1).

56. Robert, X. and P. Gouet, *Deciphering key features in protein structures with the new ENDscript server.* Nucleic Acids Research, 2014. **42**(W1): p. W320-W324.

57. Janin, J., R.P. Bahadur, and P. Chakrabarti, *Protein-protein interaction and quaternary structure.* Q Rev Biophys, 2008. **41**(2): p. 133-80.

58. Danel, F., M. Paetzel, N.C. Strynadka, and M.G. Page, *Effect of divalent metal cations on the dimerization of OXA-10 and -14 class D beta-lactamases from Pseudomonas aeruginosa.* Biochemistry, 2001. **40**(31): p. 9412-20.

59. Franceschini, N., L. Boschi, S. Pollini, R. Herman, M. Perilli, M. Galleni, J.M. Frere, G. Amicosante, and G.M. Rossolini, *Characterization of OXA-29 from Legionella (Fluoribacter) gormanii: molecular class D beta-lactamase with unusual properties.* Antimicrob Agents Chemother, 2001. **45**(12): p. 3509-16.

60. Carugo, O. and K. Djinović-Carugo, *Packing bridges in protein crystal structures.* Journal of Applied Crystallography, 2014. **47**(1): p. 458-461.

61. Arkin, M.R., Y. Tang, and J.A. Wells, *Small-molecule inhibitors of protein-protein interactions: progressing toward the reality.* Chem Biol, 2014. **21**(9): p. 1102-14.

62. Salam, N.K., M. Adzhigirey, W. Sherman, and D.A. Pearlman, *Structure-based approach to the prediction of disulfide bonds in proteins.* Protein Eng Des Sel, 2014. **27**(10): p. 365-74.

63. Fisher, J., R.L. Charnas, S.M. Bradley, and J.R. Knowles, *Inactivation of the RTEM beta-lactamase from Escherichia coli. Interaction of penam sulfones with enzyme.* Biochemistry, 1981. **20**(10): p. 2726-31.

64. Dalbadie-McFarland, G., J.J. Neitzel, and J.H. Richards, *Active-site mutants of beta-lactamase: use of an inactive double mutant to study requirements for catalysis.* Biochemistry, 1986. **25**(2): p. 332-8.

65. Sigal, I.S., B.G. Harwood, and R. Arentzen, *Thiol-beta-lactamase: replacement of the active-site serine of RTEM beta-lactamase by a cysteine residue.* Proc Natl Acad Sci U S A, 1982. **79**(23): p. 7157-60.

66. Holyk, A., V. Belden, J.J. Lee, W. Musick, R. Keul, G.W. Britz, and J. Lin, *Ceftazidime/avibactam use for carbapenem-resistant Klebsiella pneumoniae meningitis: a case report.* J Antimicrob Chemother, 2018. **73**(1): p. 254-256.

67. Fraile-Ribot, P.A., X. Mulet, G. Cabot, E. del Barrio-Tofiño, C. Juan, J.L. Pérez, and A. Oliver, *In Vivo Emergence of Resistance to Novel Cephalosporin–β-Lactamase Inhibitor Combinations through the Duplication of Amino Acid D149 from OXA-2 β-*

Lactamase (OXA-539) in Sequence Type 235 Pseudomonas aeruginosa. Antimicrobial Agents and Chemotherapy, 2017. **61**(9): p. e01117-17.

68. Bush, K. and P.A. Bradford, *beta-Lactams and beta-Lactamase Inhibitors: An Overview.* Cold Spring Harb Perspect Med, 2016. **6**(8).

69. Drawz, S.M. and R.A. Bonomo, *Three decades of beta-lactamase inhibitors.* Clin Microbiol Rev, 2010. **23**(1): p. 160-201.

70. Giddins, M.J., N. Macesic, M.K. Annavajhala, S. Stump, S. Khan, T.H. McConville, M. Mehta, A. Gomez-Simmonds, and A.C. Uhlemann, *Successive Emergence of Ceftazidime-Avibactam Resistance through Distinct Genomic Adaptations in blaKPC-2-Harboring Klebsiella pneumoniae Sequence Type 307 Isolates.* Antimicrob Agents Chemother, 2018. **62**(3).

71. Shields, R.K., L. Chen, S. Cheng, K.D. Chavda, E.G. Press, A. Snyder, R. Pandey, Y. Doi, B.N. Kreiswirth, M.H. Nguyen, and C.J. Clancy, *Emergence of Ceftazidime-Avibactam Resistance Due to Plasmid-Borne blaKPC-3 Mutations during Treatment of Carbapenem-Resistant Klebsiella pneumoniae Infections.* Antimicrob Agents Chemother, 2017. **61**(3).

72. Bruylants, G., J. Wouters, and C. Michaux, *Differential scanning calorimetry in life science: thermodynamics, stability, molecular recognition and application in drug design.* Curr Med Chem, 2005. **12**(17): p. 2011-20.

73. Johnson, C.M., *Differential scanning calorimetry as a tool for protein folding and stability.* Arch Biochem Biophys, 2013. **531**(1-2): p. 100-9.

74. Yang, P.-H. and J.A. Rupley, *Protein-water interactions. Heat capacity of the lysozyme-water system.* Biochemistry, 1979. **18**(12): p. 2654-2661.

75. Calorimetry Sciences Corporation, *Characterizing Protein Stability by DSC*, in *Life Scences Apllication Note* L. Sciences, Editor. 2006.

76. Ibarra-Molero, B. and J.M. Sanchez-Ruiz, *Statistical Differential Scanning Calorimetry: Probing Protein Folding - Unfolding Esembles*, in *Protein Folding, Misfolding and Aggregation: Classical Themes and Novel Approaches* V. Munez, Editor. 2008, RSC Biomolecular Sciences. p. 85-105.

77. Jerabek-Willemsen, M., C.J. Wienken, D. Braun, P. Baaske, and S. Duhr, *Molecular interaction studies using microscale thermophoresis.* Assay Drug Dev Technol, 2011. **9**(4): p. 342-53.

78. Seidel, S.A., P.M. Dijkman, W.A. Lea, G. van den Bogaart, M. Jerabek-Willemsen, A. Lazic, J.S. Joseph, P. Srinivasan, P. Baaske, A. Simeonov, I. Katritch, F.A. Melo, J.E. Ladbury, G. Schreiber, A. Watts, D. Braun, and S. Duhr, *Microscale thermophoresis quantifies biomolecular interactions under previously challenging conditions.* Methods, 2013. **59**(3): p. 301-15.

79. Duhr, S. and D. Braun, *Why molecules move along a temperature gradient.* Proc Natl Acad Sci U S A, 2006. **103**(52): p. 19678-82.

80. Branden, C. and J. Tooze, *Determination of Protein Structures* in *Introduction to Protein Structure* 1999, Garland Science p. 373-392.

81. Russo Krauss, I., A. Merlino, A. Vergara, and F. Sica, *An overview of biological macromolecule crystallization.* Int J Mol Sci, 2013. **14**(6): p. 11643-91.

82. McPherson, A., *Introduction to protein crystallization.* Methods, 2004. **34**(3): p. 254-65.

83. Asherie, N., *Protein crystallization and phase diagrams.* Methods, 2004. **34**(3): p. 266-272.

84. Nelson, D.L. and M.M. Cox, *Enzymes*, in *Lehninger, Principles of Biochemistry* 2013, W.H Freeman and Company. p. 189-241.

85.   Branden, C. and J. Tooze, *An Example of Enzyme Catalysis: Serine Proteinases* in *Introduction to Protein Structure*. 1999, Garland Science p. 205-221.

86.   Bugg, T.D.H., *Methods for Studying Enzymatic Reactions*, in *Introduction to Enzyme and Coenzyme Chemistry*. 2012, WILEY. p. 50-75.

87.   Novoradovsky, A., V. Zhang, M. Ghosh, H. Hogrefe, J.A. Sorge, and T. Gaasterland, *Computational Principles of Primer Design for Site Directed Mutagenesis* in *Technical Proceedings of the 2005 NSTI Nanotechnology Conference and Trade Show, Volume 1*. 2005. p. 532-535.

88.   Cohen, S.N., A.C.Y. Chang, and L. Hsu, *Nonchromosomal Antibiotic Resistance in Bacteria: Genetic Transformation of Escherichia coli by R-Factor DNA.* Proceedings of the National Academy of Sciences of the United States of America, 1972. **69**(8): p. 2110-2114.

89.   Mandel, M. and A. Higa, *Calcium-dependent bacteriophage DNA infection.* J Mol Biol, 1970. **53**(1): p. 159-62.

90.   Tang, X., Y. Nakata, H.O. Li, M. Zhang, H. Gao, A. Fujita, O. Sakatsume, T. Ohta, and K. Yokoyama, *The optimization of preparations of competent cells for transformation of E. coli.* Nucleic Acids Research, 1994. **22**(14): p. 2857-2858.

91.   Petersen, T.N., S. Brunak, G. von Heijne, and H. Nielsen, *SignalP 4.0: discriminating signal peptides from transmembrane regions.* Nat Methods, 2011. **8**(10): p. 785-6.

92.   Cline, J., J.C. Braman, and H.H. Hogrefe, *PCR fidelity of pfu DNA polymerase and other thermostable DNA polymerases.* Nucleic Acids Research, 1996. **24**(18): p. 3546-3551.

93.   Hall, T.A., *BioEdit: a user-friendly biological sequence alignment editor and analysis program for Windows 95/98/NT.* Nucleic Acids Symposium Series, 1999. **41**: p. 95-98.

94.   Thompson, J.D., D.G. Higgins, and T.J. Gibson, *CLUSTAL W: improving the sensitivity of progressive multiple sequence alignment through sequence weighting, position-specific gap penalties and weight matrix choice.* Nucleic Acids Research, 1994. **22**(22): p. 4673-4680.

95.   Nesheim, B.H.B., *Characterization and structural analysis of class D beta-lactamases: variants and mutants of OXA-48 type carbapenemases* in *Chemistry* 2016, UiT, Arctic University of Norway Munin.

96.   van den Berg, S., P.A. Lofdahl, T. Hard, and H. Berglund, *Improved solubility of TEV protease by directed evolution.* J Biotechnol, 2006. **121**(3): p. 291-8.

97.   Wei, L., X. Cai, Z. Qi, L. Rong, B. Cheng, and J. Fan, *In vivo and in vitro characterization of TEV protease mutants.* Protein Expr Purif, 2012. **83**(2): p. 157-63.

98.   Bornhorst, J.A. and J.J. Falke, *[16] Purification of Proteins Using Polyhistidine Affinity Tags.* Methods in enzymology, 2000. **326**: p. 245-254.

99.   Wilkins, M.R., E. Gasteiger, A. Bairoch, J.C. Sanchez, K.L. Williams, R.D. Appel, and D.F. Hochstrasser, *Protein identification and analysis tools in the ExPASy server.* Methods Mol Biol, 1999. **112**: p. 531-52.

100.   Stojanoski, V., D.C. Chow, B. Fryszczyn, L. Hu, P. Nordmann, L. Poirel, B. Sankaran, B.V. Prasad, and T. Palzkill, *Structural Basis for Different Substrate Profiles of Two Closely Related Class D beta-Lactamases and Their Inhibition by Halogens.* Biochemistry, 2015. **54**(21): p. 3370-80.

101.   Akhter, S., B.A. Lund, A. Ismael, M. Langer, J. Isaksson, T. Christopeit, H.S. Leiros, and A. Bayer, *A focused fragment library targeting the antibiotic resistance enzyme - Oxacillinase-48: Synthesis, structural evaluation and inhibitor design.* Eur J Med Chem, 2018. **145**: p. 634-648.

102.   Calorimetry Sciences Corporation, *Nano-Differential Scanning Calorimetry User´s Manual Model CSC 6300*. 2005.

103.   Hong, P., S. Koza, and E.S.P. Bouvier, *Size-Exclusion Chromatography for the Analysis of Protein Biotherapeutics and their Aggregates.* Journal of Liquid Chromatography & Related Technologies, 2012. **35**(20): p. 2923-2950.

104.   Siemann, S., D.P. Evanoff, L. Marrone, A.J. Clarke, T. Viswanatha, and G.I. Dmitrienko, *N-Arylsulfonyl Hydrazones as Inhibitors of IMP-1 Metallo-β-Lactamase.* Antimicrobial Agents and Chemotherapy, 2002. **46**(8): p. 2450-2457.

105.   Rychlik, W., W.J. Spencer, and R.E. Rhoads, *Optimization of the annealing temperature for DNA amplification in vitro.* Nucleic Acids Research, 1990. **18**(21): p. 6409-6412.

106.   Lorenz, T.C., *Polymerase Chain Reaction: Basic Protocol Plus Troubleshooting and Optimization Strategies.* Journal of Visualized Experiments : JoVE, 2012(63): p. 3998.

107.   Chakrabarti, R. and C.E. Schutt, *The enhancement of PCR amplification by low molecular-weight sulfones.* Gene, 2001. **274**(1-2): p. 293-8.

108.   Krissinel, E. and K. Henrick, *Inference of macromolecular assemblies from crystalline state.* J Mol Biol, 2007. **372**(3): p. 774-97.

109.   Simakov, N., D.A. Leonard, J.C. Smith, T. Wymore, and A. Szarecka, *A Distal Disulfide Bridge in OXA-1 beta-Lactamase Stabilizes the Catalytic Center and Alters the Dynamics of the Specificity Determining Omega Loop.* J Phys Chem B, 2017. **121**(15): p. 3285-3296.

110.   Stojanoski, V., C.J. Adamski, L. Hu, S.C. Mehta, B. Sankaran, P. Zwart, B.V. Prasad, and T. Palzkill, *Removal of the Side Chain at the Active-Site Serine by a Glycine Substitution Increases the Stability of a Wide Range of Serine beta-Lactamases by Relieving Steric Strain.* Biochemistry, 2016. **55**(17): p. 2479-90.

111.   Woodbury, R.L., S.J. Hardy, and L.L. Randall, *Complex behavior in solution of homodimeric SecA.* Protein Sci, 2002. **11**(4): p. 875-82.
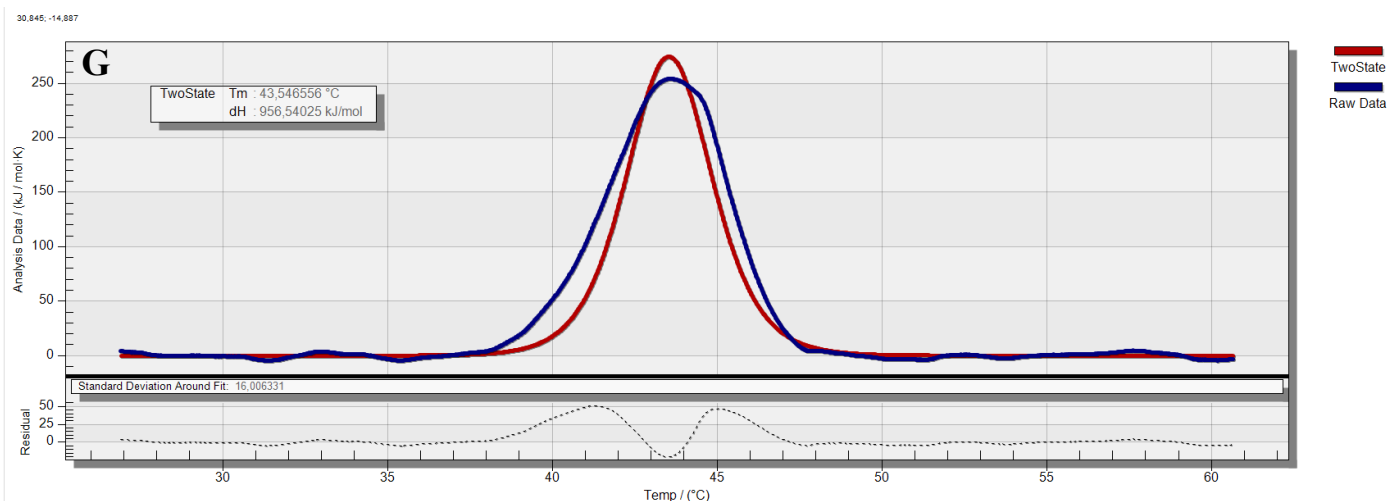
Appendix
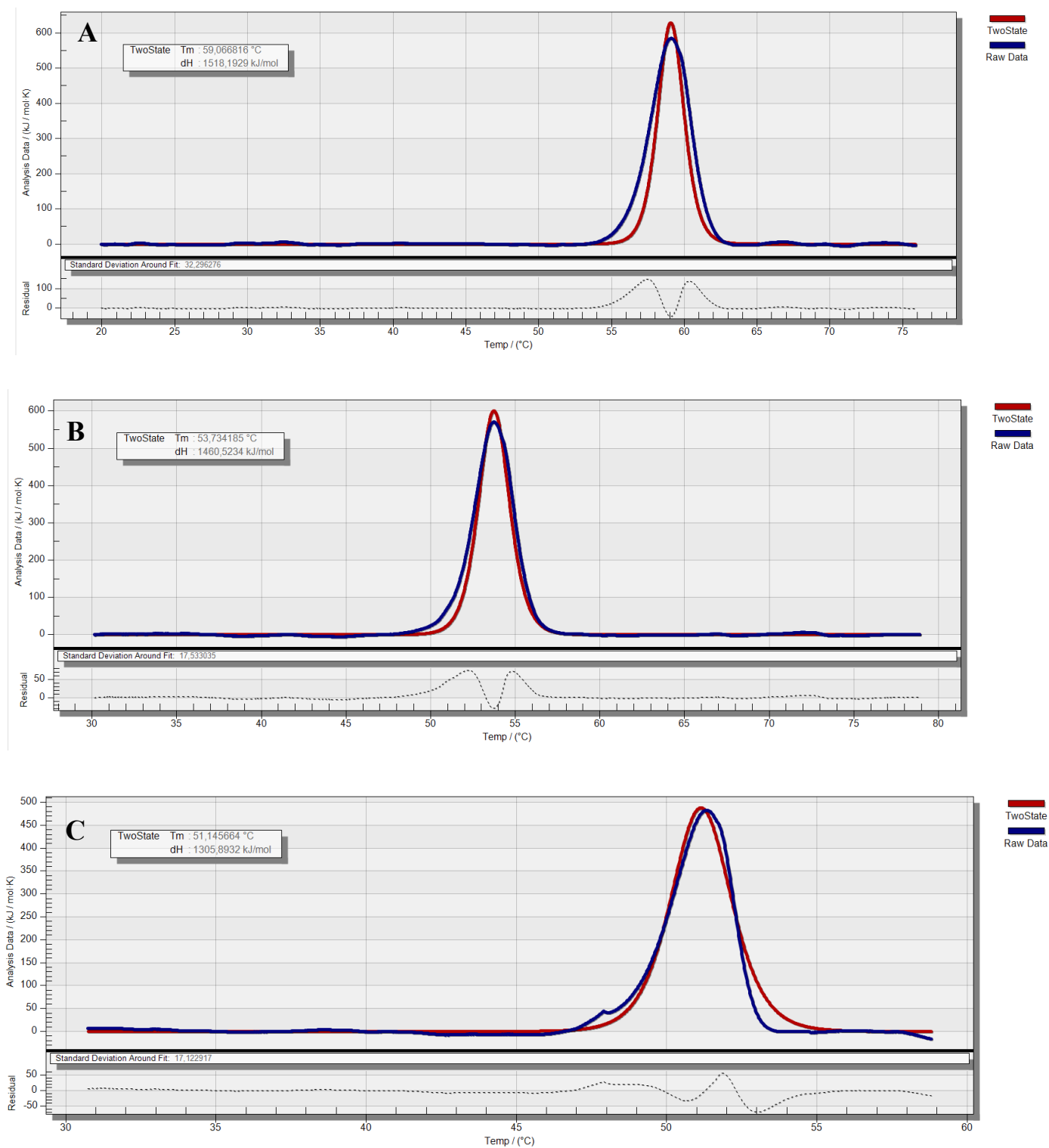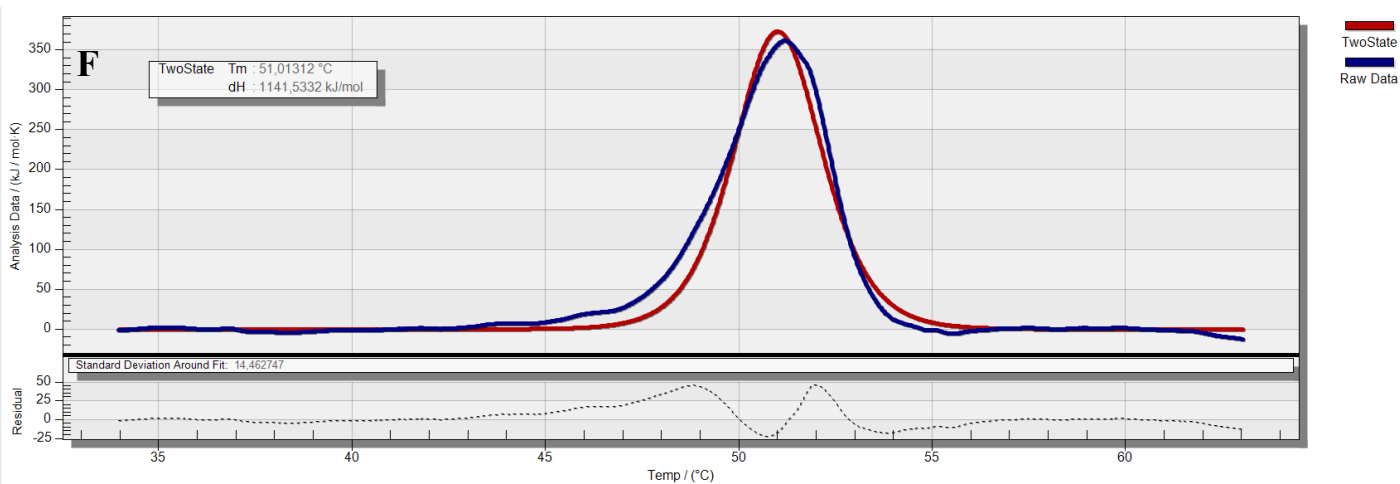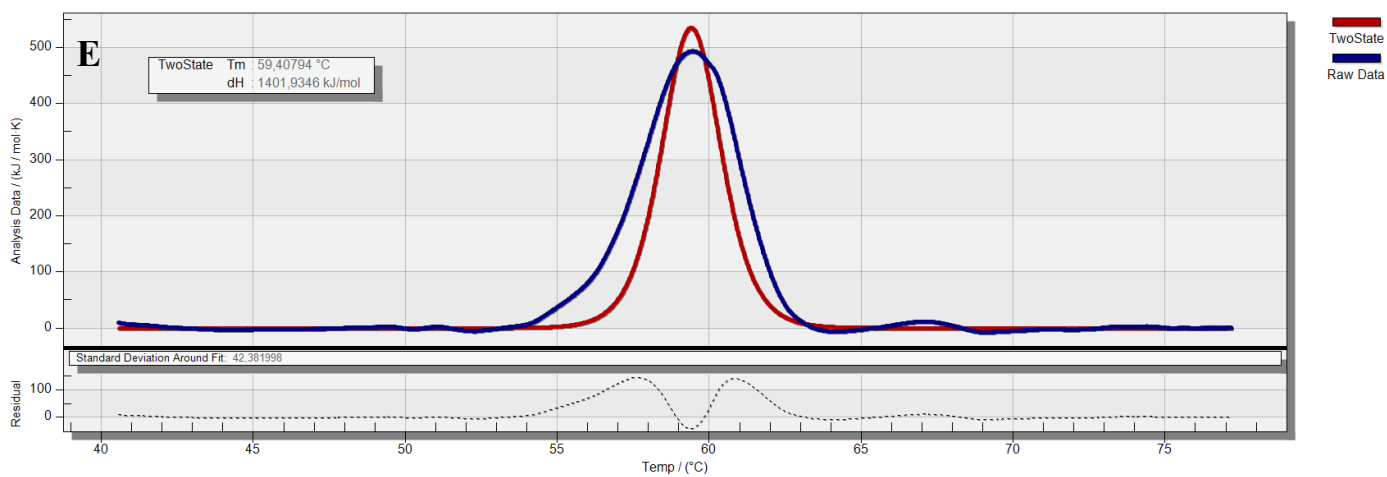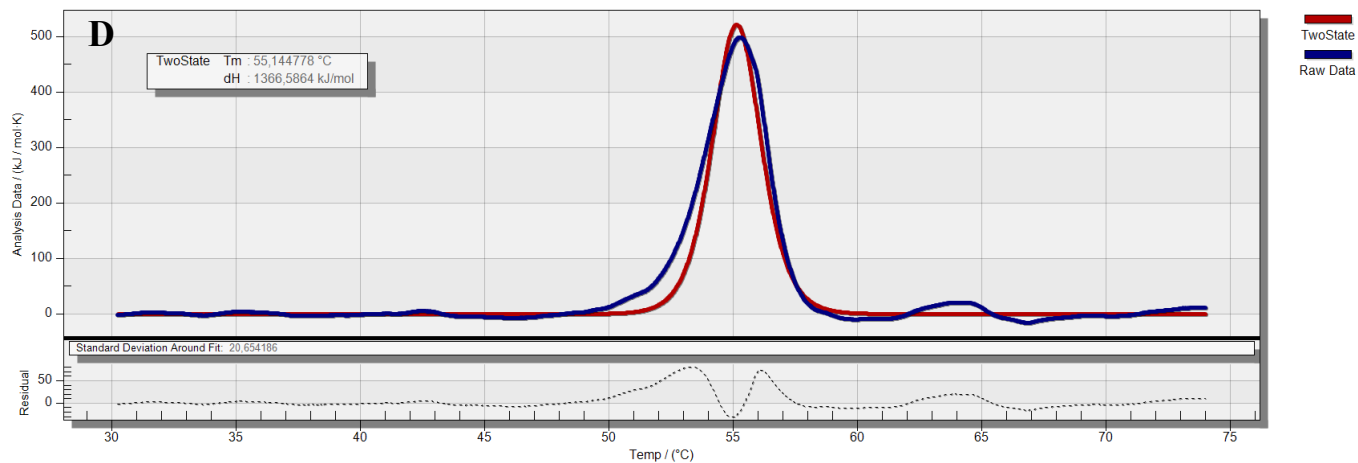
Figure A1: DSC transition curves (blue) for (A) OXA-48, (B) OXA-163, (C) OXA-48 R206A, (D) OXA-181, (E) OXA-245, (F) OXA-48 R189A, and (G) OXA-48 R189A/R206A, dialyzed in 50 mM phosphate buffer pH 7.2, with the theoretical fitted two-state model (red) for the respective dimers, to calculate the enthalpy of protein unfolding. The temperature is given along the x-axis, and the heat capacity along the y-axis.
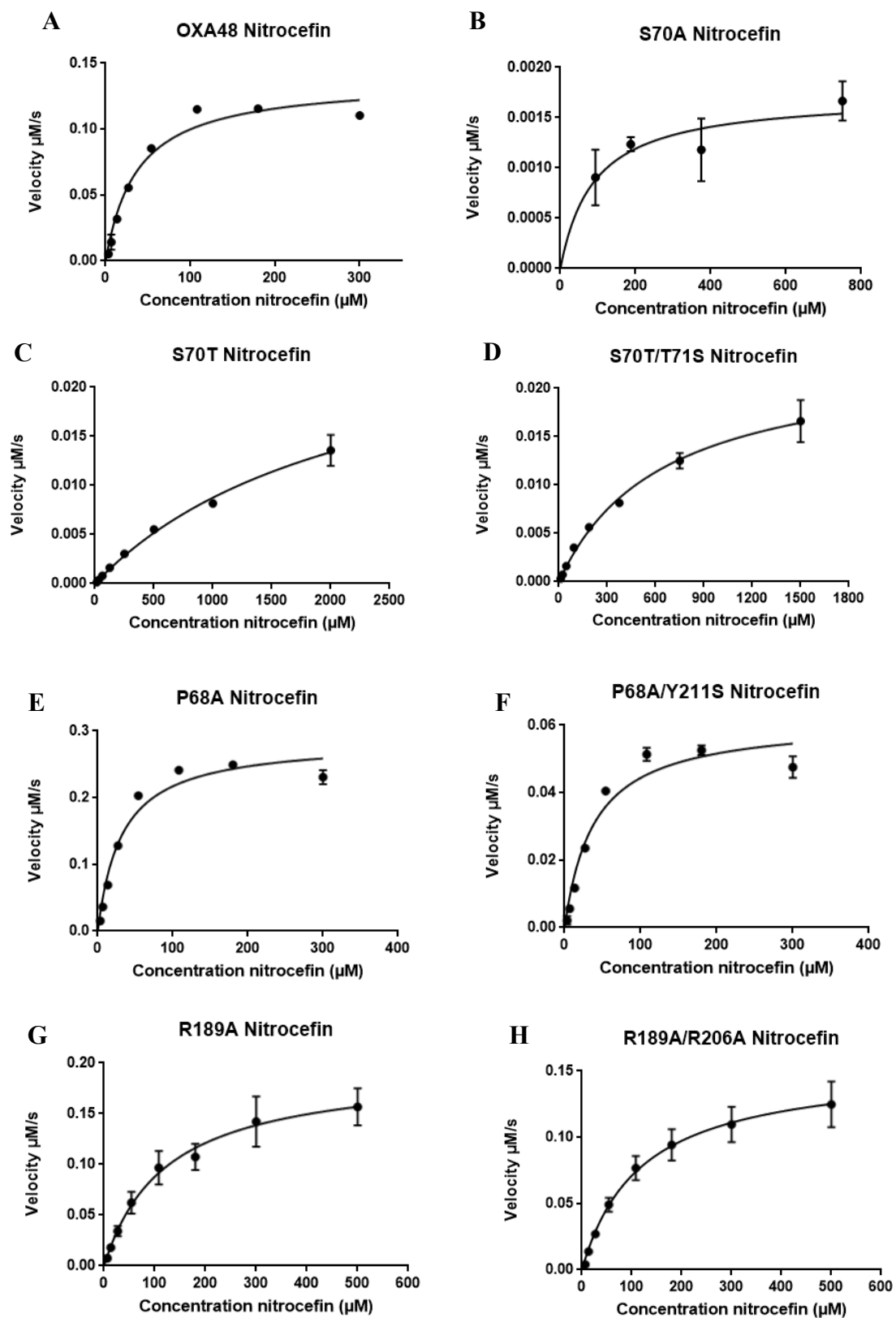
Figure A2: Enzyme kinetics curves for OXA-48 (A) and OXA-48 mutants S70A (B), S70T (C), S70T/T71S (D), P68A (E), P68A/Y211S (F), R189A (G) and R189A/R206A (H) with nitrocefin. The substrate concentrations are given along the x-axis, while the reaction velocity is given along the y-axis. The curves are labelled according to the enzymes.
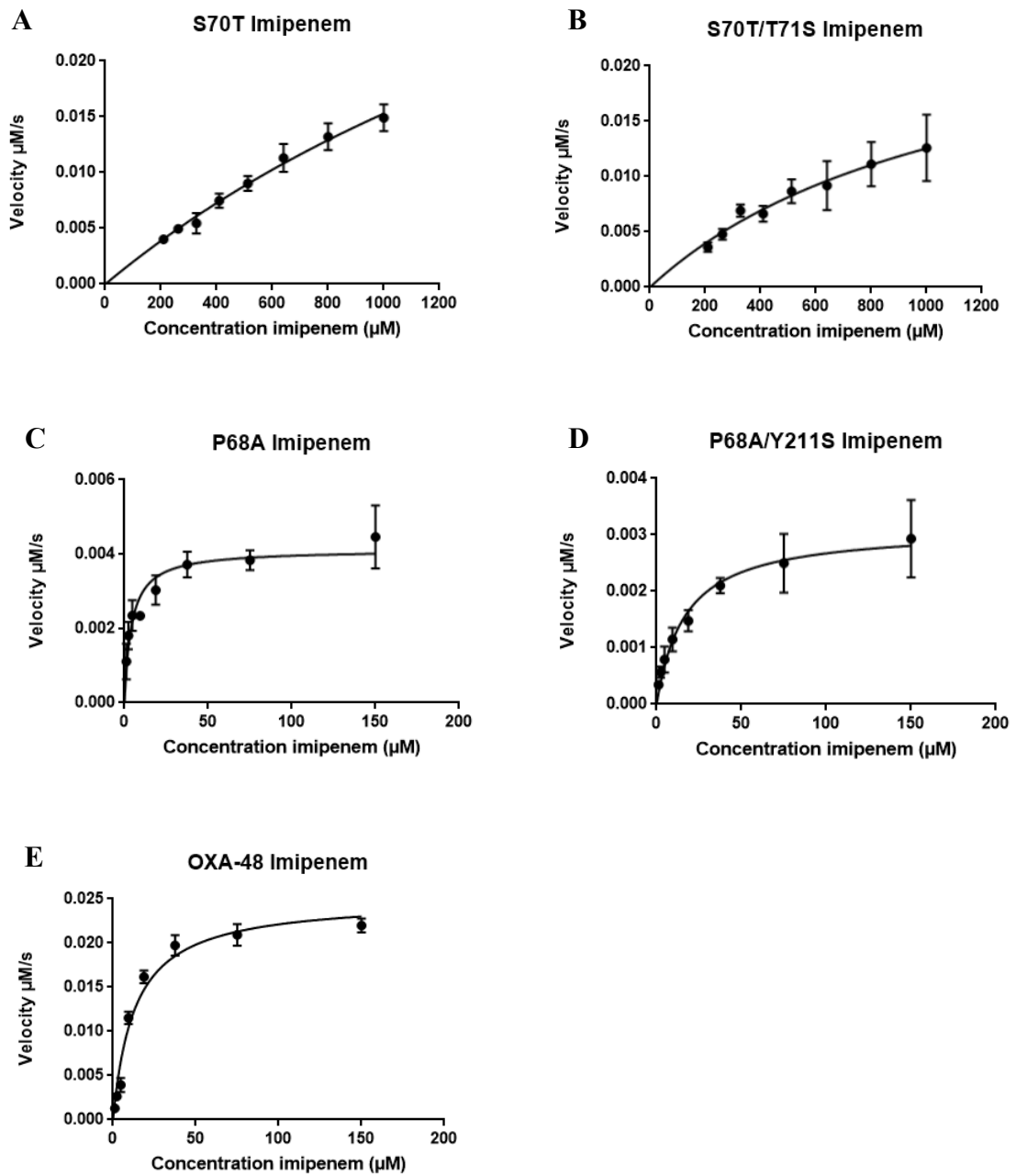
Figure A3: Enzyme kinetics curves for OXA-48 (E) and OXA-48 mutants S70T (A), S70T/T71S (B), P68A (C), and P68A/Y211S (D) with imipenem. The substrate concentrations are given along the x-axis, while the reaction velocity is given along the y-axis. The curves are labelled according to the enzymes.

Figure A4: Enzyme kinetics curves for OXA-48 (C) and OXA-48 mutants P68A (A), and P68A/Y211S (B) with ceftazidime. The substrate concentrations are given along the x-axis, while the reaction velocity is given along the y-axis. The curves are labelled according to the enzymes.

Figure A5: Enzyme kinetics curves for OXA-48 (C) and OXA-48 mutants P68A (A), and P68A/Y211S (B) with ampicillin. The substrate concentrations are given along the x-axis, while the reaction velocity is given along the y-axis. The curves are labelled according to the enzymes.
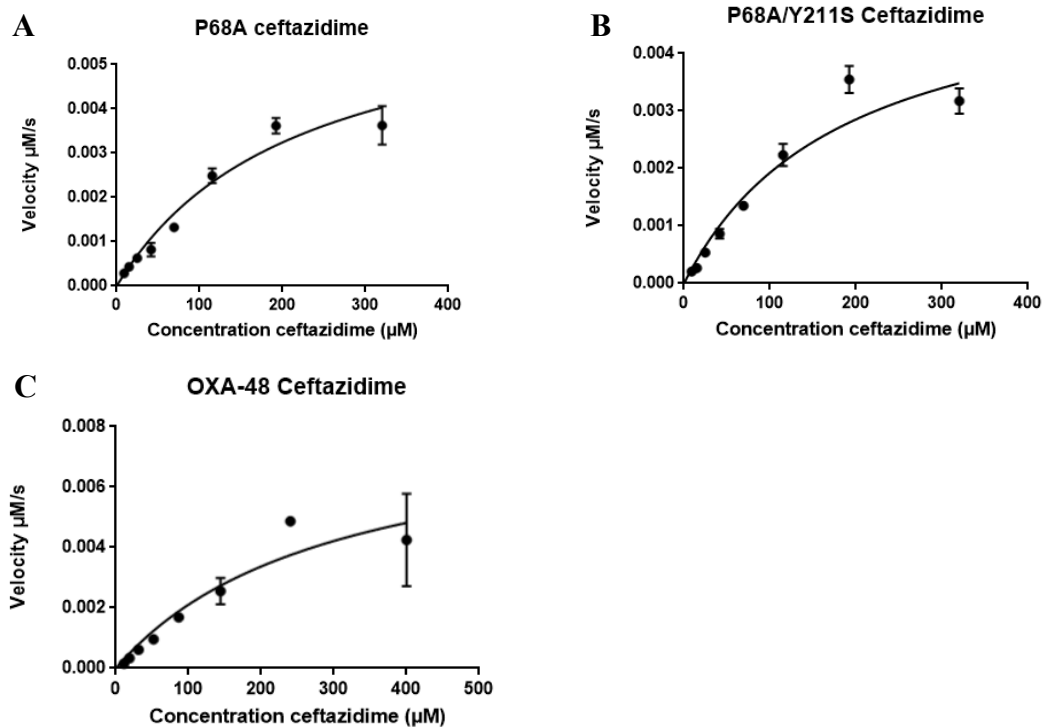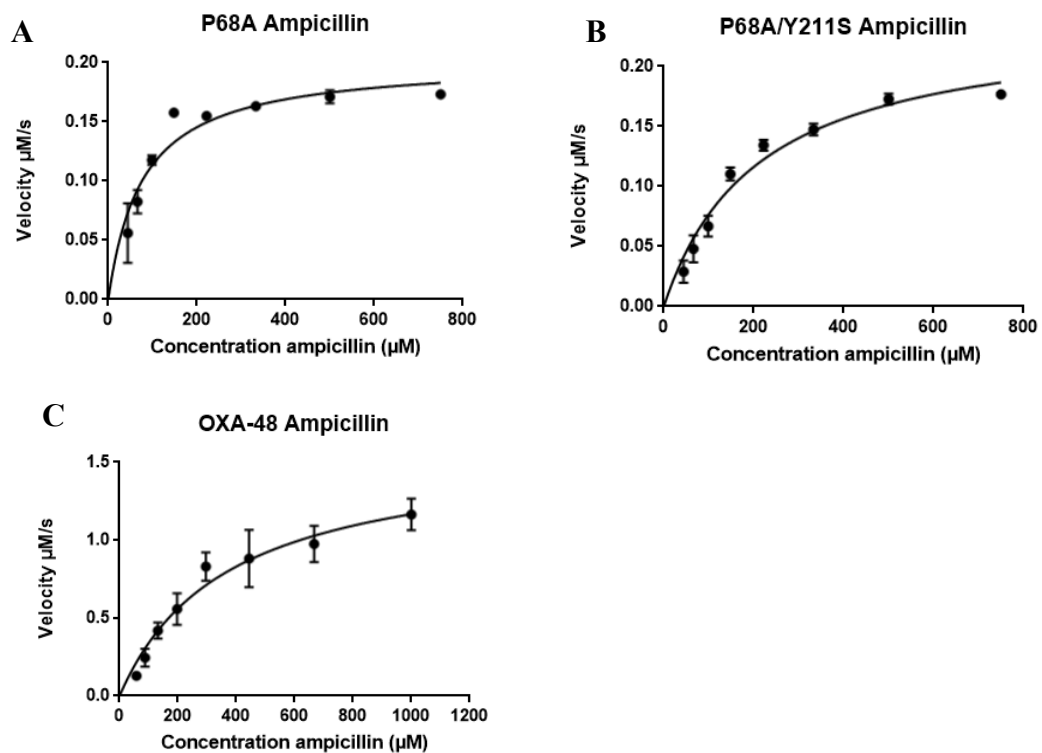
Table A1: X-ray data collection and crystallographic refinement statistics for OXA-48 mutants S70A, S70T, ST70TS, R189A. Values in parenthesis are for the highest resolution shell.

	OXA-48 S70A	OXA-48 S70T	OXA-48 S70T/T71S	OXA-48 R189A
PDB entry				
X-ray source	BESSY, BL14.1 27.2.2018	BESSY, BL14.1 27.2.2018	BESSY, BL14.1 27.2.2018	BESSY, BL14.1 27.2.2018
Data collection statistics				
Space group	$P6_522$ (no. 179)	$P2_1$	$P2_1$	$P2_1$
No. Mol in AU	2	8	8	8
Unit cell (Å)				
a	122.34	107.82	107.22	107.73
b	122.34	85.12	85.30	85.55
c	161.57	125.19	126.45	125.81
β (°)	120	90.15	90.04	90.08
Resolution (Å)	25-1.85 (1.89-1.85)	25.0-2.50 (2.55-2.50)	25.0-1.89 (1.92-1.89)	24.77-2.55 (2.60-2.55)
Wavelength (Å)	0.9184	0.9184	0.9184	0.9184
No. unique reflections	61 335 (3 726)	77 870 (4 452)	175 904 (8 670)	72 168 (4 435)
Multiplicity	12.0 (11.6)	3.5 (3.6)	3.90 (3.9)	3.1 (3.2)
Completeness (%)	100.0 (100.0)	99.1 (99.6)	96.7 (96.5)	96.7 (96.9)
Mean ($<I>/<\sigma_I>$)	12.6 (1.8)	6.0 (1.1)	7.7 (1.1)	4.9 (1.0)
R-merge [a]	0.177 (1.449)	0.165 (1.036)	0.107 (1.109)	0.188 (0.971)
$CC_{1/2}$	0.998 (0.701)	0.990 (0.568)	0.997 (0.513)	0.980 (0.538)
Wilson B-factor (Å^2)	17.5	31.7	24.5	28.3
Refinement statistics				
Resolution (Å)	25.0-1.85	25.0-2.50	25.0-1.89	25.0-2.55
R-factor (all reflections)	0.1480	0.2074	0.216	0.20
R-free	0.1761	0.2756	0.256	0.29
RMSD bond lengths (Å)	0.009	0.004	0.012	0.002
RMSD bond angles (°)	0.98	0.63	1.07	0.46
Ramachandran favored (%)	98.11	95.52	96.84	96.10
Ramachandran outliers (%)	0.00	0.21	0.11	0.37
Clashscore	3.28	2.87	4.16	1.69
Average B-factor (Å^2)	24.63	52.37	41.24	54.53

Appendix Paper 1

Structure, activity and thermostability investigations of OXA-163, OXA-181 and OXA-245 using biochemical analysis, crystal structures and differential scanning calorimetry analysis

Bjarte Aarmo Lund, Ane Molden Thomassen, Trine Josefine Olsen Carlsen and Hanna-Kirsti S. Leiros

Structure, activity and thermostability investigations of OXA-163, OXA-181 and OXA-245 using biochemical analysis, crystal structures and differential scanning calorimetry analysis

Bjarte Aarmo Lund, Ane Molden Thomassen, Trine Josefine Olsen Carlsen and Hanna-Kirsti S. Leiros*

Department of Chemistry, UiT The Arctic University of Norway, 9037 Tromsø, Norway. *Correspondence e-mail: hanna-kirsti.leiros@uit.no

The first crystal structures of the class D β-lactamases OXA-181 and OXA-245 were determined to 2.05 and 2.20 Å resolution, respectively; in addition, the structure of a new crystal form of OXA-163 was resolved to 2.07 Å resolution. All of these enzymes are OXA-48-like and have been isolated from different clinical *Klebsiella pneumoniae* strains and also from other human pathogens such as *Pseudomonas aeruginosa* and *Escherichia coli*. Here, enzyme kinetics and thermostability studies are presented, and the new crystal structures are used to explain the observed variations. OXA-245 had the highest melting point (T_m = 55.8°C), as determined by differential scanning calorimetry, compared with OXA-163 (T_m = 49.4°C) and OXA-181 (T_m = 52.6°C). The differences could be explained by the loss of two salt bridges in OXA-163, and an overall decrease in the polarity of the surface of OXA-181 compared with OXA-245.

1. Introduction

After 70 years, penicillin and other β-lactam antibiotics are still the best weapons for fighting bacterial infections; however, the rise of bacterial strains resistant to β-lactam antibiotics threatens to make them obsolete (O'Neill, 2016; Bush & Macielag, 2010). The most common mechanisms for bacteria to become resistant to β-lactam antibiotics is the uptake of foreign genetic material encoding β-lactamases: enzymes that break down the central β-lactam ring of these antibiotics, rendering them inactive (Bush & Bradford, 2016).

To date (June 2017), over 2600 β-lactamases have been described (Bush, 2013*a*; http://bldb.eu). Based on their genetic sequence and structural motifs, β-lactamases can be grouped into four classes: A–D (Hall & Barlow, 2005; Bush, 2013*b*). The largest class, with more than 500 members, is class D. This class is often referred to as the oxacillinases (OXAs) owing to their preferential hydrolysis of oxacillin. Typically, this class has not been considered to be as threatening as the other classes. Still, it contains members which may inactivate the entire spectrum of β-lactam antibiotics (Leonard *et al.*, 2013; Evans & Amyes, 2014; Docquier & Mangani, 2016).

One of the most geographically widespread members of the class D β-lactamases is OXA-48 (Vallejo *et al.*, 2016). OXA-48 and the increasing number of OXA-48-like variants have been called the 'phantom menace' owing to their broad substrate specificity and the difficulties in identifying bacteria expressing OXA-48-like enzymes (Poirel *et al.*, 2012). The OXA-48-like
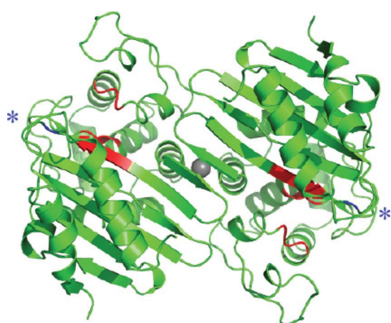
Table 1
Crystallization conditions for tOXA-163, tOXA-181 and tOXA-245.

	tOXA-163	tOXA-181	tOXA-245
Method	Vapour diffusion		
Plate type	Hampton Research VDX 24-well plate with sealant		
Temperature (K)	298		
Protein concentration (mg ml^{-1})	9	11	3
Buffer composition of protein solution	50 mM HEPES pH 7.2, 50 mM K$_2$SO$_4$	50 mM Tris pH 7.2, 50 mM K$_2$SO$_4$	25 mM HEPES pH 7.5
Composition of reservoir solution	0.1 M Tris pH 9.0, 28% PEG 500	0.1 M Tris pH 7.0, 0.2 M ammonium sulfate, 20.5% PEG MME 5000	0.1 M HEPES pH 7.0, 10% PEG 6000
Drop volume (µl)	2	1	2
Protein:reservoir ratio	3:20	1:1	1:1
Reservoir volume (µl)	1000	800	500

β-lactamases OXA-163, OXA-181 and OXA-245 have all been identified in *Klebsiella pneumoniae* (Potron, Nordmann *et al.*, 2011; Oteo *et al.*, 2013). Although *K. pneumoniae* is most commonly found in soil and water, it frequently causes infections in immunocompromised individuals and has been connected to outbreaks of nosocomial infections (Podschun & Ullmann, 1998; Paczosa & Mecsas, 2016; Navon-Venezia *et al.*, 2017). OXA-163 and OXA-181 have also been identified in other human pathogens such as *Escherichia coli* (McGann *et al.*, 2015; Stoesser *et al.*, 2016), and OXA-181 has been identified in *Pseudomonas aeruginosa* strains (Meunier *et al.*, 2016). OXA-181 is reported to originate from a *Shewanella xiamenensis* chromosomal β-lactamase (Potron, Poirel *et al.*, 2011) and OXA-163 also appears to originate from *Shewanella*. spp, while OXA-245 appears from random mutations of the OXA-48 gene in *K. pneumoniae* strains (Pérez-Vázquez *et al.*, 2016). OXA-163 was first identified in Argentina (Poirel *et al.*, 2011), but has also been observed in Egypt (Abdelaziz *et al.*, 2012). OXA-181 has been identified all over the world (Potron, Nordmann *et al.*, 2011; Samuelsen *et al.*, 2013; Rojas *et al.*, 2017). The strain responsible for OXA-245, however, appears to be limited to Spain (Pérez-Vázquez *et al.*, 2016). The sequence identities compared with OXA-48 are 98.0% for OXA-163, 98.4% for OXA-181 and 99.6% for OXA-245, using Gly22 (left after TEV cleavage) and the periplasmic part (Lys23–Pro256) for all four enzymes.

While class D β-lactamases are a diverse class with respect to protein sequence, their tertiary structures are highly conserved. All known structures of OXAs share an $\alpha\beta$-fold and many form dimers in solution (Docquier *et al.*, 2009; Paetzel *et al.*, 2000; Dale & Smith, 1976). The active site of OXAs is made up of three conserved motifs, $_{70}$STFK$_{73}$, $_{118}$SVV$_{120}$ and $_{208}$KTG$_{210}$, and each monomer has an independent active site. The serine in the STFK motif has been identified as the nucleophile that is responsible for the formation of the acyl-complex with β-lactam antibiotics (Paetzel *et al.*, 2000), while the lysine in the same motif has a conserved post-translational carboxylation that is important for deacetylation (Schneider *et al.*, 2009). The structures of the homologues OXA-48, OXA-163, OXA-232 and OXA-405 have been published (Docquier *et al.*, 2009; Stojanoski *et al.*, 2015). In this study, we wanted to thoroughly characterize the antibiotic-resistance enzymes OXA-163, OXA-181 and OXA-245 by comparing their thermostabilities, hydrolytic properties

and crystal structures with those of the OXA-48 enzyme with worldwide spread.

2. Materials and methods

2.1. Cloning of OXA-181 and OXA-245 and recombinant macromolecule production

Genes encoding OXA-181 and OXA-245 were amplified from clinical isolates and cloned into a pDEST-17 vector using exponential megaprimer cloning (EMP) as described previously (Lund *et al.*, 2014, 2016). Two gene constructs were made for both OXA-181 and OXA-245, in which one gene construct encoded the full-length gene with the signal peptide, thus including residues 1–265 (nOXA-181 and nOXA-245), and a second gene construct encoded a truncated gene with a hexahistidine (His) tag and a TEV protease site followed by residues 23–265 (tOXA-181 and tOXA-245).

Synthetic DNA encoding an OXA-163 construct with a TEV protease site (ENLYFQG) followed by residues Lys23–Pro265 (tOXA-163), codon-optimized for expression in *E. coli*, was purchased from Life Technologies (Thermo Fisher Scientific). The DNA was inserted in pDEST17, which carries an N-terminal His tag. The primers and strains used in this study are described in Supplementary Table S1.

All enzymes were produced recombinantly. tOXA-181 and tOXA-163 were produced in *E. coli* BL21 (DE3) pLysS cells in Terrific Broth medium (TB) with 100 µg ml^{-1} ampicillin and 34 µg ml^{-1} chloramphenicol, the cells were induced by 0.4 mM isopropyl β-D-1-thiogalactopyranoside (VWR) at log phase and expression was continued at 20°C for 16 h. nOXA-181, nOXA-245 and tOXA-245 were produced in *E. coli* BL21 Star (DE3) pRARE cells in ZYP5052 autoinduction medium at 310 K (37°C) for 3–4 h and then left at 293 K (20°C) for 16 h.

Recombinant nOXA-181 and nOXA-245 were isolated from the periplasm after lysozyme treatment and were purified by two steps using an anion exchanger (Giuliani *et al.*, 2005). Contaminants were bound on an anion-exchange Q Sepharose column at 277 K (4°C) equilibrated with 25 mM bis-tris propane pH 7.2. The pH of the running buffer was adjusted to pH 9.5 before applying a pH gradient from pH 9.5 to 6.5 with 25 mM bis-tris propane. A cation-exchange column (HiTrap SP) was used for polishing with a gradient from pH 6.5 (25 mM HEPES) to pH 8.5 (25 mM HEPES) with 150 mM

Table 2
X-ray data-collection and processing statistics for tOXA-163, tOXA-181 and tOXA-245.

Values in parentheses are for the outer resolution shell.

	tOXA-163	tOXA-181	tOXA-245
Diffraction source	BL14.1, BESSY	BL14.1, BESSY	BL14.1, BESSY
Wavelength (Å)	0.918409	0.918409	0.918409
Temperature (K)	100	100	100
Detector	PILATUS 6M	PILATUS 6M	PILATUS 6M
Crystal-to-detector distance (mm)	293.51	426.55	371.19
Rotation range per image (°)	0.1	0.1	0.1
Total rotation range (°)	200	120	200
Exposure time per image (s)	0.4	0.3	0.3
Space group	$P6_522$	$P6_2$	$P2_1$
a, b, c (Å)	121.92, 121.92, 160.43	143.93, 143.93, 53.543	64.16, 108.72, 83.68
α, β, γ (°)	90, 90, 120	90, 90, 120	90, 102.39, 90
Mosaicity (°)	0.12	0.08	0.13
Resolution range (Å)	24.49–2.07 (2.14–2.07)	35.98–2.05 (2.12–2.05)	41.06–2.20 (2.28–2.20)
Total No. of reflections	476104 (48568)	258749 (26225)	211084 (21915)
No. of unique reflections	43401 (4244)	40027 (3911)	56510 (5674)
Completeness (%)	99.90 (100.00)	99.55 (99.21)	99.25 (99.95)
Multiplicity	11.0 (11.4)	6.5 (6.6)	3.7 (3.9)
$\langle I/\sigma(I)\rangle$	12.66 (2.98)	13.19 (2.27)	11.15 (3.63)
R_{meas}	0.1614 (0.8966)	0.08461 (0.8693)	0.0954 (0.387)
Overall B factor from Wilson plot (Å^2)	24.49	29.65	29.30

potassium sulfate. Recombinant tOXA-163, tOXA-181 and tOXA-245 were isolated from sonicated and clarified samples, and were first purified by nickel immobilized metal-affinity chromatography (Ni-IMAC) at 277 K (4°C) with a 0–500 mM imidazole gradient also including 25 mM HEPES pH 6.5 and 50 mM potassium sulfate (Lund *et al.*, 2016). The semi-pure enzyme extract was then cleaved using in-house-purified TEV protease (with L56V, S135G, S219N, T17S, N68D and I77V mutations; Leiros *et al.*, 2014) to remove the His tag, and the cleaved protein was again purified using Ni-IMAC, with the cleaved protein eluting in the flowthrough (Lund *et al.*, 2016; Leiros *et al.*, 2014). The last polishing step was a cation-exchange column as described for the enzyme isolated from the periplasm. Finally, the TEV constructs were dialysed in different storage buffers (Table 1), and nOXA-181 and nOXA245 were dialysed in 50 mM HEPES pH 7.2, 50 mM potassium sulfate. The proteins were concentrated using Centriprep centrifugal filters (Merck) and the protein concentrations were measured using the OD$_{280}$, molecular weights (MW) and extinction coefficients for each gene construct.

2.2. Enzyme kinetics of nOXA-181 and nOXA-245

Enzyme characterization and determination of the kinetic parameters were carried out as previously described for nOXA-48 (Antunes *et al.*, 2014; Lund *et al.*, 2016). Substrate hydrolysis was measured by monitoring the UV absorbance for ampicillin ($\Delta\varepsilon_{235\,nm} = -820\ M^{-1}\,cm^{-1}$, 1–100 µ$M$, 100 p$M$ nOXA-181/nOXA-245); ceftazidime ($\Delta\varepsilon_{260\,nm} = -9000\ M^{-1}\,cm^{-1}$, 18–300 µ$M$, 5 n$M$ nOXA-181/10 nM nOXA-245); ertapenem ($\Delta\varepsilon_{300\,nm} = -6920\ M^{-1}\,cm^{-1}$, 10–1000 µ$M$, 5 n$M$ nOXA-181/nOXA-245); imipenem ($\Delta\varepsilon_{300\,nm} = -9000\ M^{-1}\,cm^{-1}$, 1–100 µ$M$, 5 n$M$ nOXA-181/nOXA-245) and meropenem ($\Delta\varepsilon_{300\,nm} = -6500\ M^{-1}\,cm^{-1}$, 0.02–50 µ$M$, 5 n$M$ nOXA-181/2 nM OXA-245). A SpectraMax M2e

(Molecular Devices, Sunnyvale, California, USA) plate reader at 25°C and nonlinear regression using *GraphPad Prism* 6 (GraphPad Software) were used to determine k_{cat} and K_m with substrate-hydrolysis velocities from the linear phase of the reaction course.

2.3. Thermostability analysis by differential scanning calorimetry (DSC)

Purified tOXA-48 (Lund *et al.*, 2016), tOXA-163, tOXA-181 and tOXA-245 were dialyzed against 50 mM HEPES pH 7.0 supplemented with 50 mM potassium sulfate. Enzyme concentrations were in the range 0.5–1 mg ml^{-1}. All samples were filtrated and degassed. Temperatures were scanned in the range 10–80°C with a gradient of 1°C min^{-1}. To calculate the heat capacities the concentrations and molecular weights were given for the dimers. All measurements were collected using a CSC Nano-Differential Scanning Calorimeter III (N-DSC III) with the pressure kept constant at 304 kPa. All data were analyzed in *NanoAnalyze* 3.6 (TA Instruments, New Castle, Delaware, USA).

2.4. Crystallization conditions

tOXA-163, tOXA-181 and tOXA-245 were used for crystallization experiments. Conditions for tOXA-163 (9 mg ml^{-1}) and tOXA-181 (11 mg ml^{-1}) were identified from screening 284 in-house stochastic crystallization conditions, whereas the conditions for tOXA-245 (3 mg ml^{-1}) were based on the conditions for the tOXA-48 homologue. Ethanediol was added to the crystallization condition at 17, 20 and 25% to cryoprotect tOXA-163, tOXA-181 and tOXA-245, respectively, prior to flash-cooling the crystals in liquid nitrogen. Crystallization information is summarized in Table 1.

Table 3
Refinement statistics for tOXA-163, tOXA-181 and tOXA-245.

Values in parentheses are for the outer shell.

	tOXA-163	tOXA-181	tOXA-245
Resolution range (Å)	24.49–2.07	35.98–2.05	41.06–2.20
	(2.14–2.07)	(2.12–2.05)	(2.28–2.20)
Completeness (%)	99.90 (100.00)	99.55 (99.21)	99.25 (99.95)
No. of reflections			
Working set	43401 (4244)	39856 (3913)	56501 (5674)
Test set	2186 (222)	1971 (165)	1290 (129)
Final R_{cryst}	0.1456 (0.1821)	0.2034 (0.3398)	0.1951 (0.2304)
Final R_{free}	0.1870 (0.2014)	0.2418 (0.4248)	0.2307 (0.2924)
No. of non-H atoms			
Protein	3975	3956	7944
Ligands	17	6	3
Water	367	476	536
Total	4359	4438	8483
R.m.s. deviations			
Bonds (Å)	0.014	0.003	0.004
Angles (°)	1.38	0.54	0.86
Average B factors (Å^2)			
Overall	32.84	37.78	39.04
Protein	31.88	36.68	38.87
Ligands	54.98	76.17	25.01
Water	42.28	46.40	41.65
Ramachandran plot			
Most favoured (%)	97.22	97.89	97.5
Allowed (%)	2.78	2.11	2.5

2.5. X-ray data collection and processing

X-ray diffraction data were collected on BL14.1 operated by the Helmholtz-Zentrum Berlin (HZB) at the BESSY II electron-storage ring (Berlin-Adlershof, Germany; Mueller *et al.*, 2015). Images were indexed and integrated using *XDS* (Kabsch, 2010) and were merged and scaled using *AIMLESS* (Evans & Murshudov, 2013). 5% of reflections were used for cross-validation for tOXA-163 and tOXA-181, whereas 2%

were used for tOXA-245. X-ray data-collection and processing statistics are summarized in Table 2.

2.6. Structure solution and refinement

The structures were solved using *Phaser* (McCoy *et al.*, 2007) with one monomer of OXA-48 (PDB entry 3hbr; Docquier *et al.*, 2009) as the search model. Refinement was carried out using *phenix.refine* (Afonine *et al.*, 2012), with individual isotropic *B* factors and torsion-angle NCS restraints. Models were inspected and manually modified using *Coot* (Emsley *et al.*, 2010). For the final refinement, TLS parameters were refined and refinement weights were optimized. Refinement statistics are summarized in Table 3. Interactions within each protein were evaluated using the *Protein Interactions Calculator* (*PIC*; Tina *et al.*, 2007) and the *Protein Interfaces, Surfaces and Assemblies* service *PISA* at the European Bioinformatics Institute (http://www.ebi.ac.uk/pdbe/prot_int/pistart.html; Krissinel & Henrick, 2007). Figures were prepared using *PyMOL* (v1.8; Schrödinger).

3. Results and discussion

3.1. Enzyme production and enzyme kinetics

In this paper two gene constructs were used: either with native leader sequences followed by periplasmic purification (nOXA-181 and nOXA-245) or His-TEV gene constructs (tOXA-163, tOXA-181 and tOXA.245), where the His tag was cleaved with TEV protease. All gene constructs were expressed in *E. coli*. The highest yield was obtained for tOXA-181, with up to 55 mg of enzyme per litre in BL21 (DE3) pLysS cells in TB medium. tOXA-163 was expressed in BL21 (DE3) pLysS cells in TB medium, whereas nOXA-181,
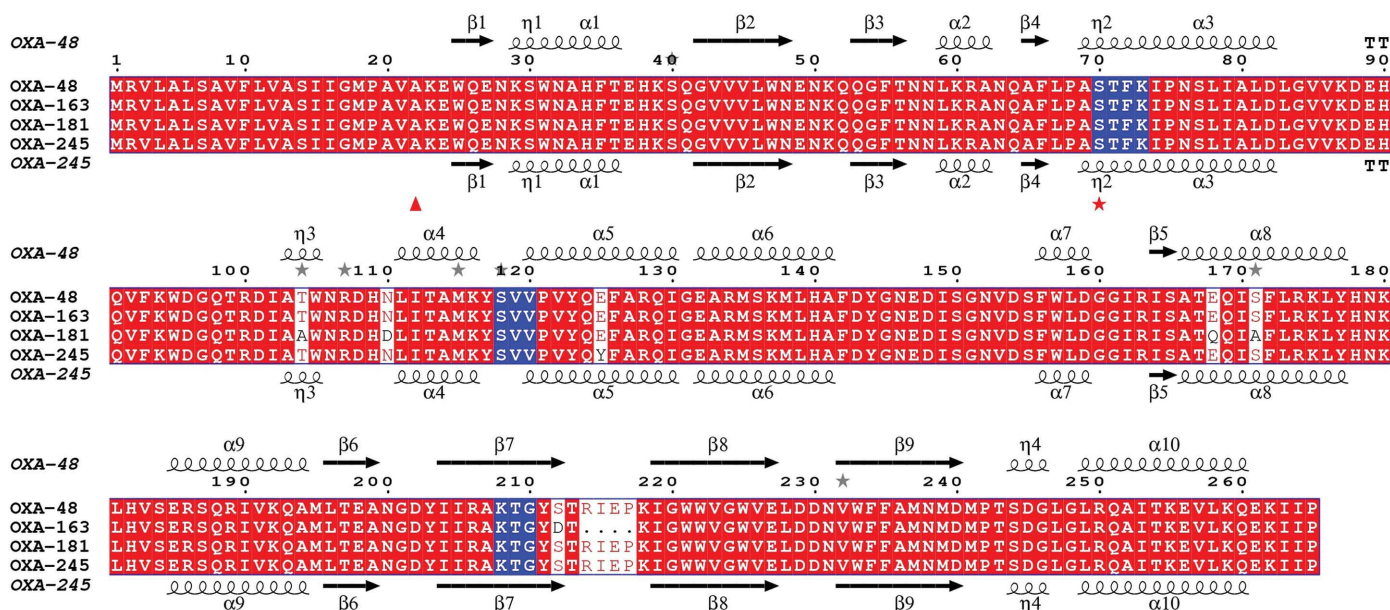

Figure 1
Sequence alignment of OXA-48, OXA-163, OXA-181 and OXA-245. The conserved active-site motifs are marked in blue. Secondary-structure elements are from the crystal structures of tOXA-48 (top; PDB entry 5dtk) and tOXA-245 (bottom; PDB entry 5oe2). The red triangle denotes the end of the signal peptide. The red star denotes the active-site serine. Grey stars indicate residues with alternate conformations in the crystal structure of OXA-48. This figure was prepared using *ESPript* 3.0 (Robert & Gouet, 2014).

Table 4
Kinetic parameters of purified nOXA-181 and nOXA-245 with standard errors from three replicates, showing similar hydrolytic properties compared with nOXA-48.

Results for nOXA-48 and OXA-163 are included for reference (Lund *et al.*, 2016; Poirel *et al.*, 2011).

	Penicillin	Cephalosporin	Carbapenems		
	Ampicillin	Ceftazidime	Ertapenem	Imipenem	Meropenem
nOXA-181					
K_m (µM)	23 ± 5	170 ± 90	900 ± 300	17 ± 4	0.3 ± 0.1
k_{cat} (s^{-1})	2100 ± 200	0.7 ± 0.2	1.6 ± 0.3	5.1 ± 0.4	0.013 ± 0.01
k_{cat}/K_m (µM^{-1} s^{-1})	91	0.004	0.002	0.3	0.04
nOXA-245					
K_m (µM)	35 ± 13	110 ± 80	80 ± 20	11 ± 1	2 ± 0.8
k_{cat} (s^{-1})	1200 ± 200	0.3 ± 0.1	0.29 ± 0.03	4.4 ± 0.2	0.11 ± 0.01
k_{cat}/K_m (µM^{-1} s^{-1})	34	0.003	0.004	0.40	0.05
nOXA-48†					
K_m (µM)	150	5100	100	7.9	1
k_{cat} (s^{-1})	560	4	0.13	4.5	0.1
k_{cat}/K_m (µM^{-1} s^{-1})	4	0.0008	0.001	0.6	0.1
OXA-163‡					
K_m (µM)	320	>2000	150	530	2200
k_{cat} (s^{-1})	25	200	0.01	0.03	0.07
k_{cat}/K_m (µM^{-1} s^{-1})	0.1	<0.1	0.00007	0.00006	0.00003

† The enzyme kinetic parameters for nOXA-48 with ampicillin, imipenem and meropenem are from Lund *et al.* (2016), those with ceftazidime are from Poirel *et al.* (2004) and those with ertapenem are from Docquier *et al.* (2009).   ‡ The enzyme kinetic parameters for OXA-163 are from Poirel *et al.* (2011).

nOXA-245 and tOXA-245 were expressed in BL21 STAR (DE3) pRARE cells in ZYP5052 autoinduction medium.

The substitutions in the protein sequence for OXA-181 and OXA-245 (Fig. 1) are located away from the active-site residues (Fig. 3), and none of the conserved motifs $_{70}$STFK$_{73}$, $_{118}$SVV$_{120}$ or $_{208}$KTG$_{210}$ appear to be influenced. However, it is well known that modifications of distal sites may influence enzyme activity (Guarnera & Berezovsky, 2016), so we enzymatically characterized nOXA-181 and nOXA-245 and compared our results with the reported values for OXA-48 (Lund *et al.*, 2016; Docquier *et al.*, 2009; Poirel *et al.*, 2004) and OXA-163 (Poirel *et al.*, 2011). We tested the substrates ampicillin, ceftazidime, ertapenem, imipenem and meropenem. Both enzymes showed activity against all of the substrates (Table 4); however, ceftazidime was a poor substrate. In summary, the substitutions in nOXA-181 and nOXA-245 did not significantly change the enzymatic characteristics compared with OXA-48. OXA-163, however, has an overall lower catalytic efficiency, but much higher turnover rates for ceftazidime.

3.2. Thermostability analysis by differential scanning calorimetry

Even though the enzyme kinetics did not reveal any significant functional changes between nOXA-181 and nOXA-245, an investigation of thermostability properties could still reveal differences. We determined the midpoint melting temperatures (T_m) for tOXA-48, tOXA-163, tOXA-181 and tOXA-245 by differential scanning calorimetry (DSC). Since all four enzymes are dimers according to interaction analysis of the crystal structures, with 10–20% of the surface buried up on dimerization (Krissinel & Henrick, 2007), and gel-filtration experiments of OXA-48 indicate dimer formation (data not shown), the curves were fitted with the molecular weights and concentrations of the dimers. The recorded melting curves (Fig. 2) and their fit to the two-state model (Supplementary Fig. S1) indicate that all four enzymes unfold *via* a two-state transition without a stable intermediate, like many other dimeric proteins (Neet & Timm, 1994). tOXA-163 and tOXA-181 have a broader melting curves than tOXA-48 and tOXA-245 (Fig. 2) possibly owing to lower protein concentrations, nonhomogeneous samples or minor impurities. Still, we found tOXA-163 to be the least stable of the OXA-48-like enzymes, with a T_m of 49.40°C compared with the other OXA-48-like enzymes with midpoint melting temperatures of 55.3°C (tOXA-48), 52.6°C (tOXA-181) and 55.8°C (tOXA-245) (Table 5, Fig. 2).
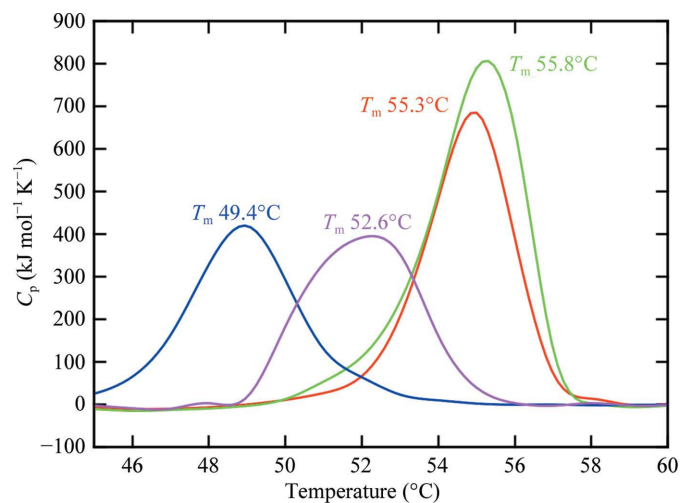

Figure 2
Differential scanning calorimetry curves for tOXA-48 (red), tOXA-163 (blue), tOXA-181 (purple) and tOXA-245 (green) showing that tOXA-245 and tOXA-48 have the highest melting temperatures, whereas tOXA-181 and tOXA-163 have lower melting points.

Table 5
Midpoint melting temperatures (T_m) determined by differential scanning calorimetry for tOXA-48, tOXA-163, tOXA-181 and tOXA-245.

T_m values are given as the mean with standard deviations from duplicate experiments performed in 50 m*M* HEPES pH 7.0 with 50 m*M* potassium sulfate. The apparent unfolding enthalpies (ΔH) with standard deviations were calculated for a two-state model with the enzymes modelled as dimers.

	T_m (°C)	ΔH (kJ mol^{-1})
tOXA-48	55.3 ± 0.2	1500 ± 200
tOXA-163	49.4 ± 0.1	1280 ± 50
tOXA-181	52.6 ± 0.1	1400 ± 300
tOXA-245	55.8 ± 0.1	1700 ± 100

3.3. New crystal structures of tOXA-181 and tOXA-245, and a new tOXA-163 crystal form resolved by X-ray crystallography

We present the first crystal structures of the OXA-48-like β-lactamases tOXA-181 and tOXA-245 and a new crystal form of tOXA-163. The new crystal form of tOXA-163 belonged to space group $P6_522$ and diffracted to 2.07 Å resolution, with R_{cryst} and R_{free} values of 0.15 and 0.19, respectively. The tOXA-181 enzyme crystallized in space group $P6_2$ and diffracted to 2.05 Å resolution, with R_{cryst} and R_{free} values of 0.20 and 0.24, respectively. Finally, tOXA-245 crystallized in space group $P2_1$ and diffracted to 2.20 Å resolution, with refined R_{cryst} and R_{free} values of 0.20 and 0.23, respectively. Gly22 from the TEV site is absent in all structures and Lys23 is missing in all tOXA-181 and tOXA-245 chains, but otherwise all residues are included in the final PDB models. The asymmetric unit of the new crystal structures are different (Fig. 3): tOXA-163 and tOXA-181 have a dimer in the asymmetric unit, corresponding to the expected biological assembly, while tOXA-245 has two dimers in the asymmetric unit. An interesting feature is the chloride ions that are observed to bridge two arginines at the dimer interface: one arginine from each monomer in all three new OXA structures. Other class D β-lactamases such as OXA-10 are known to have a cation-mediated dimerization with a histidine acid in the same position binding to a divalent cation such as cobalt, copper or zinc (Paetzel *et al.*, 2000; Danel *et al.*, 2001).

As expected from the sequence alignment (Fig. 1), the new structures show a close resemblance in their tertiary structure. The mutations are all on the surface of the proteins and the dimer interface is undisturbed. When all monomers of the new structures are compared against each other (tOXA-163, tOXA-181 and tOXA-245), the different chains in the asymmetric units have r.m.s.d. values for C$^\alpha$ atoms in the range 0.3–0.6 Å as calculated by the protein structure-similarity service *PDBeFold* at the European Bioinformatics Institute (Krissinel & Henrick, 2004).

3.4. The increased flexibility necessary for cephalosporin hydrolysis makes OXA-163 less stable

OXA-163 differs from OXA-48 by an S212D substitution and a four-amino-acid deletion corresponding to Arg214, Ile215, Glu216 and Pro217 in OXA-48. Crystal structures of OXA-163 have previously been reported (PDB entries 4s2l, 4s2m and 5har; Stojanoski *et al.*, 2015, 2016); however, we report a new space group and unit cell for our tOXA-163 structure, similar to a crystal form reported for a laboratory mutant of OXA-48 (PDB entry 5hap; Stojanoski *et al.*, 2016) crystallized from similar conditions. Comparing our tOXA-163 structure with another OXA-163 structure (PDB entry 4s2l) reveals perturbations that are localized primarily to polar surface residues, and there are two molecules in the asymmetric unit (Fig. 3). The r.m.s.d. for C$^\alpha$ atoms in one tOXA-163 chain compared with existing OXA-163 structures are: 0.32–0.43 Å for PDB entry 4s2l, 0.52–0.67 Å for PDB entry 4s2m and 0.32–0.46 Å for PDB entry 5har.

For tOXA-163, shortening the loop (Fig. 4) connecting β7 to β8 opens up access to the active site, allowing the binding of bulkier groups, as found in, for example, cephalosporins (Stojanoski *et al.*, 2015). From the enzymatic characterization (Table 4) it was clear that this structural change increases the catalytic turnover for the cephalosporin ceftazidime dramatically, but the carbapenemase enzyme activity is nearly abolished. The DSC results shows that tOXA-163 had a 5.9°C lower melting temperature compared with tOXA-48 (Table 5) and the structure shows that the deletion of residues 214–217 in tOXA-163 disrupts two ionic bonds, Arg214–Asp159

(a)   (b)   (c)
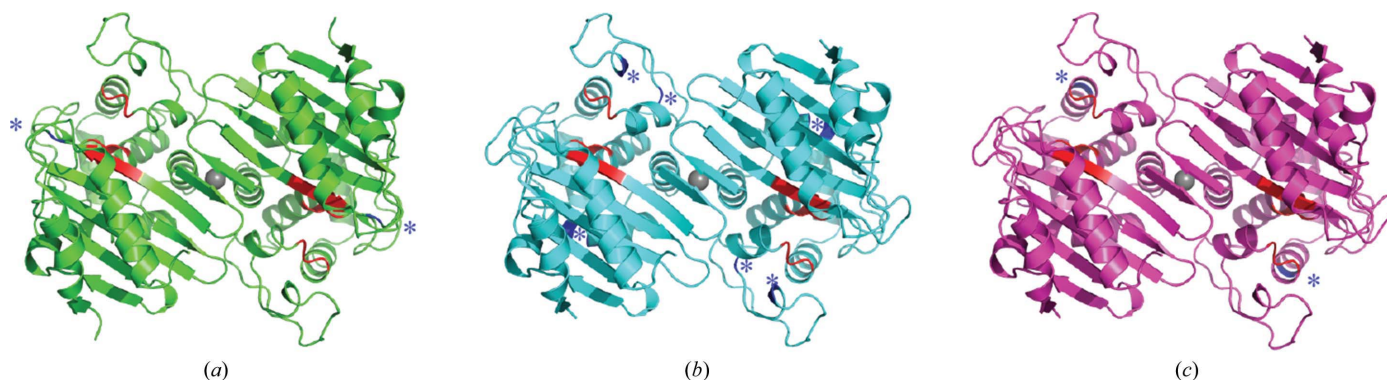
Figure 3
The quaternary structures of tOXA-163 (*a*), tOXA-181 (*b*) and tOXA-245 (*c*) reveal biological dimers with buried chloride ions in the dimer interface (grey). For OXA-245 there are two dimers in the asymmetric unit (one is shown). Active-site motifs are coloured in red and residues involved in substitutions are shown in blue and marked with asterisks.

(2.9 Å) and Glu216–Lys218 (2.4 Å), that are found in both tOXA-181 and tOXA-245 (Figs. 4a, 4b and 4c). The effect of the S212D mutation in OXA-163 seems to partially compensate for the loss of two ionic bonds by forming two hydrogen bonds from the Asp212 side chain to the main-chain N atoms of residue 218 and 219 rather than one as found in tOXA-181 and tOXA-245 (Figs. 4a, 4b and 4c). For OXA-163 it appears that the destabilization of the structure allows greater flexibility and easier access to the active site, facilitating the hydrolysis of bulky substrates (Simakov et al., 2017).

3.5. OXA-181 reveals decreased thermostability

The OXA-181 enzyme differs from OXA-48 by four substitutions: T104A, N110D, E168Q and S171A. Our new structure was resolved to 2.05 Å resolution in space group $P6_2$, with two molecules in the asymmetric unit (Fig. 3). The

tOXA-181 structure has very similar unit-cell parameters to some of the crystals of the homologues OXA-48 (PDB entry 4s2k; King et al., 2015) and OXA-232 (PDB entry 5hfo; P. Retailleau, S. Oueslati, C. Cisse, P. Nordmann, T. Naas & B. Iorga, unpublished work), but the tOXA-181 crystals grew from different crystallization conditions.

The nOXA-181 enzyme has the highest activity against ampicillin of the tested OXAs and has some activity against ceftazidime (Table 4). The activity of nOXA-181 against the carbapenems is lower than that of nOXA-48; however, these in vitro results are not reflected in bacterial cells, where OXA-48 and OXA-181 have very similar hydrolytic profiles (Potron, Nordmann et al., 2011).

For tOXA-181 the thermal stability was reduced by 2.7°C compared with tOXA-48 (Table 5) and this could be attributed to changes in the tertiary structure. The N110D mutation in tOXA-181 introduces an ionic bond from Asp110 to His90,
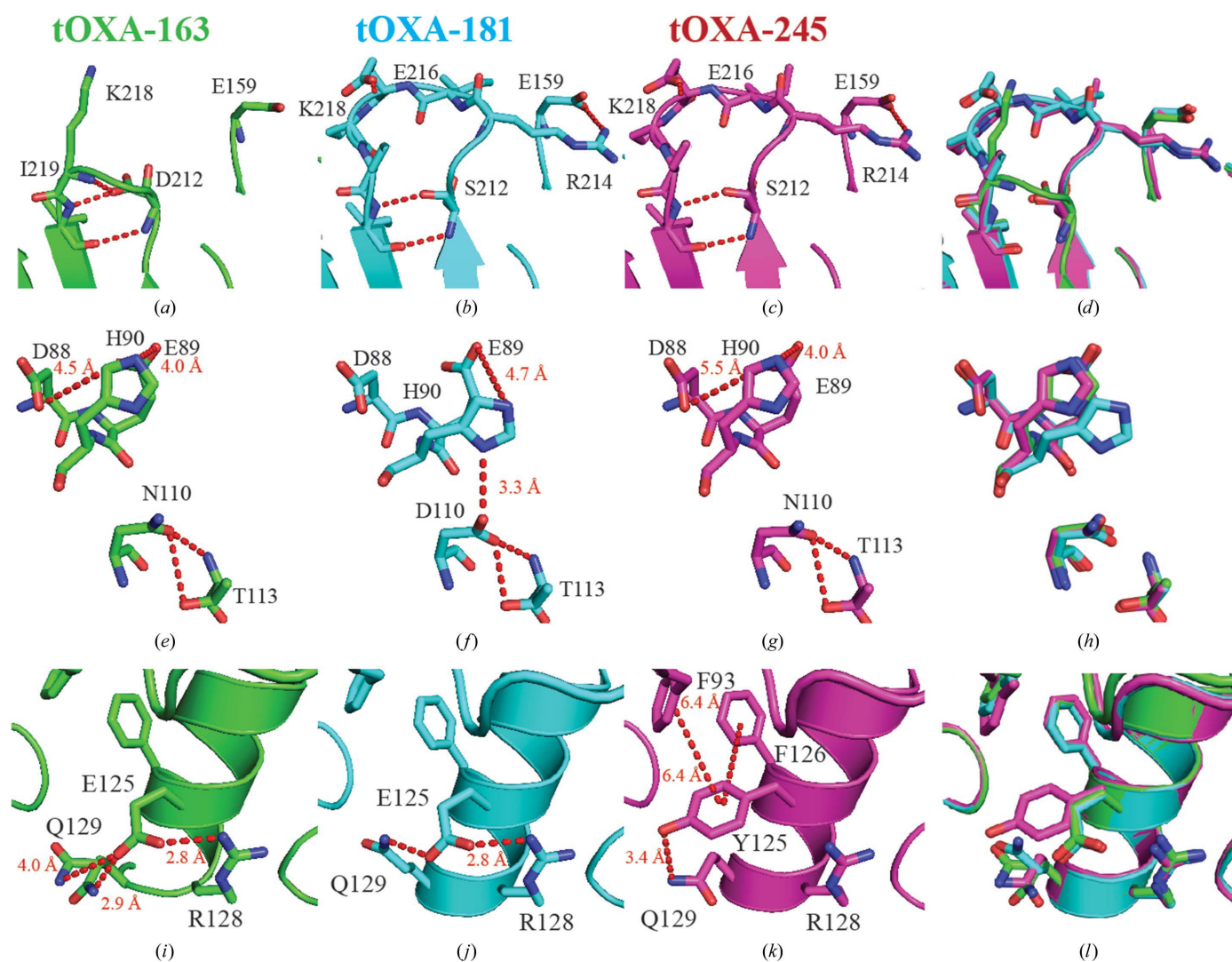

Figure 4
The substitutions in tOXA-163 (green), tOXA-181 (cyan) and tOXA-245 (magenta). (a), (b) and (c) show the S212D substitution and the deletion of residues 214–217 in tOXA-163 which disrupt two ionic bonds. (e), (f) and (g) show the N110D substitution in OXA-181; the aspartic acid forms an ionic bond to His90, which disrupts the Asp88-His90-Glu89 network. (i), (j) and (k) show the E125Y substitution in tOXA-245, where the loss of an ionic bond to Arg128 is compensated by π–π stacking from Tyr125 to both Phe93 and Phe126. (d), (h) and (l) show superpositions of tOXA-163 (green), tOXA-181 (cyan) and tOXA-245 (magenta) for comparison of the three structures.

causing the His90 residue to shift significantly. This disrupts the ionic network Asp88-His90-Glu89 as found in OXA-48 (not shown), tOXA-163 and tOXA-245 (Figs. 4d, 4e and 4f). The other OXA-181 mutations T104A and S171A decrease the overall polarity of the surface, which is likely to make the protein less stable (Vogt et al., 1997; Michetti et al., 2017), thus explaining the lower thermal stability of tOXA-181 compared with tOXA-48.

3.6. A new crystal structure of tOXA-245 uncovers a stabilizing aromatic network

OXA-245 differs from OXA-48 by the single substitution E125Y. The tOXA-245 crystal structure belonged to space group $P2_1$ with four molecules in the asymmetric unit and was refined to 2.20 Å resolution. tOXA-245 crystallized with similar unit-cell parameters to another crystal form of OXA-48 (PDB entry 3hbr).

In our substrate-hydrolysis experiments, nOXA-245 shows the same behaviour as nOXA-181, with higher activity against ampicillin compared with nOXA-48, some activity against ceftazidime and weaker carbapenemase activity than nOXA-48, except for the carbapenem ertapenem, towards which nOXA-245 had the highest activity of the tested OXAs (Table 4). This behaviour is consistent with the antibiotic-susceptibility profile reported previously (Oteo et al., 2013).

tOXA-245 had an increased overall stability of 0.5°C compared with tOXA-48 (Table 5) and only has the E125Y substitution. This stabilization is surprising, since Glu125 in the other structures forms an ionic bond to Arg129 and a hydrogen bond to Gln129. However, in the tOXA-245 crystal structure Tyr125 makes a hydrogen bond to Gln129 with the phenolic hydroxyl group and π–π stacking interactions with Phe126 (6.0 Å between the ring centroids) and Phe93 (6.5 Å between the ring centroids). The π–π stacking from Phe93 to Phe126 and the hydrogen bond from the Gln129 amide N atom to the Tyr125 hydroxyl group may compensate for the loss of the ionic bond (Figs. 4g, 4h and 4i), and thus stabilize the protein and explain the observed 0.5°C increase in overall stability. π–π stacking has been reported in the literature to enhance the overall thermostability (Karlström et al., 2006).

4. Conclusion

Overall, it appears that the changes in the nOXA-181 and nOXA-245 protein sequences are well tolerated, giving a similar hydrolytic spectrum compared with nOXA-48. In overall thermal stability, tOXA-163 was the least stable OXA-48-like enzyme, with a melting temperature reduced by 5.9°C compared with tOXA-48. Based on the crystal structures, we hypothesize that this decrease is caused by two broken salt bridges (Glu126–Arg128 and Glu159–Arg214) and a more accessible active site compared with the three other OXA enzymes. The tOXA-181 enzyme has a 2.7°C lower melting point compared with tOXA-48, possibly owing to one broken ionic interaction in the Asp88-His90-Glu89 network caused by the shift of His90 towards Asp110, combined with an overall decrease in surface polarity. Finally, tOXA-245 was most similar to tOXA-48, with an increased T_m of 0.5°C, and this increase could arise from one additional hydrogen bond (Tyr125–Asn129) and the π–π aromatic stacking network with Phe93-Tyr125-Phe126 compensating for the loss of the Glu125–Arg128 salt bridge.

From these observations, we speculate that a bacterium carrying a serine β-lactamase already has an advantage in β-lactam resistance, that the differences in the sequences of OXA-181 and OXA-245 depend on the original host organism, and that these differences are tolerated as long as there is no interference with substrate hydrolysis.

References

Abdelaziz, M. O., Bonura, C., Aleo, A., El-Domany, R. A., Fasciana, T. & Mammina, C. (2012). J. Clin. Microbiol. **50**, 2489–2491.

Afonine, P. V., Grosse-Kunstleve, R. W., Echols, N., Headd, J. J., Moriarty, N. W., Mustyakimov, M., Terwilliger, T. C., Urzhumtsev, A., Zwart, P. H. & Adams, P. D. (2012). Acta Cryst. D**68**, 352–367.

Antunes, N. T., Lamoureaux, T. L., Toth, M., Stewart, N. K., Frase, H. & Vakulenko, S. B. (2014). Antimicrob. Agents Chemother. **58**, 2119–2125.

Bush, K. (2013a). Ann. N. Y. Acad. Sci. **1277**, 84–90.

Bush, K. (2013b). J. Infect. Chemother. **19**, 549–559.

Bush, K. & Bradford, P. A. (2016). Cold Spring Harb. Perspect. Med. **6**, a025247.

Bush, K. & Macielag, M. J. (2010). Expert Opin. Ther. Pat. **20**, 1277–1293.

Dale, J. W. & Smith, J. T. (1976). Biochem. Biophys. Res. Commun. **68**, 1000–1005.

Danel, F., Paetzel, M., Strynadka, N. C. J. & Page, M. G. P. (2001). Biochemistry, **40**, 9412–9420.

Docquier, J.-D., Calderone, V., De Luca, F., Benvenuti, M., Giuliani, F., Bellucci, L., Tafi, A., Nordmann, P., Botta, M., Rossolini, G. M. & Mangani, S. (2009). Chem. Biol. **16**, 540–547.

Docquier, J.-D. & Mangani, S. (2016). Curr. Drug Targets, **17**, 1061–1071.

Emsley, P., Lohkamp, B., Scott, W. G. & Cowtan, K. (2010). Acta Cryst. D**66**, 486–501.

Evans, B. A. & Amyes, S. G. B. (2014). Clin. Microbiol. Rev. **27**, 241–263.

Evans, P. R. & Murshudov, G. N. (2013). Acta Cryst. D**69**, 1204–1214.

Giuliani, F., Docquier, J.-D., Riccio, M. L., Pagani, L. & Rossolini, G. M. (2005). Antimicrob. Agents Chemother. **49**, 1973–1980.

Guarnera, E. & Berezovsky, I. N. (2016). Curr. Opin. Struct. Biol. **37**, 1–8.

Hall, B. G. & Barlow, M. (2005). *J. Antimicrob. Chemother.* **55**, 1050–1051.

Kabsch, W. (2010). *Acta Cryst.* D**66**, 125–132.

Karlström, M., Steen, I. H., Madern, D., Fedöy, A. E., Birkeland, N. K. & Ladenstein, R. (2006). *FEBS J.* **273**, 2851–2868.

King, D. T., King, A. M., Lal, S. M., Wright, G. D. & Strynadka, N. C. J. (2015). *ACS Infect. Dis.* **1**, 175–184.

Krissinel, E. & Henrick, K. (2004). *Acta Cryst.* D**60**, 2256–2268.

Krissinel, E. & Henrick, K. (2007). *J. Mol. Biol.* **372**, 774–797.

Leiros, H. K. S., Skagseth, S., Edvardsen, K. S. W., Lorentzen, M. S., Bjerga, G. E. K., Leiros, I. & Samuelsen, Ø. (2014). *Antimicrob. Agents Chemother.* **58**, 4826–4836.

Leonard, D. A., Bonomo, R. A. & Powers, R. A. (2013). *Acc. Chem. Res.* **46**, 2407–2415.

Lund, B. A., Christopeit, T., Guttormsen, Y., Bayer, A. & Leiros, H.-K. S. (2016). *J. Med. Chem.* **59**, 5542–5554.

Lund, B. A., Leiros, H.-K. S. & Bjerga, G. E. (2014). *Microb. Cell Fact.* **13**, 38.

McCoy, A. J., Grosse-Kunstleve, R. W., Adams, P. D., Winn, M. D., Storoni, L. C. & Read, R. J. (2007). *J. Appl. Cryst.* **40**, 658–674.

McGann, P., Snesrud, E., Ong, A. C., Appalla, L., Koren, M., Kwak, Y. I., Waterman, P. E. & Lesho, E. P. (2015). *Antimicrob. Agents Chemother.* **59**, 3556–3562.

Meunier, D., Doumith, M., Findlay, J., Mustafa, N., Mallard, K., Anson, J., Panagea, S., Pike, R., Wright, L., Woodford, N. & Hopkins, K. L. (2016). *J. Antimicrob. Chemother.* **71**, 2056–2057.

Michetti, D., Brandsdal, B. O., Bon, D., Isaksen, G. V., Tiberti, M. & Papaleo, E. (2017). *PLoS One*, **12**, e0169586.

Mueller, U., Förster, R., Hellmig, M., Huschmann, F. U., Kastner, A., Malecki, P., Pühringer, S., Röwer, M., Sparta, K., Steffien, M., Ühlein, M., Wilk, P. & Weiss, M. S. (2015). *Eur. Phys. J. Plus*, **130**, 141.

Navon-Venezia, S., Kondratyeva, K. & Carattoli, A. (2017). *FEMS Microbiol. Rev.* **41**, 252–275.

Neet, K. E. & Timm, D. E. (1994). *Protein Sci.* **3**, 2167–2174.

O'Neill, J. (2016). *Tackling Drug-Resistant Infections Globally: Final Report and Recommendations.* London: Review on Antimicrobial Resistance. https://amr-review.org/sites/default/files/160525_Final paper_with cover.pdf.

Oteo, J. *et al.* (2013). *J. Antimicrob. Chemother.* **68**, 317–321.

Paczosa, M. K. & Mecsas, J. (2016). *Microbiol. Mol. Biol. Rev.* **80**, 629–661.

Paetzel, M., Danel, F., de Castro, L., Mosimann, S. C., Page, M. G. P. & Strynadka, N. C. J. (2000). *Nature Struct. Biol.* **7**, 918–925.

Pérez-Vázquez, M., Oteo, J., García-Cobos, S., Aracil, B., Harris, S. R., Ortega, A., Fontanals, D., Hernández, J. M., Solís, S., Campos, J., Dougan, G. & Kingsley, R. A. (2016). *J. Antimicrob. Chemother.* **71**, 887–896.

Podschun, R. & Ullmann, U. (1998). *Clin. Microbiol. Rev.* **11**, 589–603.

Poirel, L., Castanheira, M., Carrër, A., Rodriguez, C. P., Jones, R. N., Smayevsky, J. & Nordmann, P. (2011). *Antimicrob. Agents Chemother.* **55**, 2546–2551.

Poirel, L., Héritier, C., Tolün, V. & Nordmann, P. (2004). *Antimicrob. Agents Chemother.* **48**, 15–22.

Poirel, L., Potron, A. & Nordmann, P. (2012). *J. Antimicrob. Chemother.* **67**, 1597–1606.

Potron, A., Nordmann, P., Lafeuille, E., Al Maskari, Z., Al Rashdi, F. & Poirel, L. (2011). *Antimicrob. Agents Chemother.* **55**, 4896–4899.

Potron, A., Poirel, L. & Nordmann, P. (2011). *Antimicrob. Agents Chemother.* **55**, 4405–4407.

Robert, X. & Gouet, P. (2014). *Nucleic Acids Res.* **42**, W320–W324.

Rojas, L. J., Hujer, A. M., Rudin, S. D., Wright, M. S., Domitrovic, T. N., Marshall, S. H., Hujer, K. M., Richter, S. S., Cober, E., Perez, F., Adams, M. D., van Duin, D. & Bonomo, R. A. (2017). *Antimicrob. Agents Chemother.* **61**, e00454-17.

Samuelsen, Ø., Naseer, U., Karah, N., Lindemann, P. C., Kanestrom, A., Leegaard, T. M. & Sundsfjord, A. (2013). *J. Antimicrob. Chemother.* **68**, 1682–1685.

Schneider, K. D., Bethel, C. R., Distler, A. M., Hujer, A. M., Bonomo, R. A. & Leonard, D. A. (2009). *Biochemistry*, **48**, 6136–6145.

Simakov, N., Leonard, D. A., Smith, J. C., Wymore, T. & Szarecka, A. (2017). *J. Phys. Chem. B*, **121**, 3285–3296.

Stoesser, N., Sheppard, A. E., Peirano, G., Sebra, R., Lynch, T., Anson, L., Kasarskis, A., Motyl, M. R., Crook, D. W. & Pitout, J. D. (2016). *Antimicrob. Agents Chemother.* **60**, 6948–6951.

Stojanoski, V., Adamski, C. J., Hu, L., Mehta, S. C., Sankaran, B., Zwart, P., Prasad, B. V. V. & Palzkill, T. (2016). *Biochemistry*, **55**, 2479–2490.

Stojanoski, V., Chow, D.-C., Fryszczyn, B., Hu, L. Y., Nordmann, P., Poirel, L., Sankaran, B., Prasad, B. V. V. & Palzkill, T. (2015). *Biochemistry*, **54**, 3370–3380.

Tina, K. G., Bhadra, R. & Srinivasan, N. (2007). *Nucleic Acids Res.* **35**, W473–W476.

Vallejo, J. A., Martínez-Guitián, M., Vázquez-Ucha, J. C., González-Bello, C., Poza, M., Buynak, J. D., Bethel, C. R., Bonomo, R. A., Bou, G. & Beceiro, A. (2016). *J. Antimicrob. Chemother.* **71**, 2171–2180.

Vogt, G., Woell, S. & Argos, P. (1997). *J. Mol. Biol.* **269**, 631–643.

Supporting information

Table S1   Macromolecule production information for the cloning and production of OXA-163,OXA-181 and OXA-245. Italic nucleotides

Source organism	*Klebsiella pneumoniae*	
DNA source	Genomic DNA	
	Native construct with signal peptide:	**His-tagged construct with TEV-protease cleavage site:**
Forward primer	**OXAs:** ATAATTTTGTTTAACTTTAAGAAGGAGATATACATATGCGTGTATTAGCCTTATC GG	**TEV-cleavage site[a]:** ACCATCACCTCGAATCAACAAGTTTGTAC*GGTGAGAATCTTTATTTTC GGGT*T **OXAs:** GTTTGTACGGTGAGAATCTTTATTTTCAGGGTAAGGAATGGCAAGAAAACAAAAGT
Reverse primer	**OXAs:** GGCTTTGTTAGCAGCCTCGAATCACTAGGGAATAATTTTTTCCTGTTTGAG	**TEV-cleavage site[a]:** GGCTTTGTTAGCAGCCTCGAATCA*ACCCTGAAAATAAAGATTCTCACCG* **OXAs:** GGCTTTGTTAGCAGCCTCGAATCACTAGGGAATAATTTTTTCCTGTTTGAG
EMP R2 primer	TTCTAGAGGGAAACCGTTGTGGTCT	TTGTTGATTCGAGGTGATGGTGAT
Cloning vector	pDEST17	
Expression vector	pDEST17	
Expression host	*E. coli* BL21 (DE3) STAR pRARE	
Complete amino acid sequence of the construct produced[a]		
OXA-163[b]		**(tOXA-163)** HHHHHHENLYFQGKEWQENKSWNAHFTEHKSQGVVVLWNENKQQGFTNNLKRANQAFLPASTFKIPNSLIALDLGVVKDEHQVFKWDGQTRDIATWNRDHNLITAMKYSVVPVYQEFARQIGEARMSKMLHAFDYGNEDISGNVDSFWLDGGIRISATEQIS

FLRKLYHNKLHVSERSQRIVKQAMLTE
ANGDYIIRAKTGYDTKIGWWVGWVEL
DDNVWFFAMNMDMPTSDGLGLRQAIT
KEVLKQEKIIP

(nOXA-181)

OXA-181

<u>MRVLALSAVFLVASIIGMPAVA</u>
KEWQENKSWNAHFTEHKSQG
VVVLWNENKQQGFTNNLKRA
NQAFLPASTFKIPNSLIALDLGV
VKDEHQVFKWDGQTRDIAAW
NRDHDLITAMKYSVVPVYQEF
ARQIGEARMSKMLHAFDYGNE
DISGNVDSFWLDGGIRISATQQI
AFLRKLYHNKLHVSERSQRIVK
QAMLTEANGDYIIRAKTGYSTR
IEPKIGWWVGWVELDDNVWFF
AMNMDMPTSDGLGLRQAITKE
VLKQEKIIP

(tOXA-181)

<u>MSYYHHHHHHLESTSLYGENLYFQ</u>
GKEWQENKSWNAHFTEHKSQGVV
VLWNENKQQGFTNNLKRANQAFLP
ASTFKIPNSLIALDLGVVKDEHQVF
KWDGQTRDIAAWNRDHDLITAMK
YSVVPVYQEFARQIGEARMSKMLH
AFDYGNEDISGNVDSFWLDGGIRIS
ATQQIAFLRKLYHNKLHVSERSQRI
VKQAMLTEANGDYIIRAKTGYSTRI
EPKIGWWVGWVELDDNVWFFAMN
MDMPTSDGLGLRQAITKEVLKQEKI
IP

(nOXA-245)

OXA-245

<u>MRVLALSAVFLVASIIGMPAVA</u>
KEWQENKSWNAHFTEHKSQG
VVVLWNENKQQGFTNNLKRA
NQAFLPASTFKIPNSLIALDLGV
VKDEHQVFKWDGQTRDIATW
NRDHNLITAMKYSVVPVYQYF
ARQIGEARMSKMLHAFDYGNE
DISGNVDSFWLDGGIRISATEQI
SFLRKLYHNKLHVSERSQRIVK
QAMLTEANGDYIIRAKTGYSTR
IEPKIGWWVGWVELDDNVWFF
AMNMDMPTSDGLGLRQAITKE
VLKQEKIIP

(tOXA-245)

<u>MSYYHHHHHHLESTSLYGENLYFQ</u>
GKEWQENKSWNAHFTEHKSQGVV
VLWNENKQQGFTNNLKRANQAFLP
ASTFKIPNSLIALDLGVVKDEHQVF
KWDGQTRDIATWNRDHNLITAMK
YSVVPVYQYFARQIGEARMSKMLH
AFDYGNEDISGNVDSFWLDGGIRIS
ATEQISFLRKLYHNKLHVSERSQRIV
KQAMLTEANGDYIIRAKTGYSTRIE
PKIGWWVGWVELDDNVWFFAMN
MDMPTSDGLGLRQAITKEVLKQEKI
IP

---

[a] The nucleotides in the TEV protease cleavage site sequence is in italics. Underlined residues in the amino acid sequence are cleaved off by signal peptide peptidases in transport to the periplasm for the native construct or by an in-house TEV-protease during purification for the His-tagged construct.

[b] The gene for OXA-163 was synthesized with optimized codon usage and subcloned into the expression vector.
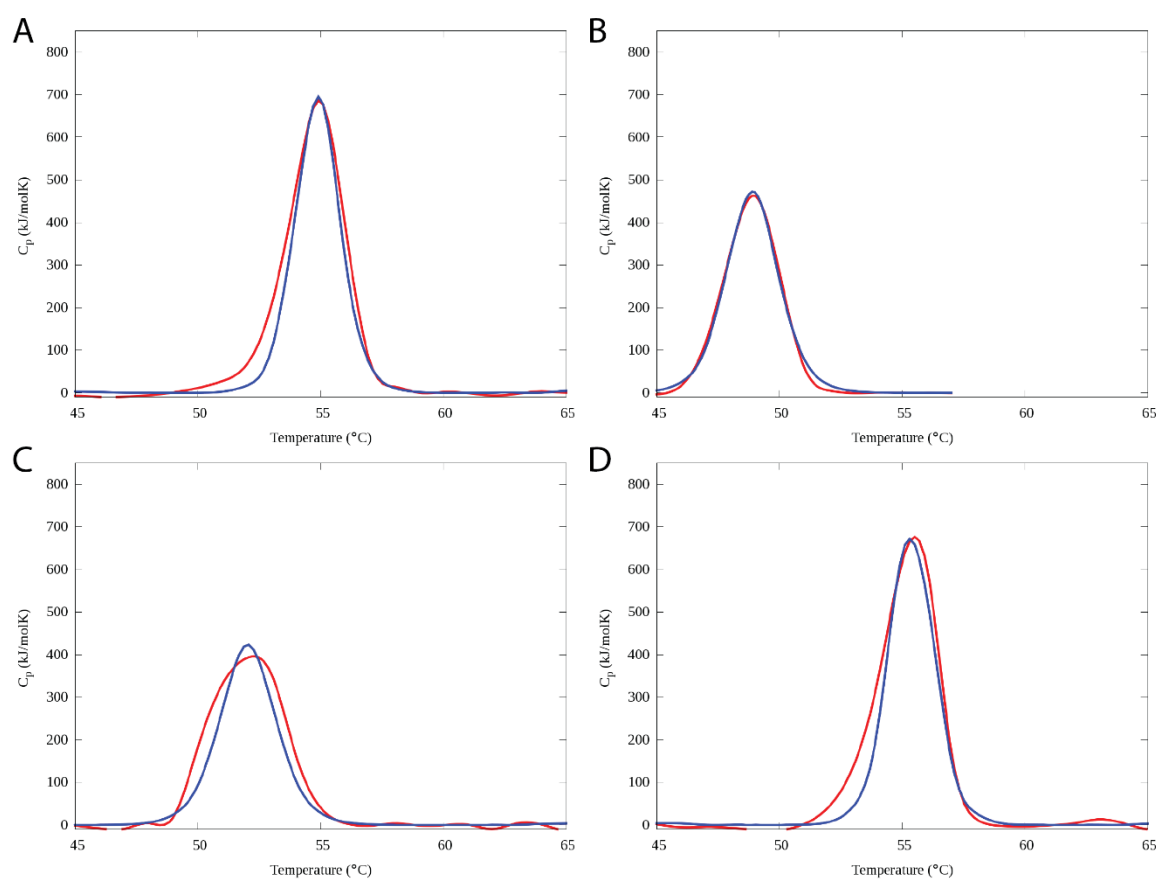
Figure S1 Differential scanning calorimetry curves (red) for (A) OXA-48, (B) OXA-163, (C) OXA-181 and (D) OXA-245 with the theoretical two-state model fitted (blue) for the respective dimers to calculate the ΔH of unfolding.